CHALMERS
UNIVERSITY OF TECHNOLOGY

Optimal Design of PMSM for High – Performance Sensorless Applications

Master of Science Thesis

MOHAMED SAAD

Department of Energy and Environment
Division of Electric Power Engineering
CHALMERS UNIVERSITY OF TECHNOLOGY
Gothenburg, Sweden 2015

BOSCH

Optimal Design of PMSM for High – Performance Sensorless Applications

MOHAMED SAAD

CHALMERS
UNIVERSITY OF TECHNOLOGY

Department of Energy and Environment
Division of Electric Power Engineering
Chalmers University of Technology
Gothenburg, Sweden 2015

Optimal Design of PMSM for High – Performance Sensorless Applications
Master of Science Thesis
MOHAMED SAAD

Supervisor: Dr. Alin Stirban, Robert Bosch GmbH
Supervisor: Dr. Ioan Serban, Robert Bosch GmbH
Examiner: Dr. Stefan Lundberg, Energy and Environment

Master's Thesis 2015
Department of Energy and Environment
Division of Electric Power Engineering
Chalmers University of Technology
SE-412 96 Gothenburg
Telephone +46 31 772 1000

Cover: Bosch's Engine Compartment Actuator (ECA - E) which has the PMSM as one if its components [1].

Optimal Design of PMSM for High – Performance Sensorless Applications
Master of Science Thesis
MOHAMED SAAD
Department of Energy and Environment
Division of Electric Power Engineering
Chalmers University of Technology

Abstract

Permanent magnet synchronous motors (PMSMs) are very attractive for industrial applications due to their high efficiency, robustness, and reliable design. However, vector control of permanent magnet AC drives requires rotor position information. With a sensorless vector control, the system is able to detect the position without any need for a position sensor. This is very beneficial as it reduces the hardware complexity, and cost, and increases the system reliability.

The master's thesis study is performed in the department (CR/ARE3): Electrical drives (ED) and Power Electronics (PE) in Robert Bosch GmbH, Stuttgart, Germany. The main goal is to investigate the sensorless vector control performance of the PMSM drive system in the early stages of the machine design. This is done by the simulation of the machine and the position estimation process and comparing any modification with the original system. The study's results may have a great impact on many of Bosch's products like: the engine compartment actuator (ECA - E), the eBike System, and others where the PMSM drive system is implemented.

In Chapter 3, the PMSM of Bosch's engine compartment actuator (ECA - E) is studied, simulated, and tested using a Finite Element Analysis (FEA) software. In Chapter 4, the incremental inductances of the machine are introduced and a methodology to measure the level of harmonic disturbance in them is implemented. This level of harmonic disturbance is selected as the key performance indicator to give a preliminary evaluation of the capability of the PMSM to perform sensorless control in a good quality using saliency tracking which is verified in a later stage. In Chapter 5, the integration between the simulated machine and Bosch's position estimator is performed. That position estimator is based on saliency tracking using high frequency voltage signal injection in the estimated rotor reference frame. In Chapter 6, five different machine geometrical modifications are simulated and integrated with the position estimator and the level of harmonic disturbance in the incremental inductances is measured for each case. The obtained results are presented and compared to verify the relation between the selected key performance indicator and the sensorless performance of the different machines. Additionally, the materials costs as well as the rated torque for every modification are calculated and presented.

It is found that adding air holes in the rotor core has no effect on the har-

monic content of the incremental inductances or the sensorless performance. The electrical position estimation error is kept between 2.5 and −18.75 degrees similar to the original machine. However, this modification can offer the same rated torque with a decrease (0.78 %) in materials costs.

Adding more steel between magnets has a good effect. It makes the harmonic content (KPI) of the inductances mostly lower. Also, a better sensorless performance is obtained where the electrical position estimation error is kept between 0.5 and −18.75 degrees. However, there is a decrease (15.6 %) in the rated toque and an increase (0.22 %) in the materials costs.

Closing the openings of the stator slots has a bad effect. It makes the harmonic content (KPI) of the inductances mostly higher in a big way. Also, a worse sensorless performance is obtained where the position estimator fails to work. Additionally, there is a decrease (37.7 %) in the rated toque and an increase (0.13 %) in the materials costs.

Increasing the width of the stator teeth has a bad effect regardless of the KPI. In spite of making the harmonic content (KPI) mostly lower, a worse sensorless performance is obtained where the position estimator fails to work. The difference between the inductances L_{qq} and L_{dd} decreases by 80 %, 55 %, and 50 % for the loads 0 %, 30 %, and 100 % respectively which explains the failure. Additionally, there is an increase (10 %) in the rated toque and an increase (1.57 %) in the materials costs.

Finally, increasing the width of the stator yoke has a good effect. It makes the harmonic content (KPI) of the inductances mostly lower. Also, a better sensorless performance is mostly obtained where the electrical position estimation error is kept between 1 and −18.75 degrees. Additionally, there is an increase (4.64 %) in the rated toque and an increase (2.62 %) in the materials costs.

Keywords: PMSM, sensorless control, finite element, incremental inductance, saliency tracking, position estimator, voltage signal injection, machine design.

Acknowledgements

I would like to thank Robert Bosch GmbH for giving me the opportunity to perform my master's thesis in the new research campus in Renningen, Germany and providing me with all the tools and software licenses that were needed.

I would like to express my sincere gratitude to Dr. Alin Stirban and Dr. Ioan Serban for their patience and continuous support of my Master study. Dr. Stirban's support was one of the main reasons that I was able to complete my work.

I would also like to thank Dr. Stefan Lundberg for his support during the course: Electric Drives 2 and valuable input through phone which helped a lot in my thesis work.

I extend my sincere thanks to "The Swedish Institute" for the financial support and the study scholarship which gave me the chance to do my master's degree in Sweden.

Finally, I sincerely thank my family and particularly my mother for her never ending love and support throughout the years.

Mohamed Saad, Stuttgart, Germany, July 2015

Contents

List of Figures

List of Tables

1

Introduction

1.1 Background

Global warming is a very serious problem that is facing humanity nowadays. It has many bad environmental impacts. Some of these impacts are: rising sea level, change of precipitation and local climate conditions; acid rain, alteration of forests and crop yields, expansions of deserts into existing rangelands, more intense rainstorms, and destabilization of ocean currents [2]. According to [3], transportation is the source of approximately one-quarter of energy-related greenhouse gas emissions globally. Therefore, vehicle and automobile manufacturers have a great responsibility to solve this problem. Improved vehicle fuel efficiency is the key to mitigation of that climate change as the greenhouse gases are the main reason for global warming [3].

The reduction of fuel emissions can be achieved by using electric propulsion. Hybrid and pure electric drives are good examples of that. They can replace the commonly used internal combustion engine. The most important components of these drives are the electric motors.

Electric motors are devices that create motion. There are many kinds of electric motors depending on their construction. Some of these motors are the permanent magnet synchronous motors (PMSMs). As the name suggests, the source of the flux in these motors is the magnetic material [4]. Permanent magnets are mounted on the rotor which then removes the need for injection of current to a moving component as in the case of the electrically magnetized synchronous motor or the induction machine [4]. The most obvious advantages of using PMSMs are high efficiency and power factor compared to an induction machine of the same size, robust and reliable design, and no conduction losses in the rotor [5]. That is why PMSMs are commonly used for propulsion as well as different motion applications. According to [6], the permanent magnet synchronous motor (PMSM) is the main component of Bosch's engine compartment actuator (ECA - E) shown in Figure 1.1. This engine compartment actuator (ECA - E) has various application areas in au-

tomotive systems like: Electrical variable valve timing (VVT) actuators, Electrical hybrid-decoupler, Electronic clutch system, and many others [1]. Any improvement in the ECA-E performance will have a good impact on its applications. A better electrical variable valve timing (VVT) actuator will reduce fuel emissions.

One drawback with actuators based on PMSMs, i.e. Permanent Magnet AC drives, is that they need information about the rotor position to perform the vector control of the PMSM stator currents [7]. Sensorless vector control is the ability of the drive system to detect the rotor position and perform the vector control without any need for a position sensor [7]. It is a desirable kind of control because the sensors may result in many practical problems such as hardware complexity, high cost, reduced reliability due to cables and sensor itself, difficulties of mechanical attachment of sensor to the electric machine, increased axial length of the machine, and electromagnetic noise interference [8]. However, the sensorless control has some problems and obstacles. The quality of its performance is affected by many factors like: loading, magnetic saturation, rotor position, and speed of rotation. These factors are strongly connected to the geometry of machine and its design, i.e. the control's performance heavily depends on the machine's physical geometry [9].

Figure 1.1:
Bosch's Engine Compartment Actuator (ECA - E) which has the PMSM as one if its components [1].

The department (CR/ARE3): Electrical drives (ED) and Power Electronics (PE) in Bosch has launched the master's thesis study "Optimal Design of PMSM for High – Performance Sensorless Applications" to investigate the possibility of a better sensorless vector control performance of the PMSM drive system. The study's results may have a great impact on many of Bosch's products like: the engine compartment actuator (previously mentioned), the eBike System, and others where the PMSM drive system is implemented.

As the world's largest independent automotive supplier [10], Bosch has a responsibility towards both vehicle and automobile manufacturers and environment. A better performance of Bosch's engine compartment actuator (ECA - E) in the "Electrical variable valve timing (VVT) actuators" will have a great impact on fuel economy and emissions. This can help solve or decrease the problem of global warming previously mentioned.

1.2 Aim

The aim of this project is the verification of a key performance indicator (KPI) that evaluates the quality of the potential sensorless vector control capabilities of a certain permanent magnet synchronous machine under study using saliency tracking.

1.3 Task

As mentioned earlier, the main goal of the study is the verification of a key performance indicator. This key performance indicator is defined as a tool that can give machine designers a preliminary idea of whether a certain permanent magnet synchronous machine design will have a better sensorless control performance compared to a previous design or not. To reach that goal, a number of tasks need to be done. These tasks will be performed in a certain chronological order. This kind of arrangement is an essential factor because every task and its expected results will be needed to perform the next one. The tasks are as follows:

1. Literature study
2. Needed software study
3. Study of the key performance indicator
4. Studying some of Bosch's PMSMs used in real life products

5. Creating a simulated model of the studied PMSMs
6. Studying and integration of the proposed sensorless observer
7. Full system simulation including the observer
8. Validation of the key performance indicator

As mentioned before, every task is needed to perform the next one. The most important task for the project is the literature study. This study includes not only the basic theory but also real life applications and research done in the field. This will help lay the ground and give an idea of what results that can be expected from this thesis study. The next task is identifying the software tools that will be used for building models, simulation, and all kinds of calculations needed to reach the goal. These software tools must be carefully studied to know their environment, capabilities, and limitations. This study includes performing some simple tasks and analyzing the expected results of them.

Then, the information obtained from the literature study of both basic theory, and updated research done in the field must be analyzed. This analysis will be needed to find out what is the possible KPI and how it can give a preliminary evaluation of the capability of a certain PMSM to perform sensorless vector control in a good quality. The next task is to study the dimensions, design, specifications, and load profiles of some PMSMs which are used in some products. The machines should be investigated so that it would be possible to create an acceptable simulated model of them in the next task.

Using the knowledge built up by studying of both software tools and real life PMSMs, a complete simulation model of the machine under study should be created. The model should be tested and checked to make sure that it gives an acceptable performance when it is compared with the real life machine. After that, some models of Bosch's real life sensorless observers should be studied. These observers should be based on the technology decided to be used in the project according to the information collected from the literature study. After understanding the operating principles of the observers, all the machine parameters and information needed for the integration of the observers with the PMSMs and having a working system should be identified and collected.

After making sure that the integration of the observer with the PMSM model is successful. Several simulations of the modelled system under operation should be performed. These simulations should take into account different loading profiles and conditions similar to real life applications. Finally, the link between the KPI and its

effect on the sensorless control performance should be validated. Several scenarios for the KPI should be performed and the resulting effects on the simulated model should be recorded and analyzed.

1.4 Scope

As concluded from the previous sections, the project investigates the quality of performance of a PMSM machine under sensorless vector control. All systems including the machine itself and the sensorless observer will be simulated using software tools. Real life testing will not be performed in this stage. The main focus is to find some indicators and parameters that can offer some guidance for selecting a suitable PMSM machine for a certain sensorless control application.

Literature study will be focused on synchronous machines and specifically PMSM. It will include not only the machine basic theory, construction, and performance but also different technologies used for sensorless control and real life applications. The PMSM is selected for this study because of its several advantages mentioned in section 1.1 which are desirable in automotive applications. Testing will not be included as the identification and verification of the key performance indicators is the main focus and the time period is limited.

A simulated model of the machine will be built. This model will be based on some real life products of Bosch. Two products are suggested at this stage: the engine compartment actuator (ECA - E), and the eBike System. The simulated model will take into account the basic construction, material selection, and real life load profiles. Details about machining allowances, fillets, and coil construction will not be included as the models will be more complicated and it will not have a big impact on the sensorless control performance, and the KPIs identification and verification.

Some of Bosch's real life sensorless observers will be studied to be used in the simulated model. Simulations based on different sensorless control techniques are not the project's main focus. The main focus is to have a working model of a sensorless observer based on a real life application that can help evaluate the machine's sensorless control performance.

Literature study will be carried out at the beginning of the project. Materials concerning the basic theory of both synchronous machines and sensorless control techniques need to be investigated. Updated research and studies in the field of sensorless control need to be reviewed and evaluated for any potential value in

the project. As mentioned in section 1.3, some software tools will be used in the project. Machine simulation will be carried out in a Finite Element Analysis (FEA) software. The software selected for that purpose is JMAG [11]. It is a high-speed, high-precision FEA software tool that can be used in the simulation of electrical devices such as motors, transformers, relays, and others.

Based on the reviewed research, possible candidates for the key performance indicators will be identified and studied carefully. As discussed in section 1.4, some real life products of Bosch will be studied and investigated. The studies will be mainly focused on basic construction, material selection, and real life load profiles of the PMSM used in these products. Two products are suggested: the engine compartment actuator (ECA - E), and the eBike System. Data concerning the loading profile, back electromotive force (EMF), bad sensorless-control-performance loading points, machine behavior under no load, and full load operation should be collected. Later, this data will be compared with the simulated model to make sure that they have similar behavior.

After collecting this data, the simulated model of the PMSMs will be created in JMAG-Designer. All the parameters needed for the observer should be collected at this stage. The sensorless observer model will be a Matlab/Simulink model. The successful integration of the observer and the machine models should be checked. This can be done by choosing some operating points and comparing them with the real life PMSM system used in Bosch's products. Again, simulated data concerning the loading profile, back electromotive force (EMF), bad sensorless-control-performance loading points, machine behavior under no load, and full load operation should be collected for comparison as mentioned before.

Finally, the identified key performance indicators should be validated. This can be done by varying the factors affecting these KPIs, running the full system simulation, and studying the resulting sensorless performance of the PMSM system. This process should be repeated many times taking into account the bad sensorless-control-performance loading points identified in the early stages. After verification, further formulation of these KPI's should be performed so that a detailed point-by-point guidance is created. This guidance should include specifications of the machines which can offer better sensorless vector control performance. It will be relevant to machine designers and drive system manufacturers.

2

Motor Theory

2.1 Introduction

An electric motor is an electrical machine that converts electrical energy into mechanical energy. If this motor is driven by an alternating current, it is called an AC motor. AC motors have many uses in daily life. Most of the applications that run on electricity and require some kind of motion are based on this kind of machines. They can be found in many industry applications, including automotive and vehicle industry. According to Figure 2.1, three phase AC motors can be divided into two categories synchronous and asynchronous motors. There are many kinds of synchronous motors such as: reluctance, hysteresis, stepped and permanent magnet (pm) motors [12]. The last motor is the main focus of this study.

2.2 Permanent Magnet Synchronous Motor

DC machines with permanent magnet field excitation were developed in the 1950s. This was due to the availability of permanent magnets which are efficient and have high energy density. Thus, the DC machines became more compact as the electromagnetic poles based on windings were replaced by these magnets. Later in the 1950s, the use of switching power transistor and silicon-controlled rectifier devices made the replacement of the mechanical commutator with an electronic commutator possible. The use of permanent magnets as well as these electronic devices helped in the creation of the permanent magnet synchronous machines (PMSMs) together with the brushless DC machines (BLDCs) [13].

It is very well-known that the induction machines IMs are the most commonly used motors in the industrial drive applications. These days, permanent magnet synchronous machines have taken a good place in the industrial market. Permanent magnet machines have many traits which make them desirable in many industrial

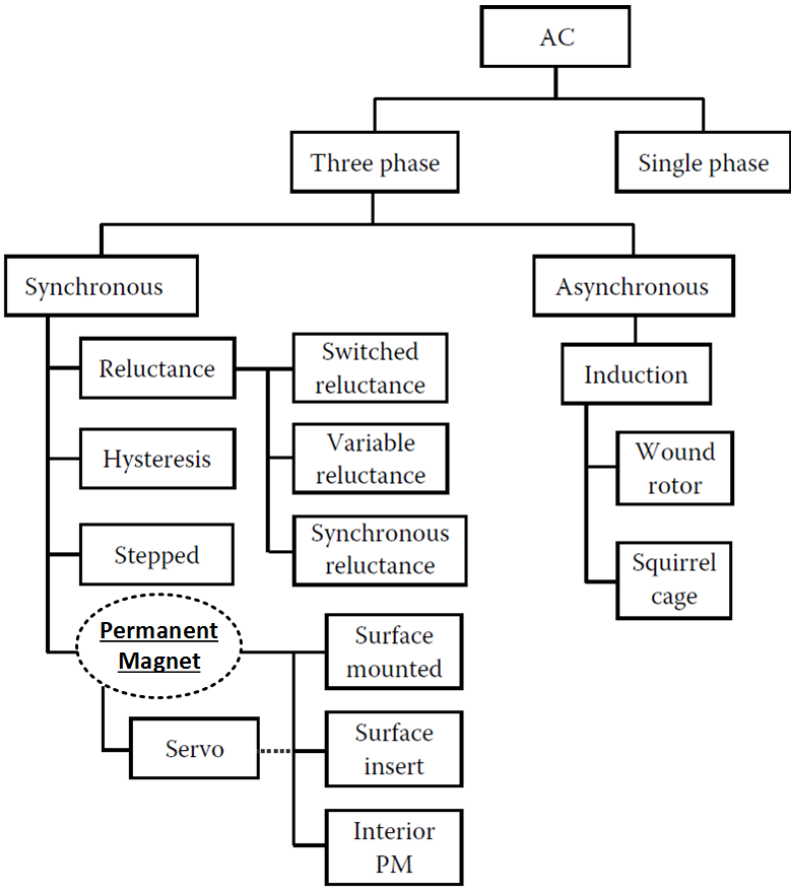

Figure 2.1:
The classification of AC electric motors [12].

applications like: automotive, robotics, and aerospace. They are commonly used in industry in machine tools and position servomotors because of their good dynamic performance and their low maintenance.

The most desirable characteristic of PM synchronous machines is the replacement of the winding excitation with permanent magnets. This plays an important role in increasing the motor efficiency as the excitation losses are removed. Also, the concentration of the conduction losses in the stator makes it easier in terms of heat dissipation. All of this has a great impact on decreasing the rotor diameter and consequently the whole motor size resulting in high power density and low motor inertia. As mentioned earlier, PM motors have a high dynamic performance. This is due to the use of high energy magnets which increases the torque per ampere constant when compared with DC or induction machines [7]. The absence of slip-rings due to the use of the permanent magnets plays an important role when it comes to the machine reliability. The motor becomes more robust and therefore lower maintenance is needed [5].

As discussed, PM machines are very desirable in many industrial applications. It is worth mentioning that, despite the advantages of using them, there are still some disadvantages. The most important disadvantage is that they need closed loop frequency converter control. This means that in order to be able to control a permanent magnet synchronous machine, the position of the rotor must be well-known. This can be done by using a position encoder or by the estimation of rotor position (sensorless control) [14]. The open loop control is usually not possible (i.e. when the motor is grid connected). Additionally, a typical permanent synchronous machine can't start on its own, and some other methods of producing a start-up torque are needed [14]. Some other drawbacks include: permanent magnets have high cost, the field weakening control is obtained by additional effort, and demagnetization occurs at high temperature [15].

2.2.1 Construction

Like any other motor construction, the two main components of the PM synchronous machine are the stator and the rotor. As the name suggests, the stator is the stationary part of the motor while the rotor is the rotating part. The stator construction is similar to that of other AC machines, for examples the induction machine.

The stator core which can be shown in Figure 2.2 is mainly made of laminated sheets (reducing eddy currents) attached together with a certain shape to form a group of teeth and slots. The stator has a poly-phase winding, mainly three-phase. By the inspection of these windings, it is easy to find that it consists of a uniform array of identical coils, located in the slots. These coils form a three phase-winding, distributed around the stator, and the phase windings are symmetrically displaced with respect to one another [14]. The three phase-windings are connected either in star (wye) or delta (mesh). When these windings are connected to a three phase supply, a rotating magnetic field is produced in the air-gap.

As mentioned earlier, the PM synchronous machines have permanent magnets attached to the rotor to provide the field. Thus, only one supply is connected to the stator. PMSMs can be classified into two main categories depending on the direction of the field flux. These two categories are: radial field and axial field machines [13]. The radial field machine shown in Figure 2.2 has the flux direction along the radius of the machine while the axial one has the flux direction parallel to the rotor shaft. The most common ones are the radial field machines. The axial field ones are used in a small number of applications nowadays which require high power density and acceleration [13].

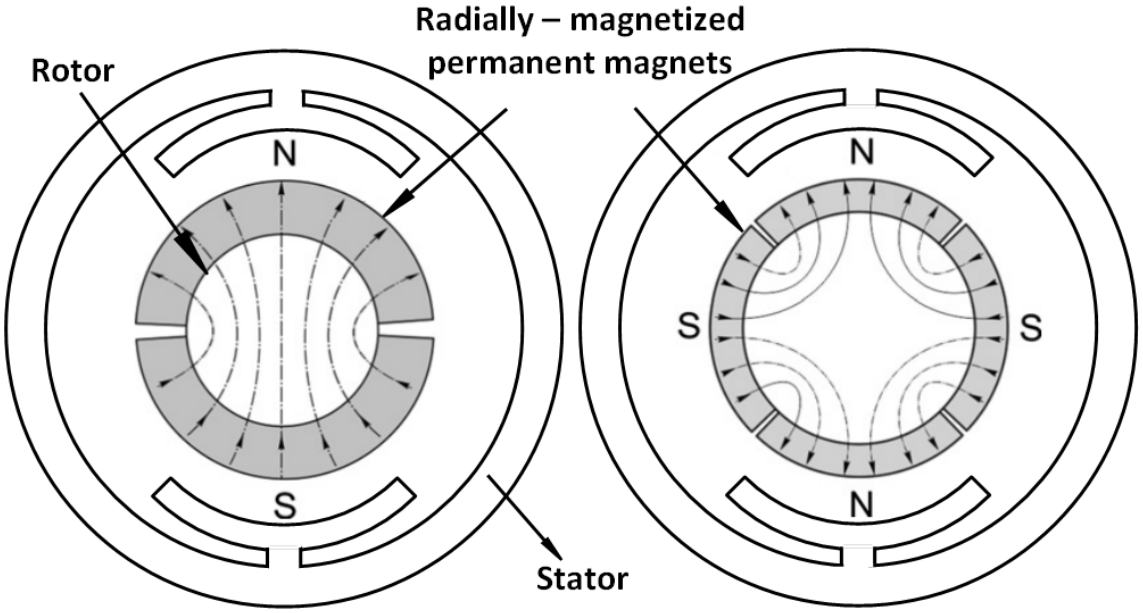

Figure 2.2:
Permanent magnet synchronous motor: 2-pole (left); 4-pole (right) [5].

2.2.2 Types of PMSMs

The permanent magnets of the PM synchronous motors are placed on the rotor. There are many different ways and arrangements by which these permanent magnets are placed. The basic principle of operation of the machine is the same regardless of the way of mounting the permanent magnets on the rotor. Different methods of mounting magnets result in different types of machines. Also, these methods result in the difference between direct and quadrature axes inductance values.

The direct axis shown in Figure 2.3 is the rotor magnetic axis where the flux passes mainly through the magnets. While, the quadrature axis shown in Figure 2.3 is the axis that is perpendicular to the direct axis in electrical degrees. The direct axis inductance is the stator inductance when the direct axis or magnets are aligned with the stator winding. While, the quadrature axis inductance is the inductance measured in the position obtained by rotating the magnets from the aligned position by 90° where the stator flux sees the interpolar area of the rotor containing only the iron path [13]. The permanent magnet synchronous motors are classified into many types which include:

1. *Surface-Mounted PMSM*: As seen in Figure 2.3a, the permanent magnets are placed on the outer surface of the rotor core in this kind of machine. It provides high air gap flux density. This structure has some disadvantages as it has low mechanical robustness and it is not preferred in high speed applications.

Also, the difference between the quadrature and direct axes inductances in this machine is very small [13]. So, it is not practical for sensorless applications based on saliency tracking. The field weakening capabilities of this kind of machine is poor but it is possible [5].

2. *Surface-Inset PMSM*: In this type of machine, the magnets are placed in the grooves of the outer surface of the rotor core resulting in a cylindrical surface which can be seen in Figure 2.3b. In comparison with the Surface-Mounted PMSM, this machine is more mechanically robust. The ratio between the quadrature and direct axes inductances can be as high as 2–2.5 [13].

3. *Interior PMSM*: If the permanent magnets are placed inside the rotor core whether in a radial or circumferential directions as seen in Figure 2.3c and d, the machine is called: Interior PMSM. It is very mechanically robust and therefore preferred for high-speed applications. It has a high ratio between the quadrature and direct axis inductances, respectively. If a wide speed range is required (using field weakening), the interior PMSM can be used [5]. In Figure 2.3c, steel is removed from the rotor structure to create large air gaps between the adjacent magnets. These air gaps are called: "flux barriers". They have two advantages: they prevent the reduction in the mutual flux linkages between the stator and the rotor and they give low rotor inertia as they reduce the weight of the rotor. The structure shown in Figure 2.3d gives a higher air gap flux density compared to the Surface-Mounted PMSM which results in higher efficiency and smaller stator excitation for the same power output. But it has a high rotor volume [13].

4. *Line-Start PMSM*: These are the PM synchronous motors designed for constant speed applications. In addition to the normal construction of a PM synchronous machine, they have squirrel cage windings. These windings have two main uses: they provide torque from standstill and help in damping the rotor oscillations [13]. When synchronism is reached (zero slip), the effect of these windings disappear as there is no induced voltage in them.

2.2.3 Operation and modelling

Like induction motors, a rotating magnetic field is produced when the stator windings of a permanent magnet synchronous motor are connected to a 3-phase supply. The synchronous speed is defined as: "the speed of rotation of the magnetic field".

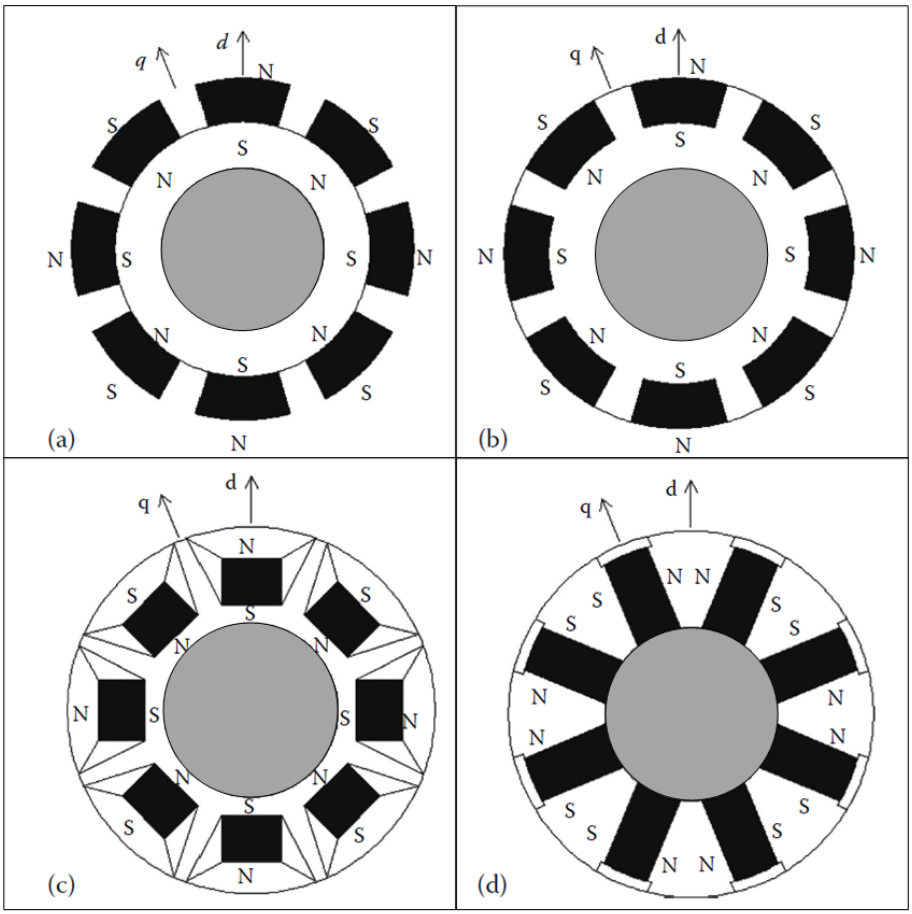

Figure 2.3:
(a) Surface PM (SPM) synchronous machine. (b) Surface inset PM (SIPM) synchronous machine. (c) Interior PM (IPM) synchronous machine. (d) Interior PM synchronous machine with circumferential orientation [13].

This speed is directly proportional to the supply frequency, and inversely proportional to the pole-number of the winding [14]. This can be seen in

$$N_s = \frac{120f}{p} \tag{2.1}$$

where N_s is the synchronous speed , f is the supply frequency and p is the pole-number of the winding. The rotor which has permanent magnets is designed to lock on or synchronize with the rotating magnetic field which is generated by the stator windings. Thus after synchronization, the rotor will run at the same speed as the rotating field independent of the load variation. From this and (2.1), it is clear that the rotor speed will remain constant as long as the supply frequency is constant.

Also, it is very important to keep in mind one of the most well-known relations in electric synchronous machines. It is the relation between the angular stator fre-

quency (frequency of the current in the stator windings) and the angular mechanical speed of the rotor. The angular stator frequency is equal to the angular mechanical speed multiplied by pairs of poles [13]. This can be formulated as

$$\omega_e = \frac{p}{2}\omega_m \tag{2.2}$$

where ω_e is the angular stator frequency, p is the pole-number of the machine and ω_m is the angular mechanical speed. Ideally, the induced electromotive force (e.m.f.) is sinusoidal in the PM synchronous motor [5]. This can be done by the proper shaping of the rotor permanent magnet poles which results in a sinusoidal distribution of the air gap flux.

In order to have a properly functional motor, the torque (or the power) produced by that motor should be constant. As mentioned earlier, the induced e.m.f. generated in the machine is sinusoidal. From that fact and from [5], a constant output power (constant torque) can be produced on one condition. That condition is that the injected 3-phase currents into the stator windings are sinusoidal and in phase with the 3-phase induced e.m.f.s. According to [5], this produced torque is given by

$$T = \frac{3 i_m e_m}{2\omega_m} = KI \tag{2.3}$$

where T is the total torque, i_m is the amplitude of the sinusoidal current, e_m is the amplitude of the sinusoidal e.m.f. , ω_m is the angular mechanical speed, K is known as the motor constant, while I is the rms value of the current.

According to [16], the basis for the control scheme of the PM synchronous motor is the two-axis machine model. DC quantities can be controlled using a PI controller which can be implemented easily. As mentioned earlier, the wave forms of the induced e.m.f., current, and flux in the PM synchronous machine are sinusoidal. This means that using a rotating dq reference frame will help in obtaining these waveforms in a DC form.

The concept of the rotating dq reference frame is mainly based on the mathematical approaches known as Park and Clarke transformations. The transformation between three-phase and two-phase systems (known as Clarke transformation and considering amplitude invariant transformation [17]) can be given by

$$\begin{bmatrix} S_\alpha \\ S_\beta \end{bmatrix} = \frac{2}{3}\begin{bmatrix} 1 & -\frac{1}{2} & -\frac{1}{2} \\ 0 & \frac{\sqrt{3}}{2} & -\frac{\sqrt{3}}{2} \end{bmatrix}\begin{bmatrix} S_a \\ S_b \\ S_c \end{bmatrix}, \quad \begin{bmatrix} S_a \\ S_b \\ S_c \end{bmatrix} = \begin{bmatrix} 1 & 0 \\ -\frac{1}{2} & \frac{\sqrt{3}}{2} \\ -\frac{1}{2} & -\frac{\sqrt{3}}{2} \end{bmatrix}\begin{bmatrix} S_\alpha \\ S_\beta \end{bmatrix} \tag{2.4}$$

, where this transformation is only valid when the three phase system is balanced (zero-sequence is negligible). Additionally, the transformation between rotating and stationary coordinate system (known as Park's transformation) can be given by

$$\underline{u}^s = \underline{u}e^{j\theta},\ \underline{u} = \underline{u}^s e^{-j\theta},\ e^{j\theta} = \cos\theta + j\sin\theta \tag{2.5}$$

$$\begin{bmatrix} u_\alpha \\ \\ u_\beta \end{bmatrix} = \begin{bmatrix} \cos\theta & -\sin\theta \\ \\ \sin\theta & \cos\theta \end{bmatrix} \begin{bmatrix} u_d \\ \\ u_q \end{bmatrix},\ \begin{bmatrix} u_d \\ \\ u_q \end{bmatrix} = \begin{bmatrix} \cos\theta & \sin\theta \\ \\ -\sin\theta & \cos\theta \end{bmatrix} \begin{bmatrix} u_\alpha \\ \\ u_\beta \end{bmatrix} \tag{2.6}$$

[17].

By using amplitude invariant transformation between the three-phase system and the two-phase stationary system and then another transformation between that stationary system and a rotating system, it is easy to obtain the conventional model for a PM synchronous motor in the dq reference frame [16]

$$V_d = R_s i_d + L_d \frac{di_d}{dt} - L_q \frac{p}{2}\Omega_r i_q \tag{2.7}$$

$$V_q = R_s i_q + L_q \frac{di_q}{dt} + L_d \frac{p}{2}\Omega_r i_d + \lambda \frac{p}{2}\Omega_r \tag{2.8}$$

where V_d, V_q are the d-q axes voltages, L_d, L_q are the d-q axes inductances, i_d, i_q are the d-q axes currents, Ω_r is the rotational speed, R_s is the stator windings resistance, p is the pole-number of the machine, λ is the amplitude of the flux induced by the permanent magnets. These equations are valid for a balanced three phase system and a salient machine where L_d and L_q are not equal.

It is worth mentioning that this conventional model for the PMSM may result in inaccurate calculations if it is used for parameter predictions [16]. To make this model suitable for this kind of predictions, some modifications need to be done. It should consider the effect of the load and saturation, the influence of anisotropy determined by the rotor position and the current phase angles, and the cross-coupling between the quadrature and direct axes. These modifications will be discussed in details in chapter 4.

2.2.4 Saliency

As mentioned in 2.2.2, the direct axis inductance is the stator inductance when the direct axis or magnets are aligned with the stator winding. While, the quadrature

axis inductance is the inductance measured in the position obtained by rotating the magnets from the aligned position by 90° where the stator flux sees the interpolar area of the rotor containing only the iron path. The value of the quadrature axis inductance is mostly higher than that of the direct axis inductance in PM synchronous machines [17] i.e.

$$L_q > L_d \tag{2.9}$$

where L_q and L_d are the quadrature axis and the direct axis inductances respectively. This is due to the difference between the effective air gap length of the direct axis and that of the quadrature axis [13]. In Figure 2.3, it can be seen clearly that this difference is due to the various motor geometries as well as the position of the permanent magnets (whose permeability is close to that of air) on the rotor. It is worth mentioning that (2.9) is not valid for the configuration in Figure 2.3d. This opens the door to another important term which is related to permanent magnet synchronous machines. This term is called: "saliency" which can be defined as the difference between the values of the quadrature axis and the direct axis inductances. Due to this saliency, another torque is produced in the machine in addition to the synchronous torque which is known as reluctance torque [13]. This torque can be given by

$$T_R = \frac{1}{2} i^2 \frac{dL}{d\theta} \tag{2.10}$$

where T_R is the reluctance torque, i is the stator current, L is the inductance, and θ is the angle of rotor rotation [5]. Also, saliency is a very important characteristic in the PM synchronous machine which can be used in the estimation of the rotor position by saliency tracking [18].

2.3 Practical machine design terms

In this section, some practical terms which are needed for machine design will be discussed. There terms have a great impact on the designed machine performance and behavior. They can distinguish one machine from the other. The discussed terms are: iron losses, stacking factor, permanent magnets, and cogging torque.

2.3.1 Iron losses

When the alternating current (AC) is used, the electrical steel is subjected to some kind of power loss. This power loss is a function of the frequency of that alternating current and the magnetic flux density. It increases as the frequency and the flux

density increases. The reason for this loss is: magnetic hysteresis, eddy currents, and the so called "anomalous loss". The "anomalous loss" is related to domain wall movement and is not often accounted for in empirical expressions of the iron loss [19].

Steel suppliers usually provide loss data for different kinds of steel. A sinusoidal flux waveform is applied to a sample of laminations and the measurements are recorded. Steinmetz equation is a good representation of the power loss and it has separate terms for hysteresis and eddy-current loss [19]

$$P = C_h f {B_{pk}}^n + C_e f^2 {B_{pk}}^2 \tag{2.11}$$

where P is the power loss measured in W/Kg, f is the frequency in Hz, B_{pk} is the peak flux density of the sinusoidal flux density [T], C_h is the hysteresis loss coefficient, C_e is the eddy-current loss coefficient, and n is an exponent that varies to a certain extent with B_{pk} but it is often assumed to be 1.6 - 1.8.

2.3.2 Stacking factor

The stacking factor is also known as the laminations factor or the space factor. As mentioned in section 2.2.1, the stator core and similarly the rotor core are mainly made of laminated sheets (reducing eddy currents). These thin sheets are added together with some kind of insulation in between so that they don't contact each other. As a direct result of that, the depth of the core is not entirely made of a ferro-magnetic material. The ratio between the effective length of the ferro-magnetic core and the total apparent length including the insulation is known as the stacking factor,

$$K_s = \frac{L_{eff}}{L_{app}} \tag{2.12}$$

where L_{eff} is the effective length of the ferro-magnetic core and L_{app} is the total apparent length including the insulation. This factor is always less than one for a laminated core.

2.3.3 Permanent magnets

Materials that are able to keep magnetism like permanent magnets were applied in electrical machine research in the 1950s [13]. According to [15], the permanent magnets that are used for electric motors are divided into three categories:

1. Alnicos: They are a group of iron (Fe) alloys. In addition to iron (Fe), they

are composed of aluminum (Al), nickel (Ni), and cobalt (Co).

2. Ceramics (ferrites): They are a type of ceramic compounds composed of a chemical combination of iron oxide (Fe_2O_3) and other metallic elements. Some examples are: barium ferrite ($BaOx6Fe_2O_3$), and strontium ferrite ($SrOx6Fe_2O_3$).

3. Rare-earth materials: They are alloys made from rare earth raw materials. The high price of these raw materials has prohibited the large scale use. Some examples are: samarium-cobalt ($SmCo$), and neodymium-iron-boron ($NdFeB$).

Alnicos are used when high magnetic remanent flux density, low temperature coefficients, and high maximum service temperature (520 °C) are needed [15]. While, ceramics (ferrites) are preferred when low cost and very high electric resistance (no eddy-current losses in the permanent magnet volume) are required [15]. The main advantages of the rare-earth materials are high remanence and high coercive force which result in a larger energy density when compared to ferrites [15].

One of the most important curves that are used in the design and analysis of electric machines is the demagnetization curve which can be seen in Figure 2.4. It helps in the prediction of the effect of the external magnetic field intensity (coming from the stator winding for example) on the existing permanent magnets. It is worth mentioning that for all curves in Figure 2.4, when the magnetic field intensity equals zero (H=0), the curve passes through the point known as remanent flux density (B_r). While the magnetic field intensity (H) required to bring the magnetic flux density to zero (B=0) is known as the coercive force or coercivity (H_c).

2.3.4 Cogging torque

It is an electromagnetic torque which is found in the permanent magnet machines even when there is no excitation in the stator windings. The reason for such a kind of torque is the interaction between the stator teeth and the permanent magnets' field of the rotor. The field around a stator tooth changes when the rotor is approaching or leaving it. This results in a change of the coenergy in the air space between the magnet and the tooth. Thus, a net torque is produced which is known as the "cogging torque" [13].

The cogging torque is periodic and almost symmetric about its angular axis. The relation between the mechanical revolutions of the motor and the cogging torque cycles can be obtained by

$$N_{co} = LCM(s, p) \tag{2.13}$$

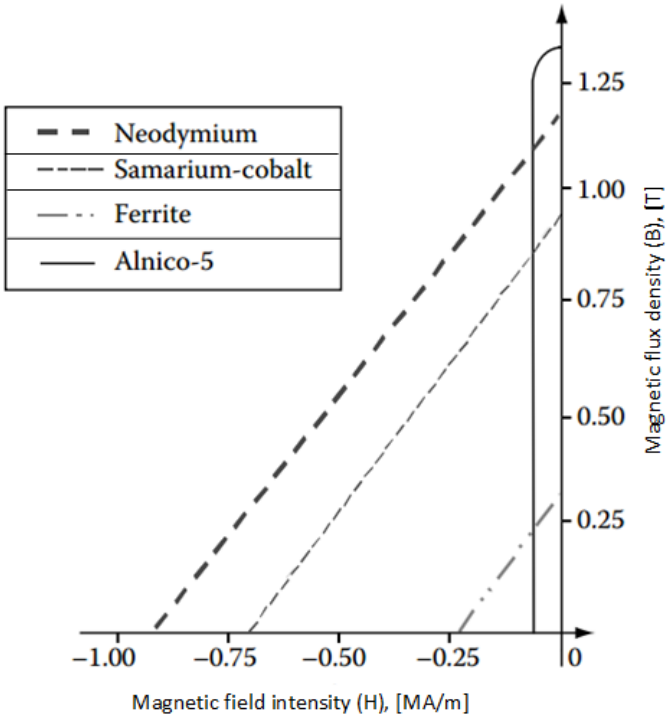

Figure 2.4:
The generic B–H demagnetization characteristics of some materials for second quadrant only [13].

where N_{co} is the number of cogging cycles per mechanical revolution, and $LCM(s, p)$ is least common multiple between the number of slots (s) and number of rotor poles (p). As a general rule, it is better to have a high number of cogging cycles per mechanical revolution. When this number increases, the cogging torque magnitude decreases which means a better machine performance [13].

The cogging torque has a fundamental frequency of N_{co}. A modeling of the cogging torque can be done as a Fourier sum of harmonics starting from fundamental to other higher order harmonics. This can be written as

$$T_{co} = \sum_{n=1}^{\infty} T_n \sin(nN_{co}\theta + \phi_n) \tag{2.14}$$

where T_{co} is the cogging torque, θ is the mechanical rotor position, ϕ_n is the phase shift of the component n, and $n = 1$ corresponds to fundamental T_1 which gives the peak fundamental of the cogging torque.

2.4 Vector control of PMSM

The block diagram of a typical vector control system of the permanent magnet synchronous motor can be shown in Figure 2.5. As seen from the figure, the measured rotor position is needed in the control system. It is mainly needed for the dq transformation of the three phase quantities. However, in the sensorless control technology the drive system is able to detect the rotor position and perform the vector control without any need for a position sensor.

The dq transformation helps in converting the sinusoidal quantities into DC ones. These DC quantities can be controlled using a PI controller which can be implemented easily. As seen from Figure 2.5, an inverter is supplying the permanent magnet synchronous motor with a three phase voltage. The motor's three phase stator currents as well as its speed and rotor position are measured using the suitable sensors. The three phase stator currents are then converted using the dq transformation and rotor position into a DC quantity which is fed into the current controller. The desired current reference value is obtained from the torque reference using the current reference calculation block. The measured current (DC quantity) as well as the current reference value are fed into the current controller which calculates using the measured speed the desired value of the stator voltage in a DC quantity. After that, the resulting DC quantity of the stator voltage is transformed into a three phase voltage using the rotor position. This three phase stator voltage is used as a reference for the inverter.

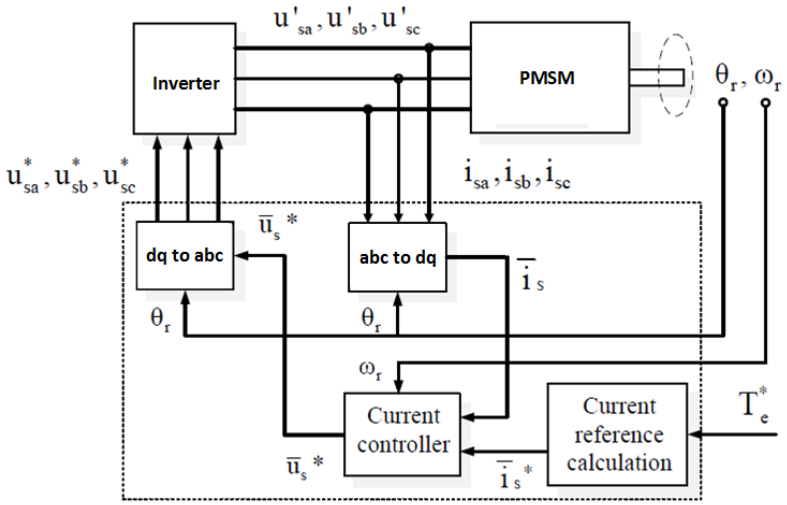

Figure 2.5:
Block diagram of a typical vector control system of PMSM with a position sensor [20].

3

Simulation: Motor

3.1 Introduction

In this chapter, the simulation of the permanent magnet synchronous motor will be discussed. As mentioned earlier in chapter 1, the aim of this study is the verification of a key performance indicator (KPI) that evaluates the quality of the potential sensorless vector control capabilities of a certain permanent magnet synchronous machine. To be able to reach that goal, an acceptable machine model needs to be created and its performance must be compared with the original simulated machine to make sure that it gives reliable results. Later, this machine will be considered as a base machine and some modifications will be performed on it to see their impact on the KPI as well as the sensorless position estimator. To have a model that is very close to the real life machine performance, a model based on Finite Element Analysis (FEA) is suggested. The software used for this is JMAG [11].

3.1.1 Finite Element Method

Computational electromagnetics (CEM) is a young field of study. It is still growing as there is an increasing demand for software tools that can be used in the design and the analysis of electrical devices. Twenty years ago, the design of most electrical devices was based on building and testing prototypes. This kind of design approach was slow and it had high costs. By introducing CEM, it was possible to decrease both time and costs in the design process [21]. Nowadays, CEM is a very important design tool that is used in the industrial and the academic fields. In electric power engineering, CEM is used in the design and investigation of many devices like: electrical motors, generators, transformers, relays and others [21].

The quality and the performance of the CEM tools is increasing in a very fast way. This kind of increase is due to two reasons. The first reason is that the computers are growing steadily and the second reason is the improvements in the

algorithms which are used in the calculation. There are many different algorithms in the CEM field. Some examples of these algorithms are: Finite Differences (FD), the Finite Element Method (FEM), and the Boundary Element Method (BEM) [21]. The main goal of all of these algorithms is the application and the solution of Maxwell's equations [22].

Finite Difference methods are mainly discretizations of Maxwell's equations in differential form, using the field components, or the potentials, on a structured grid of points as unknowns. There are two disadvantages of the Finite Difference methods. The first is that they need uniform Cartesian (structured) grids to work well. The second is that they use the so-called staircase approximation of boundaries that are not aligned with the grid. The Finite Element Methods are able to approximate complex boundaries in a much better way. In these methods, the computational region is divided into unstructured grids (typically triangles in two dimensions and tetrahedra in three dimensions) [21]. Time-harmonic problems are mainly solved using Finite Element Methods. Their disadvantage is that they are slower in time-domain calculations. The Boundary Element Methods use discretizations of Maxwell's equations in integral form. The currents or charges on the surfaces of conductors and dielectrics are the unknowns. These methods come in handy when the problem involves open regions and when the current-carrying surfaces are small [21].

3.1.2 Maxwell's Equations

As mentioned earlier, the main goal of the Computational electromagnetics' algorithms is the solution of Maxwell's Equations. They are a set of equations that describe the behavior of both electric and magnetic fields and their interaction with different materials [22]. They are named after the famous physicist "James Clerk Maxwell". These equations are simply the results of a huge amount of experiments and it is not possible to derive them from any other equations. The initial formulation of these equations was in the form of twenty equations containing twenty variables. Later, a much simpler representation was formulated using vector notations.

As explained before, the initial formulation of these equations was much more complex and it had many variables. Nowadays, it is possible to represent them in the form of four differential equations [22]: Faraday's law

$$\nabla \times \mathbf{E} = -\frac{\partial \mathbf{B}}{\partial t} \tag{3.1}$$

, Ampere's law

$$\nabla \times \mathbf{H} = \mathbf{J} + \frac{\partial \mathbf{D}}{\partial t} \tag{3.2}$$

, Gauss's law

$$\nabla \cdot \mathbf{D} = \rho \tag{3.3}$$

and Gauss's law for magnetic fields

$$\nabla \cdot \mathbf{B} = 0 \tag{3.4}$$

where $\mathbf{H}$ is the magnetic field, $\mathbf{J}$ is the current density, $\mathbf{D}$ is the electric displacement, $\mathbf{E}$ is the electric field, $\mathbf{B}$ is the magnetic field density, ρ is the electric charge density, and t is the time variable. These equations are solved using the Computational electromagnetic software tools with different boundary conditions depending on the subject under study.

3.2 Motor Simulation

After understanding the concept and the operation principle of Finite Element Methods and that they use Maxwell's equations to solve electromagnetic problems, the motor simulation will be performed using the Computational electromagnetic software tool: JMAG [11]. Two important software features will be used: JMAG-Designer and JMAG-RT. Both of them are registered trademarks of JSOL Corporation [11]. The JMAG-Designer will be used to create a simulated model of the motor under study based on real-life dimensions. It will take into account all practical design requirements like: material selection, saturation and others. Based on the model created in JMAG-Designer, the JMAG-RT will create a block for the studied PM synchronous motor which enables power electronics circuit simulations with external programs such as Simulink using the result data of the Finite Element Method (FEM).

3.2.1 Motor Specifications

As mentioned in chapter 1, the permanent magnet synchronous motor (PMSM) is the main component of Bosch's engine compartment actuator (ECA - E) which was shown in Figure 1.1. In this section, a FEM model of this PM synchronous motor will be created based on real life dimensions and specifications. The specifications of the ECA - E are shown in Table 3.1. These data are collected from the internal report in Robert Bosch GmbH [6]. This report was based on a development study

of the engine compartment actuator (ECA - E) with respect to the magnetic and electric properties according to the specification of a consultant [6]. Table 3.1 includes information about the number of teeth, slots, poles, maximum current, rated mechanical speed and others. It is worth mentioning that the rated torque value obtained in Table 3.1 is based on machine testing at rated speed using a trapezoidal current waveform from an inverter [6]. In this study, the current waveforms will be sinusoidal. This means that the value of this rated torque will be bigger as the simulation will be performed using a sinusoidal current waveform instead.

Table 3.1: Specifications of the Permanent Magnet Synchronous motor [6].

Parameter	Unit	Value
Number of slots and teeth		12
Number of rotor poles		10
Number of phases		3
Phase current maximum value	A peak	50.0
Rated mechanical speed	rpm	2000
Rated Torque	Nm	0.7
Motor constant	Nm/A	0.019
Machine active mass	kg	0.2053
Rotor moment of inertia	$kg\ mm^2$	5.0578

It is clear from the internal report [6] that the rotor of the studied motor has ten grooves which are designed for placing the magnets. There are some holes in the rotor structure. These holes are intended for two main reasons. The first reason is the control of the magnetic flux path in the rotor structure. The second reason is practical manufacturing requirements which are needed for motor mechanical structure. It is also clear from the internal report that the magnet groove is not totally flat and it has some depths.

The studied motor has the magnets placed on the outer surface of the rotor core, in the grooves of the rotor. The cross section of the used magnets is rectangular and they fit perfectly in the designed rotor grooves. Thus, the studied motor is a Surface-Mounted PMSM similar to the motor in Figure 2.3a but the magnets have some depth in the rotor core. This is needed from the mechanical strength point of view. Also, this depth helps in increasing the difference between the quadrature and direct axes inductances which can be used in the estimation of the rotor position by saliency tracking [18].

The stator of the studied permanent magnet synchronous motor is similar to the typical stator structure of a PM synchronous motor discussed in chapter 2. The dimensions of the stator core are extracted from the internal report in Robert Bosch GmbH [6]. The stator has twelve teeth and twelve slots, which are

distributed in a circular way. Similar to the rotor, there are some holes in the stator structure. These holes are practical manufacturing requirements which are needed for the mechanical structure of the motor. It is also clear from the internal report [6] that the outer cylindrical surface of the stator is not totally smooth and it has some depths and grooves. It is worth mentioning that after building the stator core (composed of twelve teeth and slots), the twelve slots are filled with copper wires which are connected in the way shown in Figure 3.1.

The stator winding is based on a three-phase winding which can be seen in Figure 3.1. The specifications of the stator winding can be seen in Table 3.2 which are also extracted from the internal report in Bosch [6]. Table 3.2 includes information about the number of turns, circuit connection, phase resistance and others. The three phase winding of the studied motor is made of copper wires and connected in star (wye) which can be seen clearly in Figure 3.1.

Table 3.2: Specifications of the stator winding of the Permanent Magnet Synchronous motor [6].

Parameter	Value
Number of turns	14
Number of conductors per slot	28
Circuit connection	$Star(wye)$
Phase resistance at 20 °C	28.72 $m\Omega$

As seen from Figure 3.1, each phase consists of two series coils which are parallel with another two series coils. The resulting three phases are connected together in one point which is the neutral point of the star (wye) connection. The direction of the currents as well as the coil positions across the stator core are extracted from the internal report in Robert Bosch GmbH [6]. The final implementation can be seen later in Figure 3.9 where the numbers represent the orders of the coils. Figure 3.9 is only for the 2D half model so the coils (7, 8, 9, 10, 11, and 12) are not shown but they also follow the same anti-periodic condition which is discussed in detail in section 3.2.3.

The material information for the selected PM synchronous motor is extracted from the internal report in Bosch [6]. According to [6], the motor shaft is made from the steel material ST 37-100 and the stator and the rotor cores are made from another steel material M800-65A. The permanent magnets are made from neodymium-iron-boron ($NdFeB$) which is a Rare-earth magnetic material as discussed in chapter 2. Finally, the stator winding is made from copper conductors. The material data collected can be shown in Table 3.3.

In Figure 3.2a, the typical curve between the magnetic field intensity (H)

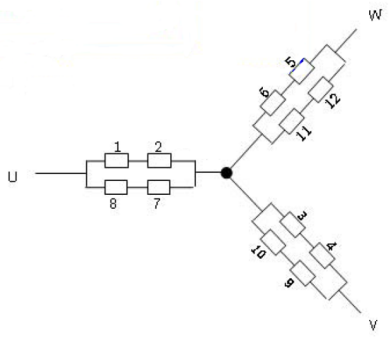

Figure 3.1:
Circuit diagram of the three-phase stator winding of the Permanent Magnet Synchronous motor [6].

Table 3.3: Materials of different parts of the Permanent Magnet Synchronous motor [6].

Part	Material
Shaft	ST 37-100
Rotor Core	M800-65A
Permanent magnets	NdFeB
Stator Core	M800-65A
Stator Winding	Copper

and the magnetic flux density (B) is shown for the steel material: ST 37-100. This typical B-H curve was obtained by the aid of the Steel Database found in the software "SPEED" [23]. The density of the steel material was found to be equal to 7860 kg/m^3 [24]. For the steel material M800-65A, the typical B-H curve is shown in Figure 3.2b. This typical B-H curve was also obtained by the aid of the Steel Database in "SPEED" [23]. The density of the steel material M800-65A was found to be equal to 7800 kg/m^3 and this value was also obtained from the Steel Database in "SPEED". According to [23], the thickness of one layer of the steel material M800-65A is equal to 0.65 mm. From Table 3.1, it is seen that the depth of both rotor and stator cores is equal to 20 mm. From these two facts, it is easy to calculate the number of layers to form each of the stator core and the rotor core which is 30 $layers$. This means that the effective length of the ferro-magnetic core (L_{eff}) is equal to 19.5 mm and the the total apparent length including the insulation (L_{app}) is equal to 20 mm. By using (2.12), the stacking factor (K_s) of both the stator and rotor cores is equal to 0.975.

For the calculation of the iron losses of the steel material M800-65A, the Steinmetz equation (2.11) discussed in chapter 2 can be used. The coefficients and powers in (2.11) related to the steel material M800-65A can be obtained from the Steels

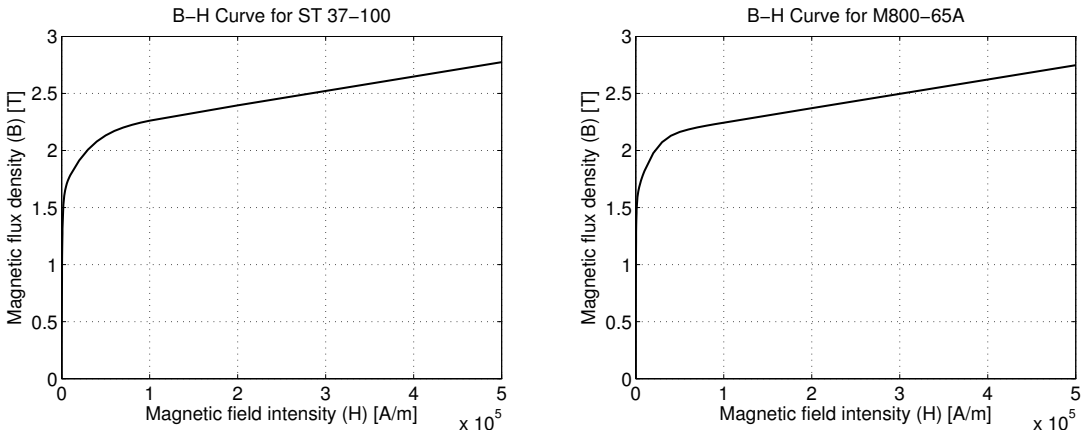

(a) **(b)**

Figure 3.2:
B-H Curves for a) ST 37-100 and b) M800-65A [23]

Database in "SPEED" [23] and they are shown in Table 3.4.

Table 3.4: The obtained coefficients and exponents in (2.11) related to the steel material: M800-65A [23].

Coefficient or Exponent	Value
C_h	0.021959
n	1.7
C_e	0.00025623

As shown in Table 3.3, the permanent magnets of the studied PM synchronous motor are made from neodymium-iron-boron ($NdFeB$). The remanent flux density (B_r), and the coercive force or coercivity (H_c) of the studied motor are found to be equal to 1.22 T and -924.61 kA/m respectively [6]. By using these two values, a similar curve to the one shown in Figure 2.4 and discussed in chapter 2 can be obtained. This curve can be shown in Figure 3.3 and it will used to define the magnets in JMAG. As seen, it is a linear curve which has a positive slope.

3.2.2 Real Life Machine Performance

In this section, the real-life machine performance and operation (the induced e.m.f., the cogging torque, and the rated torque) are discussed according to the internal report in Robert Bosch GmbH [6]. It is worth mentioning that all the curves obtained in this section are based on lab testing which was presented in the internal report [6]. Figure 3.4 shows the induced e.m.f. as function of rotor position in electrical degrees for a mechanical speed of 2000 rpm. The Figure 3.4 has three curves: one

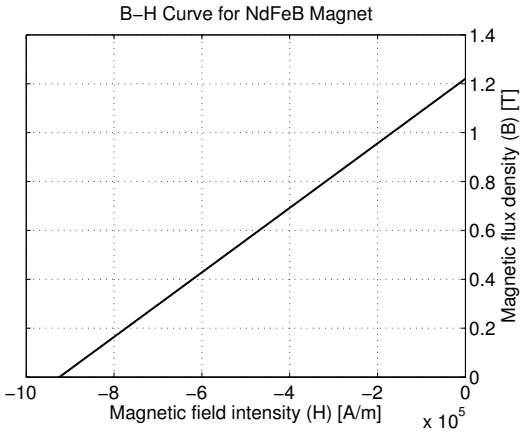

Figure 3.3:
The B–H demagnetization characteristics of the permanent magnets of the Permanent Magnet Synchronous motor for second quadrant only.

for the measured value (green), and the other two are based on software simulations. As seen from Figure 3.4, the curve has a sinusoidal waveform which agrees with the discussion in section 2.2.3 in chapter 2. According to the figure, the maximum value of the induced e.m.f. is equal to 1 *pu* where the base is selected as the peak value of the simulated induced e.m.f., as seen in the figure.

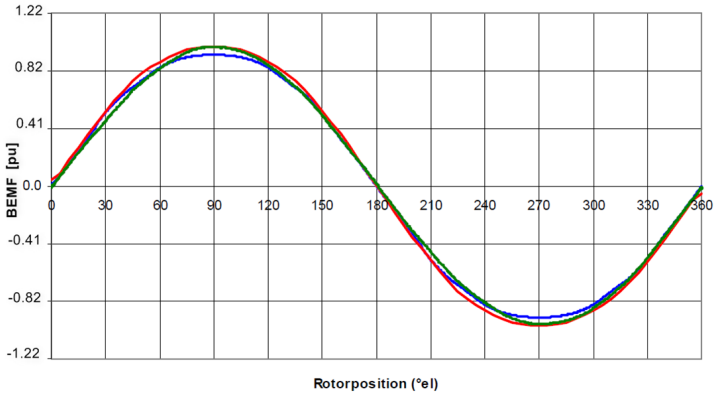

Figure 3.4:
Comparison of the induced e.m.f. at 2000 rpm: measured (green), and SPEED software simulation (blue) and FEMAG software simulation (red) [6].

Figure 3.5 shows the measured cogging torque in *p.u.* as function of the rotor position in mechanical degrees, where the base is selected as the average value of the simulated rated torque that is seen in Figure 3.16. It is clear that the waveform is distorted which may be due to the measurement disturbance which can be caused by electromagnetic interference. The Figure 3.5 has two curves: one for the anti-

clockwise rotation (pink), and the other for the clockwise rotation (blue). The two curves are different from each other because of the variation in the position relative to the teeth as well as the measurement disturbance which causes the distortion.

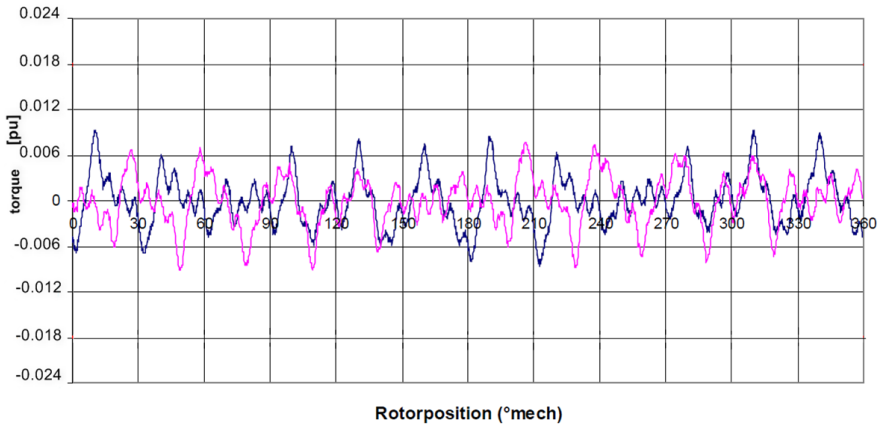

Figure 3.5:
Measured cogging torque of the Permanent Magnet Synchronous motor: anticlockwise rotation (pink) and clockwise rotation (blue) [6].

According to Table 3.1, the number of the slots (s) and the number of the rotor poles (p) of the studied PM synchronous motor are equal to 12 and 10 respectively. By using (2.13), the number of cogging cycles per one mechanical revolution (N_{co}) for the studied PM synchronous motor should be equal to 60. This also means that cogging torque period in mechanical degrees is equal to 6 °. As seen from Figure 3.5, the number of cogging cycles per one mechanical revolution (N_{co}) for the measured cogging torque as well as the cogging toque period agrees with the calculated values 60 and 6 ° respectively. But, it is clear that the cogging cycles are strongly distorted in the measurement in Figure 3.5. According to Figure 3.5, the peak-to-peak cogging torque is equal to 0.0169 pu which is also obtained from the internal report [6].

Figure 3.6 shows the measured torque in pu as function of the rotor speed, where the base is selected as the average value of the simulated rated torque that is seen in Figure 3.16. The Figure 3.6 has three curves for three different motor samples. As seen from Figure 3.6, the rated torque which is obtained at the rated speed (2000 rpm) is equal to 0.85 pu. It is worth mentioning that this value of the rated torque is based on machine testing at rated speed using a trapezoidal current waveform from an inverter [6]. If the used current waveform is sinusoidal, this value of the rated torque will be different due to the sinusoidal waveform. As seen in

Figure 3.6, the value of the measured torque differs in a small way from one sample to the other. This difference is bigger at low speed and it becomes smaller as the speed increases.

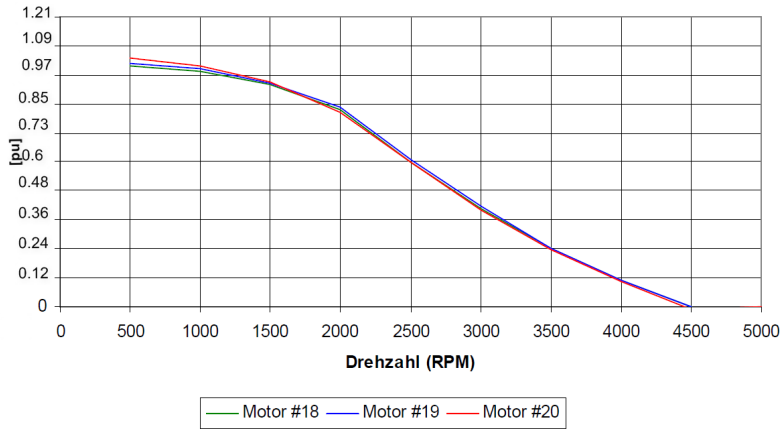

Figure 3.6:
Measured torque – speed curve of the Permanent Magnet Synchronous motor for three different motor samples (18, 19, 20) [6].

3.2.3 Simulation in JMAG-Designer

The specifications and the performance of the real-life PM synchronous motor in sections 3.2.1 and 3.2.2 are used for setting up the FEM simulation in JMAG-Designer and for validating the simulation results. JMAG-Designer is a registered trademarks of JSOL Corporation [11] and it is used to create a simulation model of the motor under study, based on real-life dimensions. All practical design requirements like: material selection, saturation and others are taken into account. The procedure of creating the model can be divided into a group of steps which are: creating the geometry, choosing the study type, setting the materials, creating the circuit, setting the study conditions, generating the mesh, running the analysis, displaying the results, modifying the circuit, running the analysis again, and displaying the results again. If every step is performed in the right way, the step "running the analysis" will be smooth and there will be no errors.

The final 2D half model that is created by the "geometry editor" is shown in Figure 3.7. The first step "creating the geometry" starts with setting the units that will be used, specifying the saving folder location, and identifying the geometric plane that will be used (XY Plane as this is a 2D study). In this step, the "geometry editor" of JMAG is used. It is worth mentioning that a 2D half model can be created for this analysis because the geometry of the motor has a mirrored symmetry, and

its magnetic field distribution has a periodicity (antiperiodic, i.e. the magnetic field distribution reverses every 180 ° which is set in the condition "Rotation Periodic Boundary"). This offers a more efficient analysis because the size of the model is smaller. Consequently, the software calculation time will be smaller. Also, it is not practical if the cross section of each wire of the conductors forming the coils in the stator winding is drawn separately. Each cross section of the coils in the stator winding can be modeled as one region if the current flowing through the coil regions is distributed uniformly. This kind of approximation will not have a big impact on the study scope [11]. It is worth mentioning that a 2D quarter model is not created because of circuit restrictions. Using the basic shapes of the "geometry editor" and

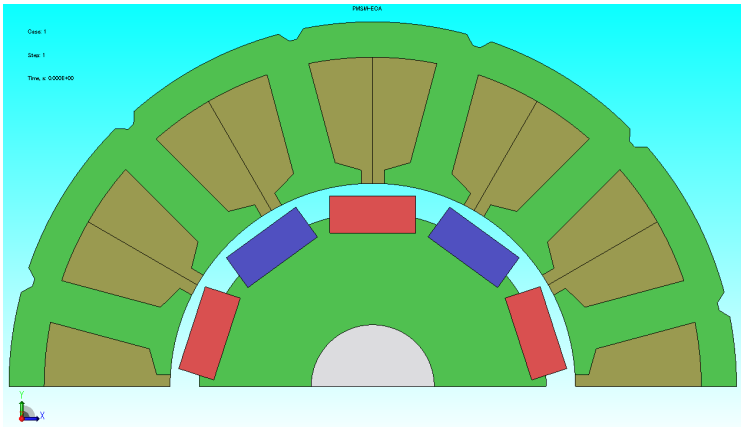

Figure 3.7:
The final 2D half model created by the "geometry editor" including the shaft, rotor core, permanent magnets, stator core, and stator winding.

based on the dimensions extracted from the internal report [6], the 2D half model, including the shaft, rotor core, permanent magnets, stator core, and stator winding can be created as shown in Figure 3.7. Some geometric approximations have been made ignoring some fillets, holes, and others based on the fact that this kind of approximation will not have a big impact on the study scope as the studied machine will be used as a base model and any modification will be compared with it.

After creating the geometry, the type of the study that will be performed needs to be selected. In this study, the "Magnetic Transient Analysis" study type has been chosen. This study type is suitable for motors and machines as the analysis target has time-varying phenomena such as motion and current variations [11].

The next step is setting the materials of the different parts of the studied permanent magnet synchronous motor. This step is performed based on the motor specifications in section 3.2.1 as well as the data extracted from the Table 3.3. It is simply performed by the "drag-and-drop" feature of JMAG. Each material is selected from the materials library in JMAG and dropped on the related geometric

part of the motor. As more customized materials that are directly related to the studied motor are needed for the parts: shaft, rotor and stator cores, and permanent magnets, the "create new material" feature of the materials library is used to create the materials: ST 37-100, M800-65A, and NdFeB. For the ST 37-100, the B-H curve is inserted based on the Figure 3.2a. Also, the mechanical properties (like density) which is mentioned in section 3.2.1 are inserted. The iron losses for ST 37-100 (shaft) are ignored in this study as this kind of approximation will not have a big impact on the study scope as no modifications will be made to the shaft and the studied machine will be used as a base model and any modification will be compared with it. For the M800-65A, the B-H curve is inserted based on the Figure 3.2b. Also, the mechanical properties (like density and stacking factor for both stator and rotor cores) which are mentioned in section 3.2.1 are inserted. The iron losses equation for M800-65A is inserted based on the Steinmetz equation (2.11) and the values in Table 3.4. For the NdFeB, the B-H demagnetization curve is inserted based on Figure 3.3. Also, the mechanical properties (like density) is inserted as 7850 kg/m^3 which is the default value in JMAG. The iron losses for NdFeB are ignored in this study as this kind of approximation will not have a big impact on the study scope as no modifications will be made to the magnets and the studied machine will be used as a base model and any modification will be compared with it. The settings for the permanent magnets made from NdFeB are inserted as in Table 3.5.

Table 3.5: The settings for the permanent magnets made from NdFeB of the permanent magnet synchronous motor in JMAG.

Item	Parameter
Magnetization Pattern	$ParallelPattern$ ($CircularDirection$)
Number of poles	10
Angle from Reference Axis	18 °
Start Point (Value is saved) (X, Y)	$(0, 0)$
Reference Axis Direction (Value is saved) (X, Y)	$(1, 0)$

After material selection, the circuit of the motor should be created. Based on Figure 3.1, the 3-phase stator winding is connected in a star (wye) form. The values inserted for the stator winding are obtained from Table 3.2. The circuit connection for the 3-phase stator winding in JMAG can be shown in Figures 3.8a and 3.8b. The Figure 3.8a shows an overview of the circuit connection with an electric potential probe on each phase which is needed for the induced e.m.f. measurement. The Figure 3.8b shows the detailed structure of the star (wye) connection.

The step "setting the study conditions" includes a group of conditions which are needed to create an operation scenario which is similar to the real-life machine

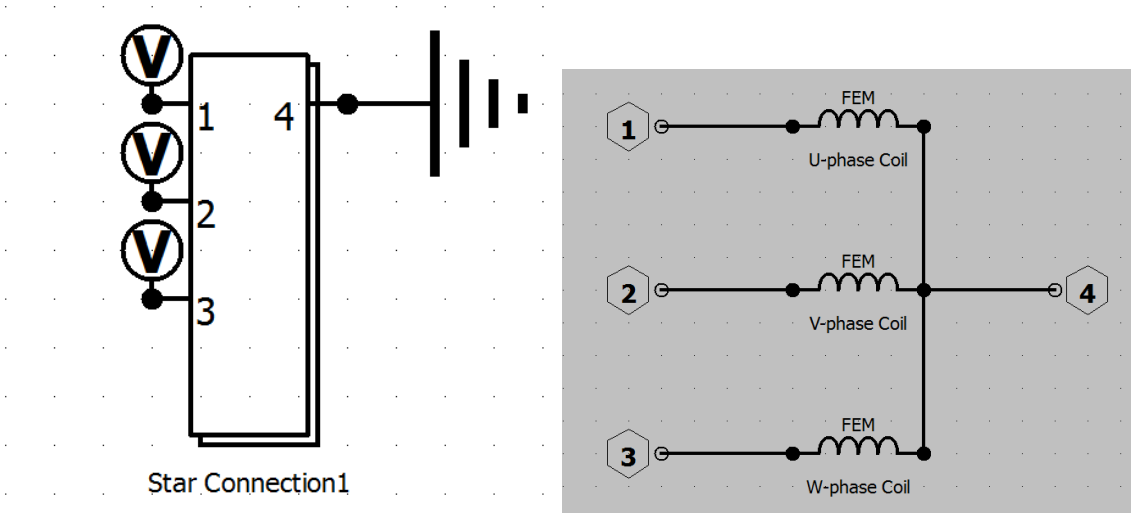

(a) (b)

Figure 3.8:
The circuit connection for the 3-phase stator winding in JMAG a) overview and b) detailed star connection.

performance. The first condition selected is "Motion: Rotation". This condition specifies the motion of the motor. For this condition, the machine parts: rotor core, shaft, and the permanent magnets are selected to be moving with a constant revolution speed which is equal to 2000 *rpm* (the rated motor speed) in the anticlockwise direction. The next condition is "Rotation Periodic Boundary". Since the model that is drawn by the "geometry editor" is only a half model because the geometry of the motor has a mirrored symmetry, and its magnetic field distribution has a periodicity, this condition must be specified to create the effect similar to the full model creation. The 2D half model used for this analysis has a periodic angle of 180 ° and a periodicity that is anti-periodic because the magnetic field distribution reverses every 180 °. As shown in Figure 3.7, the second half of full 2D model will be exactly the same in terms of geometry but the magnets will be reversed. Therefore, the periodicity is selected to be antiperiodic and the periodic angle is chosen to be 180 ° for the condition "Rotation Periodic Boundary". Another condition that is needed is "Torque: Nodal Force". This condition is set to obtain the torque for a specified part. The value of the torque is positive if the rotor rotates in the counterclockwise direction (which is the direction of rotation of this study). For this condition, the "Setting Target" is selected to be "Motion Region" which is the rotor in this study. Another important condition is "FEM Coil". This condition is set to link the coils in the geometric model (stator winding) and the FEM coils in the created circuits which can be seen in Figure 3.8b. The voltage generated in the coil terminal is calculated using the flux linkage of the coil. One "FEM Coil" is set for each phase

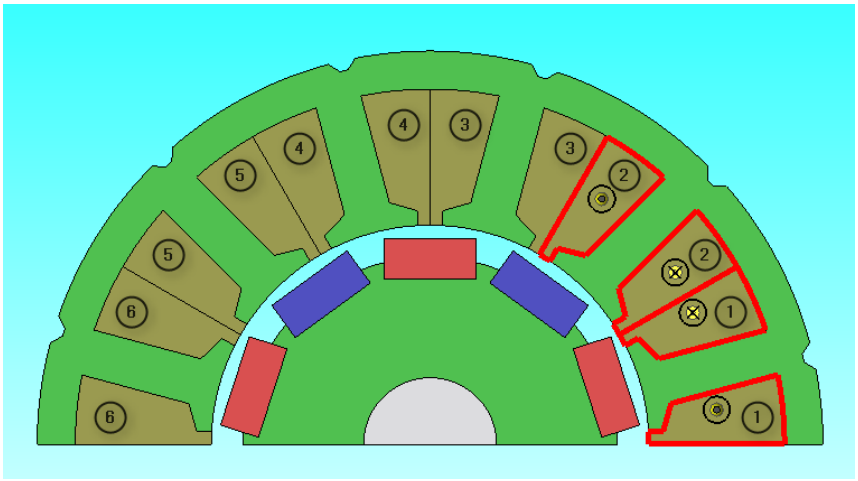

(a)

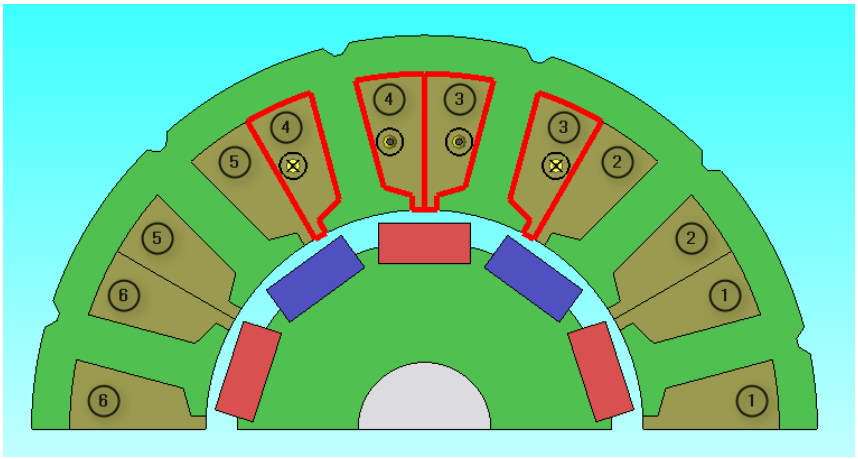

(b)

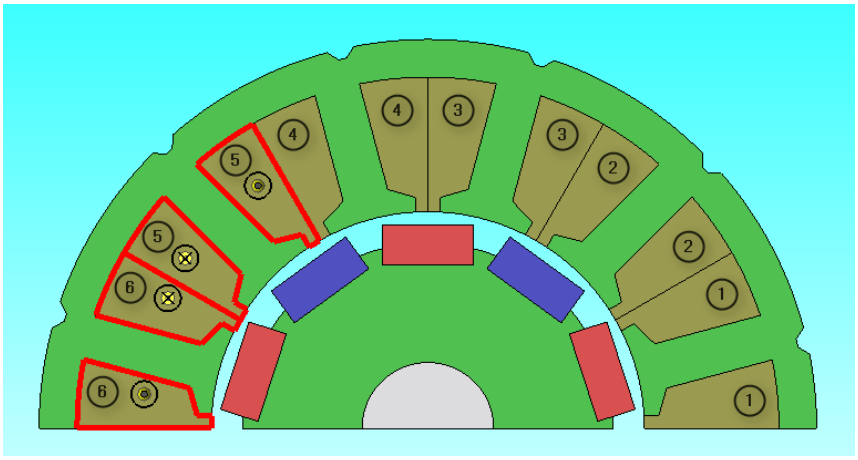

(c)

Figure 3.9:
The specified current flow directions in the three "FEM Coil" conditions for the a) U-phase, b) V-phase, and c) W-phase where the circle denotes the upward direction while the cross denotes the downward direction.

(three phases in this study). The current flow direction is set for each "FEM Coil" based on the internal report [6]. The specified current flow directions in the three "FEM Coil" conditions for the U-phase, V-phase, and W-phase are shown in Figures 3.9a, 3.9b and 3.9c respectively where the circle denotes the upward direction while the cross denotes the downward direction of the current. Finally, the condition "Iron loss calculation" needs to be added. The function of this condition is to calculate the iron losses discussed in chapter 2 based on the selected materials and their characteristics.

It is worth mentioning that some properties of the software for this study need to be set. The first property is "step control". This property affects both the calculation time and the accuracy of the analysis. It specifies the time step by which the JMAG-Designer calculates and stores quantities. The shorter time step gives more accurate results but the amount of time for the analysis increases. Thus, the time step should be selected based on a balance between the needed accuracy and calculation time. For this study, this property is selected to be set automatically based on the motion condition. But, the results obtained in Figure 3.15 are based on a "step control" which has 20 steps of calculation in one cogging torque period. This is needed to give a more detailed view of the cogging torque profile. Another property is "Full Model Conversion". It is a very important property as it converts the half 2D model quantities to the full model ones. The depth of the studied machine is inserted as 20 mm based on Table 3.1. The next property is "circuit settings". This property is needed to create the complete circuit connection (shown in Figure 3.1) of the studied motor as the "FEM Coil" condition shown in Figure 3.9 doesn't include the parallel branches.

The step "generating the mesh" is needed to divide the geometric structure into a grid (a mesh) where Maxwell's Equation discussed in section 3.1.2 can be applied. The simulation has a rotational motion as the simulated device is an electric motor. Thus, the "Slide Mesh" option is needed to account for this motion. Also, a satisfactory element size should be selected to have an accurate analysis. The final mesh structure selected for this study is shown in Figure 3.10. Also, a detailed view of the "Slide Mesh" option in the final mesh structure can be shown in Figure 3.11. It is clear from Figure 3.11 that the "Slide Mesh" is composed of six rows and that its elements are smaller than the other ones. The elements of the "Slide Mesh" are found in the air gap.

Finally, the steps "running the analysis" and "displaying the results" should be performed. As mentioned earlier, if every step is performed in the right way, the step "running the analysis" will be smooth and there will be no errors. The results obtained for this simulation study are discussed in section 3.2.4. The induced

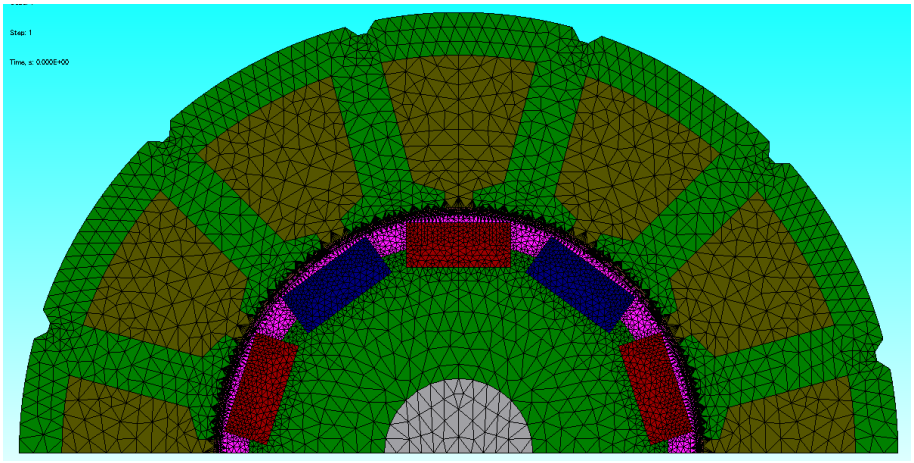

Figure 3.10:
The final mesh structure selected for the study including the "Slide Mesh" option.

e.m.f. (Figure 3.14) and the cogging torque (Figure 3.15) are generated based on the circuit connection shown in Figure 3.8. To generate the rated torque (Figure 3.16), a circuit modification is needed. According to chapter 2, a constant output power (constant torque) can be produced on one condition. That condition is that the injected 3-phase currents into the stator windings are sinusoidal and in phase with the 3-phase induced e.m.f. Thus, the circuit connection is modified to include a 3-phase sinusoidal current source which is in phase with the 3-phase induced e.m.f. Its amplitude is 50 A based on Table 3.1 and its frequency is 166.6667 Hz based on (2.1) (number of poles = 10 and the synchronous speed is 2000 rpm). The modified circuit can be shown in Figure 3.12.

As mentioned in section 3.2, a block for the studied PM synchronous motor which enables power electronics circuit simulations with external programs such as Simulink using the result data of the Finite Element Method (FEM) will be created from the model in JMAG-Designer. The JMAG-RT tool will be used for that purpose. After the creation of the model in JMAG-Designer, the "JCF" file including the mesh data is exported. This file is imported in the JMAG-RT tool and the option "Spatial Harmonic Model" is selected as it takes into account the slot harmonics which is relevant to this study. Two types of blocks for the studied PM synchronous motor can be generated from the JMAG-RT tool which can be shown in Figure 3.13. The first (Figure 3.13a) is the "Current signal input" and it takes the load torque, the three phase currents, the coils temperature, and the magnet temperature as inputs and gives the rotation angle, the revolution speed, the generated torque, the total three phase flux linkages in the coils, and the quadrature and the direct axes inductances as outputs. This block will be used in the Simulink model used to obtain the key performance indicators that will be discussed in Chapter 4. While, the

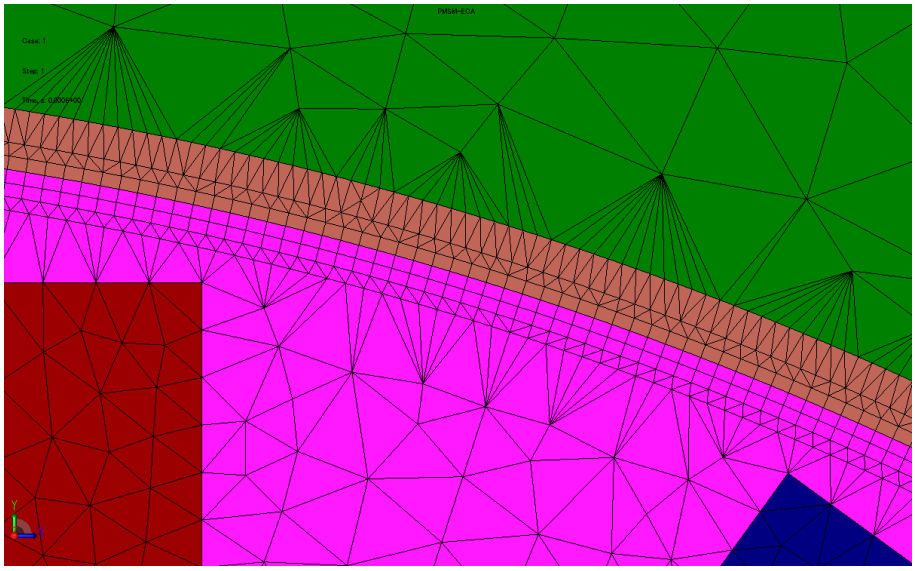

Figure 3.11:
A detailed view of the "Slide Mesh" option in the final mesh structure selected for the study.

second (Figure 3.13b) is the "Electric signal input" and it takes the load torque, the three phase voltages, the coils temperature, and the magnet temperature as inputs and gives the three phase currents, the rotation angle, the revolution speed, the generated torque, the hysteresis loss, the eddy current loss, the total three phase flux linkages in the coils, and the quadrature and the direct axes inductances as outputs. This block will be used in the Simulink model used for the verification of the key performance indicators that will be discussed in Chapter 6.

3.2.4 Simulated Machine Results

Similar to section 3.2.2, the induced e.m.f., the cogging torque, and the rated torque of the simulated motor are studied. If one complete electrical revolution of the machine is given by 360 °, the corresponding mechanical revolution can be easily calculated. According to Table 3.1, the number of the rotor poles (p) of the studied PM synchronous motor is equal to 10. Using (2.2) after integration (position instead of speed), the corresponding mechanical angle rotation is found to be equal to 72 °. It is worth mentioning that all the curves obtained in this section are based on a mechanical angle rotation of about 72 ° which is equivalent to one complete electrical revolution of the studied PM synchronous motor.

Figure 3.14 shows the simulated induced e.m.f. in pu on the y-axis and the rotor position in electrical degrees on the x-axis for one complete electrical revolution where the base is selected as the maximum value of the simulated induced e.m.f. in

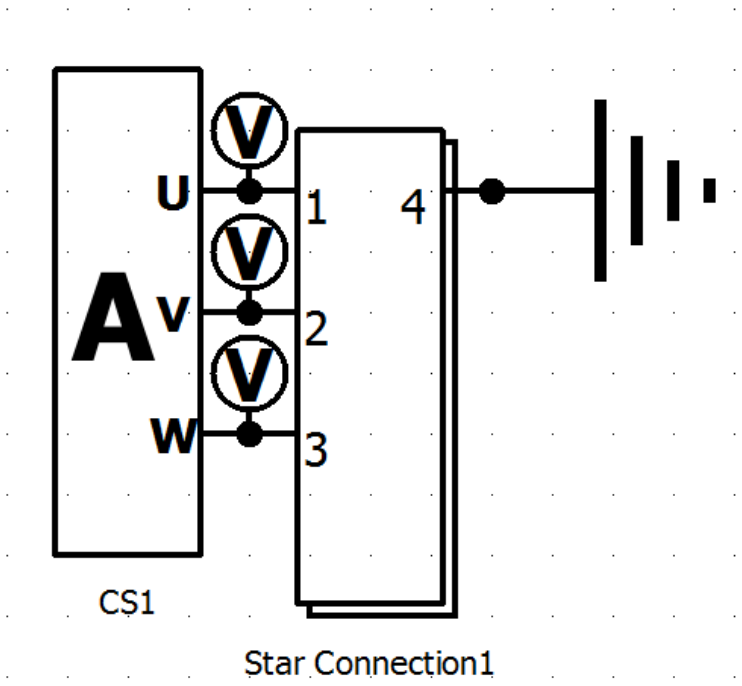

Figure 3.12:
The modified circuit connection for the 3-phase stator winding in JMAG to obtain the rated torque.

the same figure. As seen from Figure 3.14, the curve has a sinusoidal waveform which agrees with the discussion in chapter 2. According to Figure 3.14, the maximum value of the simulated induced e.m.f. is equal to 1 pu which agrees with value obtained from the real-life machine performance in Figure 3.4. By comparing the waveforms in Figures 3.4 and 3.14, it is clear that both are sinusoidal, they have the same maximum value (1 pu) and their periods are the same which are equal to 360 °. The waveform in Figure 3.14 is less smooth and this may be due to the selected time step in the simulation. A smaller time step will give a smoother waveform. Additionally, the waveform in Figure 3.14 starts at the value (0.5 pu) and not 0 pu as the one in Figure 3.4. This is due to the difference in the selected zero reference of the rotor position in both cases.

Figure 3.15 shows the simulated cogging torque in pu on the y-axis and rotor position in mechanical degrees on the x-axis for one quarter of one electrical revolution, equivalent to a mechanical angle rotation of about 18 °. The base torque is selected as the average value of the simulated rated torque that is seen in Figure 3.16. Figure 3.15 is based on the anticlockwise rotation of the rotor at a constant speed of 2000 rpm. As shown before, the number of cogging cycles per one mechanical revolution (N_{co}) for the studied PM synchronous motor should be equal to 60. This also means that cogging torque period in mechanical angle is equal to

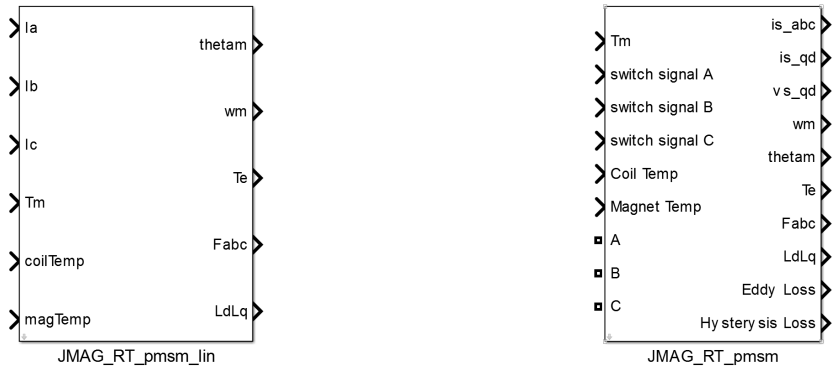

(a) **(b)**

Figure 3.13:
The Simulink blocks generated from the JMAG-RT tool for the studied PM synchronous motor: a) Current signal input model b) Electric signal input model.

6 °. As seen from Figure 3.15, the period of one simulated cogging torque cycle is equal to 6 °. This means that the number of simulated cogging cycles per one mechanical revolution (N_{co}) should be equal to 60 which agrees with both the calculated values and the values obtained from the real-life machine performance in Figure 3.5. According to Figure 3.15, the peak-to-peak cogging torque is equal to 0.0011 *pu* which is different from the value obtained in Figure 3.5 (0.0169 *pu*). This may be due to the measurement disturbance which causes the distortion in Figure 3.5. By comparing the waveforms in Figures 3.5 and 3.15, it is clear that the one in Figure 3.5 is strongly distorted. Thus, it is not easy to compare them. But, it is clear that the cogging toque periods are equal and they agree with the calculated value. Additionally, the peak-to-peak values are different due to the measurement disturbance.

According to chapter 2, a constant output power (constant torque) can be produced on one condition. That condition is that the injected 3-phase currents into the stator windings are sinusoidal and in phase with the 3-phase induced e.m.f.. Figure 3.16 shows the simulated produced torque in *pu* on the y-axis and the rotor position in mechanical degrees on the x-axis for one electrical revolution which is equivalent to a mechanical angle rotation of about 72 ° where the base is selected as the average value of the simulated rated torque in the same figure. Figure 3.16 is based on a constant rotor speed of 2000 *rpm* and a 3-phase sinusoidal current source which has a phase current maximum value of about 50 *A* and in phase with the 3-phase induced e.m.f.. As seen from Figure 3.16, the average value of the simulated produced torque is about 1 *pu*. The average value of the simulated produced torque in Figure 3.16 is different from the rated torque value obtained

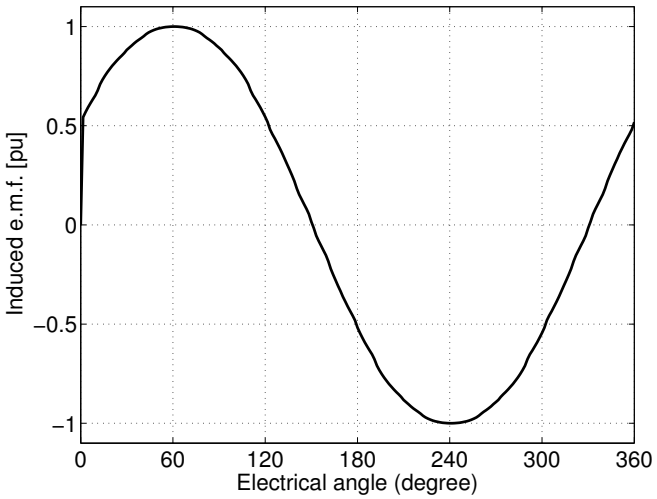

Figure 3.14:
Simulated induced e.m.f. (one phase) at 2000 rpm of the Permanent Magnet Synchronous motor (one complete electrical revolution equivalent to a mechanical angle rotation of about 72 °).

from the real-life machine performance from Figure 3.6. This is because the rated torque value obtained from the real-life machine performance in Figure 3.6 is based on machine testing at rated speed using a trapezoidal current waveform from an inverter [6].

3.3 Cost Calculation

The materials costs of the simulated machine (base model) are calculated as they will be compared with the costs of the modified machines in Chapter 6. The volumes of all parts of the machine are obtained in JMAG-Designer using the "Volume/Area Calculation" tool. After that, the masses are obtained using the information about the densities of materials, shown in Table 3.6. Finally, the costs are calculated based on the prices in Table 3.7. It is worth mentioning that the price of the steel material "M800-65A" in Table 3.7 includes also the stamping costs. Also, a copper fill factor of 0.4 is considered in the volume calculation of the stator winding [6]. The final costs calculation of the simulated Permanent Magnet Synchronous motor of Bosch's engine compartment actuator (ECA - E) can be shown in Table 3.8. This price doesn't include the end winding, outer housing, bearings, power electronics, and others.

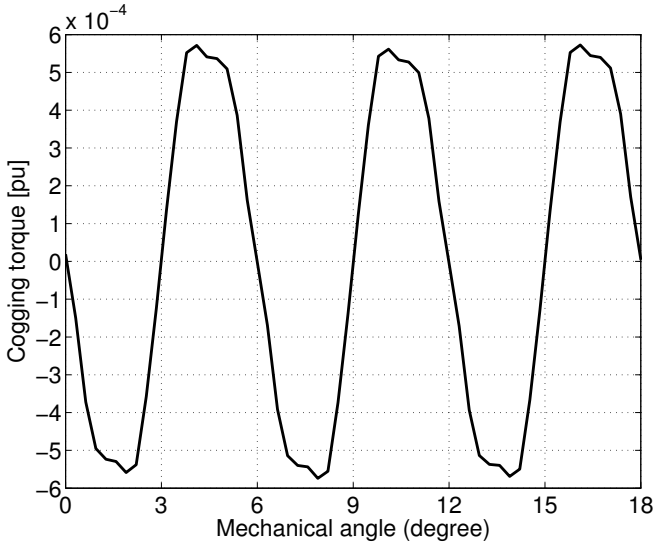

Figure 3.15:
Simulated cogging torque at 2000 rpm of the Permanent Magnet Synchronous motor (one quarter of one electrical revolution equivalent to a mechanical angle rotation of about 18 °).

Table 3.6: The densities of the materials of different parts of the Permanent Magnet Synchronous motor.

Part	Material	Density
Shaft	ST 37-100	7860 kg/m^3
Rotor Core	M800-65A	7800 kg/m^3
Permanent magnets	NdFeB	7400 kg/m^3
Stator Core	M800-65A	7800 kg/m^3
Stator Winding	Copper	8930 kg/m^3

Table 3.7: Prices of the materials of different parts of the Permanent Magnet Synchronous motor.

Material	Price
ST 37-100	0.31 €/kg
M800-65A	2.8 €/kg
NdFeB	220 €/kg
Copper	8 €/kg

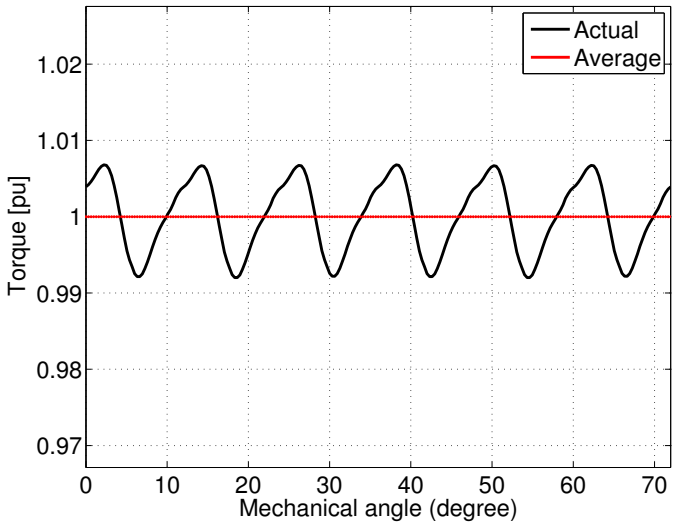

Figure 3.16:
Simulated rated torque which is obtained at the rated speed (2000 rpm) of the Permanent Magnet Synchronous motor (one complete electrical revolution equivalent to a mechanical angle rotation of about 72 °).

Table 3.8: The final costs calculation of the simulated Permanent Magnet Synchronous motor of Bosch's engine compartment actuator (ECA - E).

Part	Volume (mm^3)	Cost (€)
Shaft	1009.84	0.00246
Rotor Core	5665.49	0.12373
Stator Core	12717.10	0.27774
Magnets	2688.00	4.37606
Stator Winding	4588.76	0.32782
Total Cost (€)		5.10782

3.4 Conclusion

By comparing sections 3.2.2 and 3.2.4, it can be concluded easily that the simulated permanent magnet synchronous motor model in the Computational electromagnetic software tool (JMAG) has a similar performance when compared to the real-life performance of the permanent magnet synchronous motor in Bosch's engine compartment actuator (ECA - E) shown in Figure 1.1. The developed model is an acceptable representation of the real-life machine and it will be used in the investigations of the key performance indicator. As previously discussed, the simulated induced e.m.f. matches the one measured from the real-life machine performance as they are both sinusoidal, they have the same maximum value (1 pu), their periods are equal (360 °). However, the simulated waveform is less smooth due to the se-

lected time step. Additionally, the simulated cogging torque has the same number of cogging cycles per one mechanical revolution (N_{co}= 60) as well as the period (6 °) when compared with the measured and calculated one. But, it is noticed that the waveform of the measured one is strongly distorted and its peak-to-peak value (0.0169 *pu*) is different from the simulated value (0.0011 *pu*) which may be due to the measurement disturbance. Finally, the average value of the simulated rated torque is equal to 1 *pu* which is different from the measured one (0.85 *pu*). This can be explained by the difference in the used current waveform. To sum up, the simulated model doesn't fit perfectly when compared with the original machine, but it offers an acceptable motor performance which can be used in the next step.

4

Proposed Key Performance Indicator

In this chapter, the proposed key performance indicator is identified and discussed in details. This key performance indicator is used to evaluate the capability of a sensorless vector control system to perform the vector control of a certain PMSM with a good quality. The selected key performance indicator is primarily based on the work performed in the University of Nottingham and published in the "Power Electronics and Motion Control Conference" [16], [18]. The machine under study is the permanent magnet synchronous motor which is the main component of Bosch's engine compartment actuator (ECA - E) shown in Figure 1.1. This machine and its simulation methodology are discussed in details in chapter 3.

After the identification and the discussion of the KPI, the MATLAB and SIMULINK model proposed for its calculation will be discussed. Its components as well as its performance will be explained in details. Finally, the results obtained from that model will be presented. These results should be kept as a reference as they will be used later in chapter 6 to validate the link between the selected KPI and its effect on the sensorless control performance.

4.1 Key performance Indicator

As mentioned earlier, the selected key performance indicator is primarily based on the work performed in the University of Nottingham and published in the "Power Electronics and Motion Control Conference" [16], [18]. Some definitions as well as the link between the selected KPI and its effect on the sensorless control performance will be presented in this section. The selected key performance indicator in this study is the "machine inductances". It is a good indicator as it considers the effect of the load and saturation, the influence of anisotropy determined by the rotor position and the current phase angles, and the cross-coupling between the quadrature and

direct axes [16].

4.1.1 Incremental inductance

The selected key performance indicator in this study is the "machine inductance" and specifically the "dynamic (incremental) inductance". This kind of inductance is different from the classical definition of the machine inductances which is known as the "static (apparent) inductance". It is strongly preferred in this study as it improves the accuracy of the machine model discussed in section 2.2.3 in chapter 2. This is because it considers the effect of the load and saturation, the influence of anisotropy determined by the rotor position and the current phase angles, and the cross-coupling between the quadrature and direct axes [16].

According to [25], two kinds of motor inductance are considered in the literature. These two kinds are the static (apparent) inductance (L_a) and the dynamic (incremental) inductance (L_i). The static (apparent) inductance (L_a) is the slope of the straight line from the origin through the operating point which can be seen in the magnetizing curve in Figure 4.1. This kind can be used when the transients are not so important. The static (apparent) inductance (L_a) is given by

$$L_a = \frac{\psi}{i} \tag{4.1}$$

where ψ is the flux linkage and i is the magnetizing current. While, the dynamic (incremental) inductance (L_i) is the slope of the tangent line to the magnetizing curve at the same operating point which can be seen in Figure 4.1. This kind can be used when the dynamic behavior is considered under transient conditions. It is clear that this study is more concerned with the dynamic behavior of the studied PM synchronous motor which means that the incremental inductance is preferred. The dynamic (incremental) inductance (L_i) is given by

$$L_i = \frac{d\psi}{di} \tag{4.2}$$

.

4.1.2 Evaluation of Sensorless performance

The conventional dq model of the PM synchronous machine given by (2.7) and (2.8) may result in inaccurate calculations if it is used for parameter predictions [16]. To improve its accuracy, the model can be modified to take into account the influence

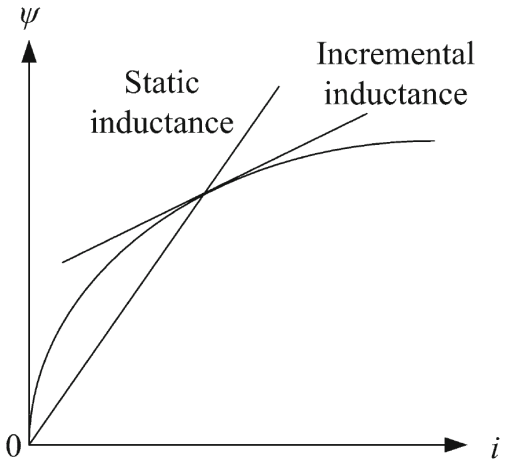

Figure 4.1:
Current – Flux linkage magnetizing curve with the static inductance and the incremental inductance.

of the self- and cross-coupling or mutual inductances between the quadrature and direct axes.

$$V_d = R_s i_d + L_{dd}\frac{di_d}{dt} + L_{dq}\frac{di_q}{dt} - L_q\frac{p}{2}\omega_r i_q \tag{4.3}$$

$$V_q = R_s i_q + L_{qq}\frac{di_q}{dt} + L_{dq}\frac{di_d}{dt} + L_d\frac{p}{2}\omega_r i_d + \lambda\frac{p}{2}\omega_r \tag{4.4}$$

where L_{dd}, L_{qq} are the direct and quadrature axis self-inductances, L_{dq}, L_{qd} are the direct and quadrature axis cross-coupling inductances, V_d, V_q are the d-q axes voltages, L_d, L_q are the d-q axes inductances, i_d, i_q are the d-q axes currents, ω_r is the rotational speed, R_s is the stator windings resistance, p is the pole-number of the machine, and λ is the amplitude of the flux induced by the permanent magnets. It is worth mentioning that the inductances L_{dd}, L_{qq}, L_{dq}, and L_{qd} are based on the "incremental inductance" concept which is discussed in section 4.1.1. From [16] and based on (4.2), L_{dd}, L_{qq}, L_{dq}, and L_{qd} are defined by

$$L_{dd} = \frac{\partial\psi_d(i_d, i_q)}{\partial i_d}, \qquad L_{qq} = \frac{\partial\psi_q(i_d, i_q)}{\partial i_q} \tag{4.5}$$

$$L_{dq} = \frac{\partial\psi_d(i_d, i_q)}{\partial i_q}, \qquad L_{qd} = \frac{\partial\psi_q(i_d, i_q)}{\partial i_d} \tag{4.6}$$

where ψ_d, and ψ_q are the d-q axes flux linkages.

Ideally, the PM synchronous machine should have a sinusoidal flux [13]. Consequently, the inductance characteristics of L_{dd}, L_{qq}, L_{dq}, and L_{qd} should be DC values which are affected by the machine loading [9]. In real-life applications, the inductance characteristics of L_{dd}, L_{qq}, L_{dq}, and L_{qd} are not DC values and they

have some space harmonics which are shown in Figure 4.10. As the rotor rotates, these space harmonics are produced in the incremental d-q inductances. They are due to the harmonics of the geometric and saturation saliency [18]. From [18] and by using Fourier analysis (found in the appendix), the harmonic analysis of the self-inductances (L_{dd}, and L_{qq}) in a PM synchronous machine results in

$$L_{dd}(\omega) = L_1\pi\delta(\omega) + \frac{L_2\pi}{2}j\delta(\omega + 6\omega_e) - \frac{L_2\pi}{2}j\delta(\omega - 6\omega_e) \tag{4.7}$$

$$L_{qq}(\omega) = 2L_S\pi\delta(\omega) - \frac{L_2\pi}{2}\delta(\omega + 6\omega_e) - \frac{L_2\pi}{2}\delta(\omega - 6\omega_e) \tag{4.8}$$

where δ is a delta function related to Fourier transformation, ω is the angular velocity, L_S is the phase stator inductance, L_1 is the saliency component, and L_2 is the more significant "unwanted" disturbance related to the phase inductance [18]. It is worth mentioning that there are other higher order harmonics but they are ignored due to their unimportant contribution as their magnitudes are small. From [18] and by using (4.7) and (4.8), it is observed that the more significant "unwanted" disturbance related to the phase inductance (L_2) is shifted in frequency and appears as a sideband component given by ($\omega \pm 6\omega_e$). This means that an unwanted disturbance will appear in the sixth harmonic component together with its multiples which is confirmed in Figures 4.11a and c. Figure 4.11 shows a Fourier analysis of the incremental inductances for the machine studied in Chapter 3 where three loading conditions are considered (no load (0 %), 30 % of the full load and full load (100 %)). Figures 4.11a and c shows the harmonic contents of the direct and quadrature axis self-inductances (L_{dd} and L_{qq}) respectively, while Figures 4.11b and d shows those of the direct and quadrature axis cross-coupling inductances (L_{dq} and L_{qd}) respectively. According to [18], the cross-coupling or mutual inductances (L_{dq}, and L_{qd}) should also have the unwanted disturbance in the sixth harmonic component together with its multiples which is conformed in Figures 4.11b and d.

As previously discussed, the incremental inductances (L_{dd}, L_{qq}, L_{dq}, and L_{qd}) are not DC values and they have some space harmonics in real-life applications. This would have a direct impact on the machine saliency which is discussed in chapter 2. Saliency is a very important characteristic in the PM synchronous machine which can be used in the estimation of the rotor position by saliency tracking [18]. Thus, any disturbance in the machine saliency will result in a bad estimation of the rotor position by that method of tracking. Also, more disturbances (more harmonic components) in the machine saliency give a worse estimation of the rotor position by saliency tracking. Consequently, the level of harmonic components in the incremental inductances (L_{dd}, L_{qq}, L_{dq}, and L_{qd}) is an indication of the quality of the rotor

position estimation by that method of tracking. In conclusion, the level of harmonic disturbance in the incremental inductances (L_{dd}, L_{qq}, L_{dq}, and L_{qd}) can be used as a key performance indicator to give a preliminary evaluation of the capability of a certain PM synchronous machine to perform sensorless vector control in a good quality using saliency tracking [18].

4.1.3 Suggested Methodology

According to [16], a proposed approach can be used to calculate the incremental inductances of a certain machine accurately based on the Finite Element Method which is discussed in chapter 3. These inductances can be calculated from the stored magnetic energy or from the flux linkages. The approach in [16] is based on the flux linkages and it will be discussed in this section.

From (4.5) and (4.6), the incremental inductances (L_{dd}, L_{qq}, L_{dq}, and L_{qd}) can be obtained by the approximation of the partial derivatives and using partial differences instead. This can be given by

$$L_{dd} = \frac{\partial \psi_d}{\partial i_d} \approx \left.\frac{\Delta \psi_d}{\Delta i_d}\right|_{\Delta i_q = 0}, \qquad L_{qq} = \frac{\partial \psi_q}{\partial i_q} \approx \left.\frac{\Delta \psi_q}{\Delta i_q}\right|_{\Delta i_d = 0} \tag{4.9}$$

$$L_{dq} = \frac{\partial \psi_d}{\partial i_q} \approx \left.\frac{\Delta \psi_d}{\Delta i_q}\right|_{\Delta i_d = 0}, \qquad L_{qd} = \frac{\partial \psi_q}{\partial i_d} \approx \left.\frac{\Delta \psi_q}{\Delta i_d}\right|_{\Delta i_q = 0} \tag{4.10}$$

where the d-q flux linkage variations ($\Delta\psi_d$ and $\Delta\psi_q$) are obtained with respect to the current variations (Δi_d and Δi_q). A FEM model of the motor under study is used to calculate these inductances. The Finite Element model of the studied PM synchronous motor is created based on the specifications of the studied motor. The Finite Element model of the studied PM synchronous motor is a "three – phase" model. In order to be able to use the equations (4.9) and (4.10), transformation between three-phase and two-phase system (using amplitude invariant transformation) as well as transformation between rotating and stationary coordinate system, and vice versa need to be implemented. Also, the loading conditions that will be considered for the studied PM synchronous motor are as follows: $I_d = 0$ and $I_q = load$. The suggested methodology shown in Figure 4.2 can be summarized in four stages (no-disturbance, disturbance in d-current, disturbance in q-current, and calculation of the incremental inductances) and it will be implemented later using a MATLAB\Simulink model, the detailed stages are as follows:

1. *No-disturbance*: In this stage, no disturbance is applied to the input current of the studied motor. Thus, the machine is loaded with the normal loading

conditions ($I_d^0 = 0$ and $I_q^0 = load$). The d-q flux linkages (ψ_d^0 and ψ_q^0) are obtained and stored. This process is repeated with several rotor positions of the studied motor and values for the whole electrical period are obtained and stored. This stage can be shown in the upper part of Figure 4.2.

2. *Disturbance in d-current*: In this stage, a disturbance (ΔI_d) is applied to the input d-current of the studied motor. Thus, the machine is loaded with the loading conditions ($I_d^d = \Delta I_d$ and $I_q^0 = load$). The d-q flux linkages (ψ_d^d and ψ_q^d) are obtained and stored. This process is repeated with several rotor positions of the studied motor and values for the whole electrical period are obtained and stored. This stage can be shown in the middle upper part of Figure 4.2.

3. *Disturbance in q-current*: In this stage, a disturbance (ΔI_q) is applied to the input q-current of the studied motor. Thus, the machine is loaded with the loading conditions ($I_d^0 = 0$ and $I_q^q = load + \Delta I_q$). The d-q flux linkages (ψ_d^q and ψ_q^q) are obtained and stored. This process is repeated with several rotor positions of the studied motor and values for the whole electrical period are obtained and stored. This stage can be shown in the middle lower part of Figure 4.2.

4. *Calculation of the incremental inductances*: In this stage, the incremental inductances (L_{dd}, L_{qq}, L_{dq}, and L_{qd}) are calculated from the differences between the disturbed and undisturbed fluxes, and the magnitude of the disturbance currents applied using (4.9) and (4.10). This stage can be shown in the lower part of Figure 4.2.

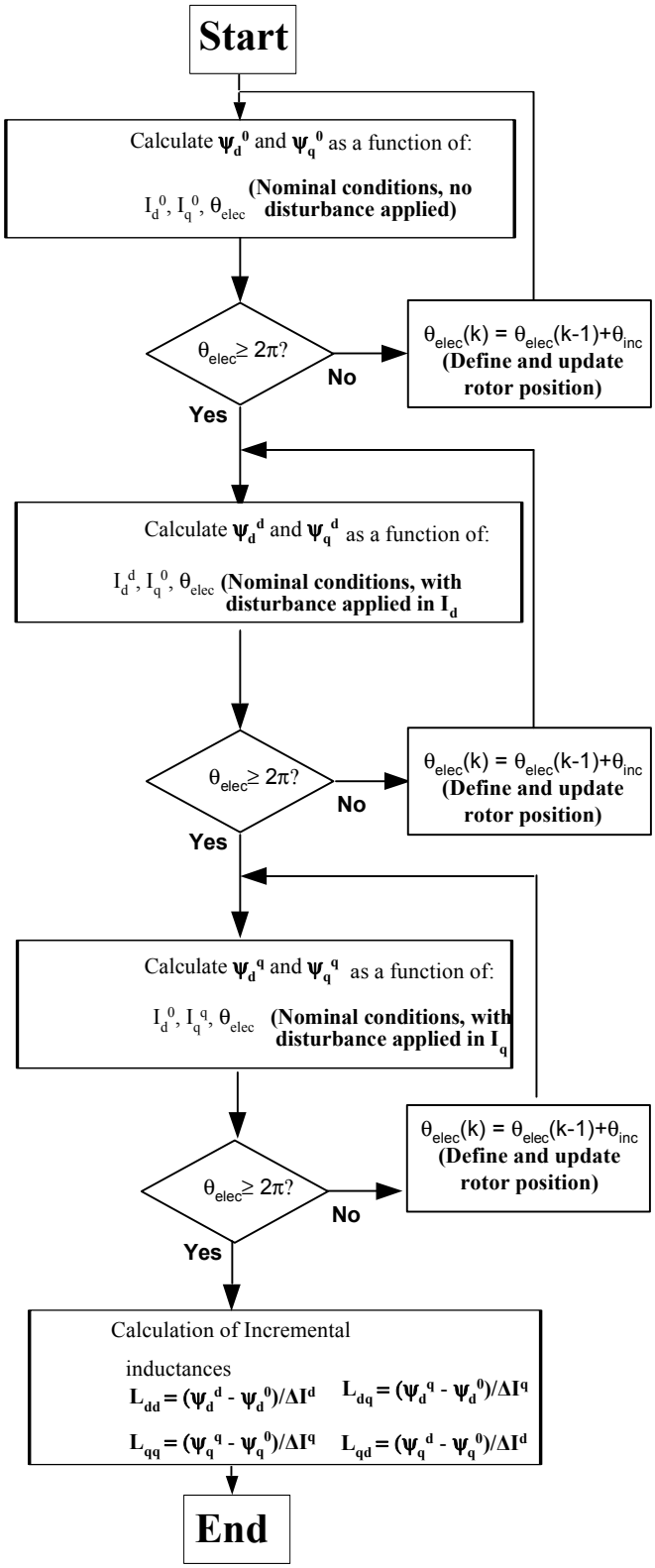

Figure 4.2:
Incremental inductances modeling flow chart [16].

It is worth mentioning that the current disturbance used in this methodology may consist of a DC value or an AC value. The advantage of using a DC value is that it reduces the computation time since a low number of iterations is required. As a general law, a DC disturbance analysis (which requires reduced computation times) can calculate the incremental inductances accurately using the proposed methodology [16]. But an AC disturbance analysis is preferred for much higher frequency ranges and when the frequency-related effects need to be analyzed in details [16].

Finally, the resulting values of the incremental inductances are plotted against the mechanical or electrical position of the rotor. Also, a Fourier analysis can be performed on the resulting incremental inductances. The harmonic content can be analyzed and used as a key performance indicator to give a preliminary evaluation of the capability of a certain PM synchronous machine to be controlled using saleincy tracking in a sensorless vector control system in a good quality as discussed earlier.

As an example for the previous discussion, the suggested methodology is applied on Bosch's machine (ECA - E). A schematic model of this machine can be shown in Figure 3.7. The machine's rated speed is 2000 *rpm* and it has 10 poles, 12 slots and 14 turns. The permanent magnets are placed on the surface of the rotor with some depth in the rotor core.

In this study, the calculated incremental inductances are obtained based on the previously discussed methodology. It is obtained for one full electrical revolution under three different loading conditions: no load (0 %), 30 % of the full load and full load (100 %). The resulting incremental inductances are plotted against the electrical position of the rotor as shown in Figure 4.10. The calculated incremental inductances for the motor at no load (0 %) is shown in Figure 4.10a, the calculated incremental inductances for the motor at 30 % of the full load is shown in Figure 4.10b, while the calculated incremental inductances for the motor at full load (100 %) is shown in Figure 4.10c.

A Fourier analysis is performed on the resulting incremental inductances for the machine studied in Chapter 3. The harmonic contents of these inducances under three different loading conditions: no load (0 %), 30 % of the full load and full load (100 %) are shown in Figure 4.11. The harmonic contents of the direct and quadrature axis self-inductances (L_{dd} and L_{qq}) are shown in Figures 4.11a and c respectively, while the harmonic contents of the direct and quadrature axis cross-coupling inductances (L_{dq} and L_{qd}) are shown in Figures 4.11b and d. Figure 4.11 shows the harmonic contents in a per unit representation respect to the offset value (the average inductance). It is worth mentioning that the Figure 4.11 agrees with what is mentioned in section 4.1.2 where the unwanted disturbances of the incremental

inductances appear in the sixth harmonic component together with its multiples.

4.2 Implementation

After the discussion of the work that is performed in the University of Nottingham and published in the "Power Electronics and Motion Control Conference" [16], [18], the implementation of the suggested methodology should be applied on the permanent magnet synchronous motor which is the main component of Bosch's engine compartment actuator (ECA - E) shown in Figure 1.1.

As mentioned in section 4.1.3, a Finite Element model of the studied PM synchronous motor needs to be created. This is done and discussed in details in chapter 3. As a result of this model, two blocks for the studied PM synchronous motor which enables power electronics circuit simulations with external programs such as Simulink are generated which are shown in Figure 3.13. According to section 3.2.3, the block "Current signal input" shown in Figure 3.13a will be used in the Simulink model used for obtaining the key performance indicators based on the suggested methodology.

The d-q currents which need to be injected to the studied PM synchronous motor will be implemented using a MATLAB\Simulink model. Also, this model will be used to perform the transformation between three-phase and two-phase system (using amplitude invariant transformation) as well as transformation between rotating and stationary coordinate system, and vice versa. Additionally, it will be used for plotting, performing Fourier analysis, and the calculation of the incremental inductances based on (4.9) and (4.10).

Finally, it is worth mentioning that the suggested methodology will be applied on the studied PM synchronous motor under three different loading conditions. The first loading condition is the full load case ($I_d = 0\ A$ and $I_q = 50\ A$) as the Phase current maximum value is 50 A according to Table 3.1. The second loading condition is 30 % of the full load case ($I_d = 0\ A$ and $I_q = 15\ A$). The third loading condition is the no load case ($I_d = 0\ A$ and $I_q = 0\ A$). Also, the current disturbance that will be applied on the d-q currents is a DC value of 0.5 A as the DC value reduces the computation time since a low number of iterations is required and it gives reliable results as discussed in section 4.1.3.

The Matlab code that is used for the suggested methodology can be seen in section A.3 in the Appendix. The first part of the code is mainly for defining some parameters that are used in the study like: the number of poles, the mechanical

speed, and the current disturbance. Then, the injected d-q currents to the studied PM synchronous motor are defined in three stages. The first one is for the "No-disturbance" stage, the second is for the "Disturbance in d-current" stage, and the third is for the "Disturbance in q-current" stage. These are the same stages that are discussed in section 4.1.3. It is worth mentioning that the code given in section A.3 in the Appendix is for the full load case. For the other cases (30 % of the full load and no load), the d-q currents need to be modified accordingly. After defining the injected d-q currents, the operating time conditions as well as the sampling frequency need to be set. The simulation is run for a period of 0.006 s which is equivalent to one electrical cycle based on a mechanical revolution speed of 2000 rpm. After that, the SIMULINK model which can be shown in Figure 4.3 is called.

This SIMULINK model helps in injecting the defined d-q currents to the motor blocks of the type shown in Figure 3.13a. There are three motor blocks, one for every current injection stage. Also, the SIMULINK model carries out the transformation between three-phase and two-phase system (using amplitude invariant transformation) as well as transformation between rotating and stationary coordinate system, and vice versa. The outputs of the three motor blocks are the three-phase flux linkages. Then back to the Matlab code, the next stage is the removal of the first point in the stored values for the currents, and flux linkages in the workspace. This is done based on the fact that all these quantities are periodic. This stage is very important as it removes the errors in calculations. After that, the incremental inductances (L_{dd}, L_{qq}, L_{dq}, and L_{qd}) are calculated based on (4.9) and (4.10). Then, the input currents as well as the output flux linkages are plotted for the sake of monitoring the system. The next stage is the Fourier analysis of the incremental inductances and then, these incremental inductances as well as their harmonic content are plotted to be used as a key performance indicator.

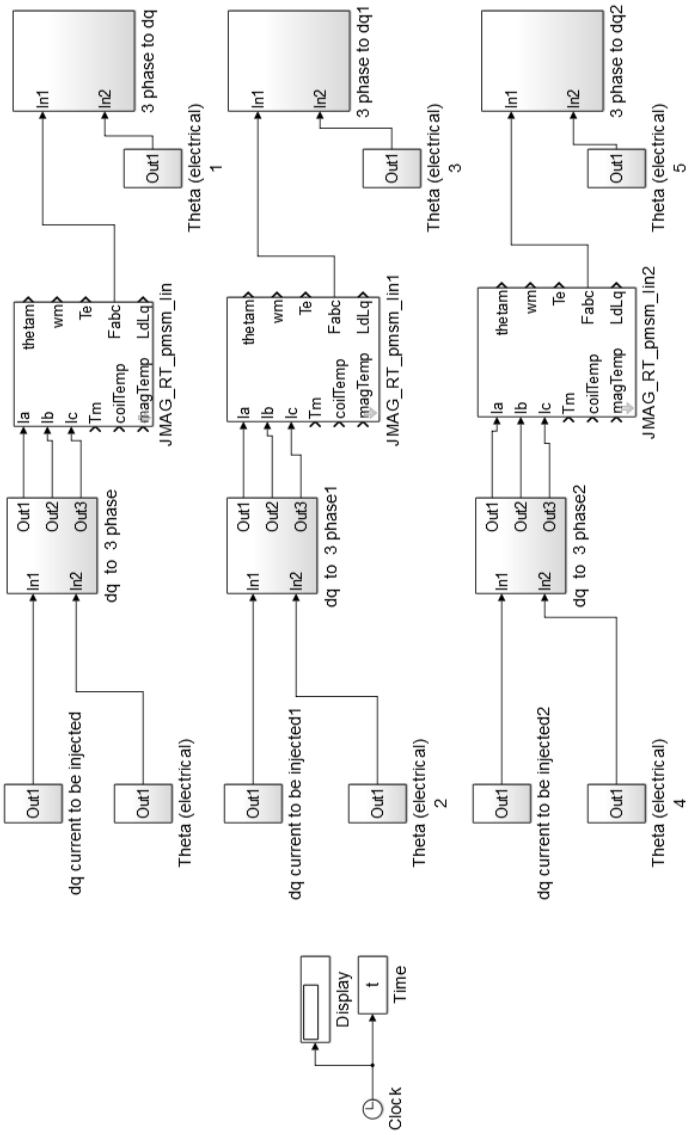

Figure 4.3:
The SIMULINK model used for the calculation of the key performance indicator including three current injection stages.

4.3 Results

As mentioned earlier, the suggested methodology is applied on the studied PM synchronous motor under three different loading conditions. The first loading condition is the full load case ($I_d = 0\ A$ and $I_q = 50\ A$). The second loading condition is 30 % of the full load case ($I_d = 0\ A$ and $I_q = 15\ A$). The third loading condition is

the no load case ($I_d = 0\ A$ and $I_q = 0\ A$). In this section, the plotted incremental inductances (L_{dd}, L_{qq}, L_{dq}, and L_{qd}) resulting from the MATLAB\Simulink model discussed in section 4.2 as well as their harmonic contents are displayed.

4.3.1 Full load case

In this case, the motor is loaded with its rated current. According to Table 3.1, the phase current maximum value of the studied PM synchronous motor is 50 A. Thus, the loading conditions for this case should be as follows: $I_d = 0\ A$ and $I_q = 50\ A$. These values are inserted in the Matlab code shown in section A.3 in the Appendix. The resulting incremental inductances (L_{dd}, L_{qq}, L_{dq}, and L_{qd}) as well as their harmonic contents are shown in Figures 4.4 and 4.5 respectively. The resulting values of the incremental inductances (L_{dd}, L_{dq}, L_{qq}, and L_{qd}) plotted against the electrical position of the rotor at full load are shown in Figures 4.4a, 4.4b, 4.4c, and 4.4d respectively. While, the resulting harmonic contents of the incremental inductances (L_{dd}, L_{dq}, L_{qq}, and L_{qd}) at full load are shown in Figures 4.5a, 4.5b, 4.5c, and 4.5d respectively.

It is worth mentioning that the incremental inductances are plotted against one electrical cycle of the rotor of the studied PM synchronous motor in Figure 4.4. Also, in Figure 4.4, it can be easily seen that the inductance characteristics of L_{dd}, L_{qq}, L_{dq}, and L_{qd} are not DC values and they have some space harmonics which agrees with what is mentioned in section 4.1.2. They are due to the harmonics of the geometric and saturation saliency [18]. Finally, all these inductances in Figure 4.4 are plotted in micro-Henry (μH).

Figure 4.5 shows the magnitude of the harmonic components of the resulting incremental inductances. These magnitudes are calculated as a per unit representation respect to the offset value (the average inductance) of each related inductance which can be seen in the Matlab code in section A.3 in the Appendix. Also, they are plotted against multiples of the frequency of the electrical period of the motor. It is worth mentioning that the Figure 4.5 agrees with what is mentioned in section 4.1.2 where the unwanted disturbances of the incremental inductances appear in the sixth harmonic component together with its multiples.

4.3.2 Thirty percent of the full load case

In this case, the motor is loaded with 30 % of its rated current (15 A). Thus, the loading conditions for this case should be as follows: $I_d = 0\ A$ and $I_q = 15\ A$. These

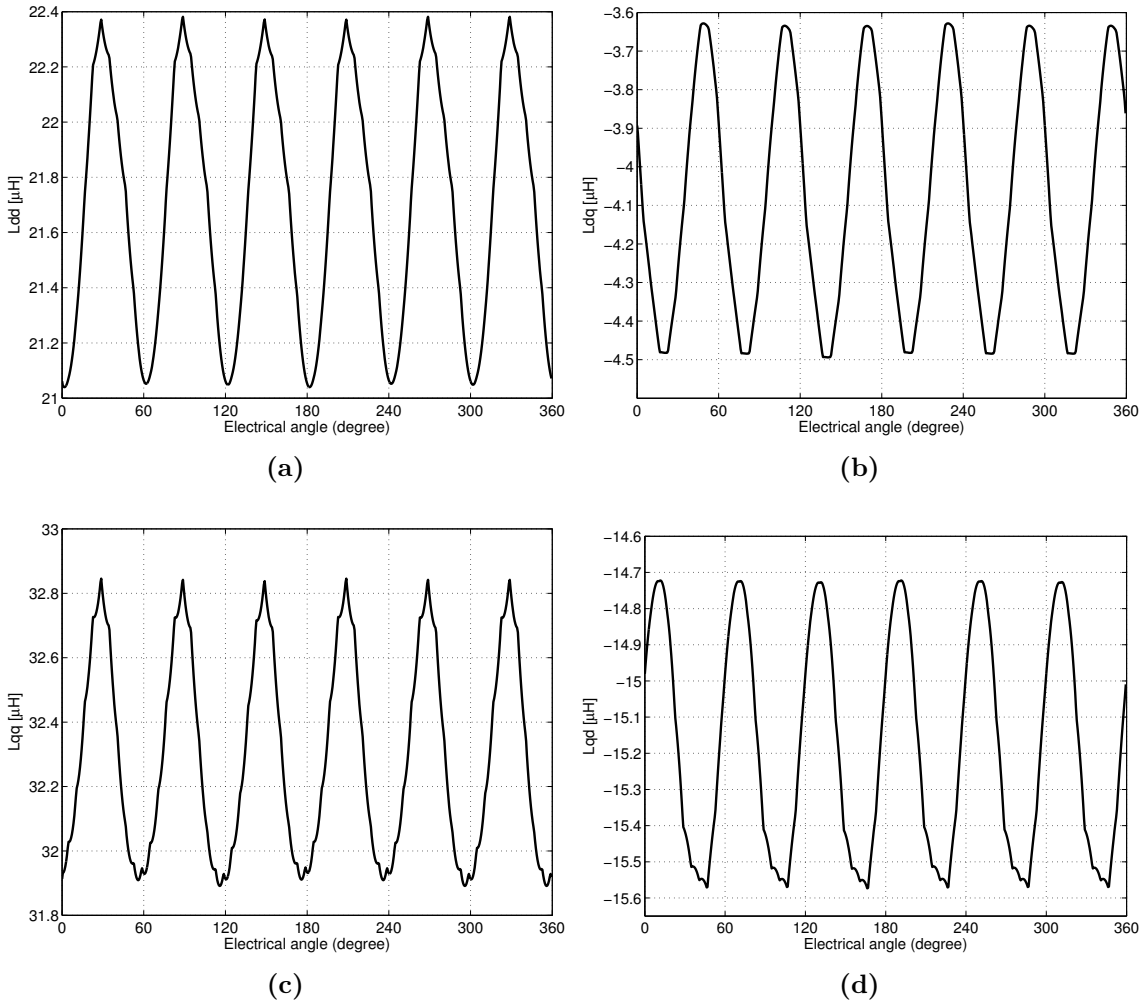

Figure 4.4:
The resulting values of the incremental inductances plotted against the electrical position of the rotor at full load: a)L_{dd} b)L_{dq} c)L_{qq} d)L_{qd}.

values are inserted in the Matlab code shown in section A.3 in the Appendix. The resulting incremental inductances (L_{dd}, L_{qq}, L_{dq}, and L_{qd}) as well as their harmonic contents are shown in Figures 4.6 and 4.7 respectively. The resulting values of the incremental inductances (L_{dd}, L_{dq}, L_{qq}, and L_{qd}) plotted against the electrical position of the rotor at 30 % of the full load are shown in Figures 4.6a, 4.6b, 4.6c, and 4.6d respectively. While, the resulting harmonic contents of the incremental inductances (L_{dd}, L_{dq}, L_{qq}, and L_{qd}) at 30 % of the full load are shown in Figures 4.7a, 4.7b, 4.7c, and 4.7d respectively.

Again, the incremental inductances are plotted against one electrical period of the rotor of the studied PM synchronous motor in Figure 4.6. Also, in Figure 4.6, it can be easily seen that the inductance characteristics of L_{dd}, L_{qq}, L_{dq}, and L_{qd} are not DC values and they have some space harmonics which agrees with what is

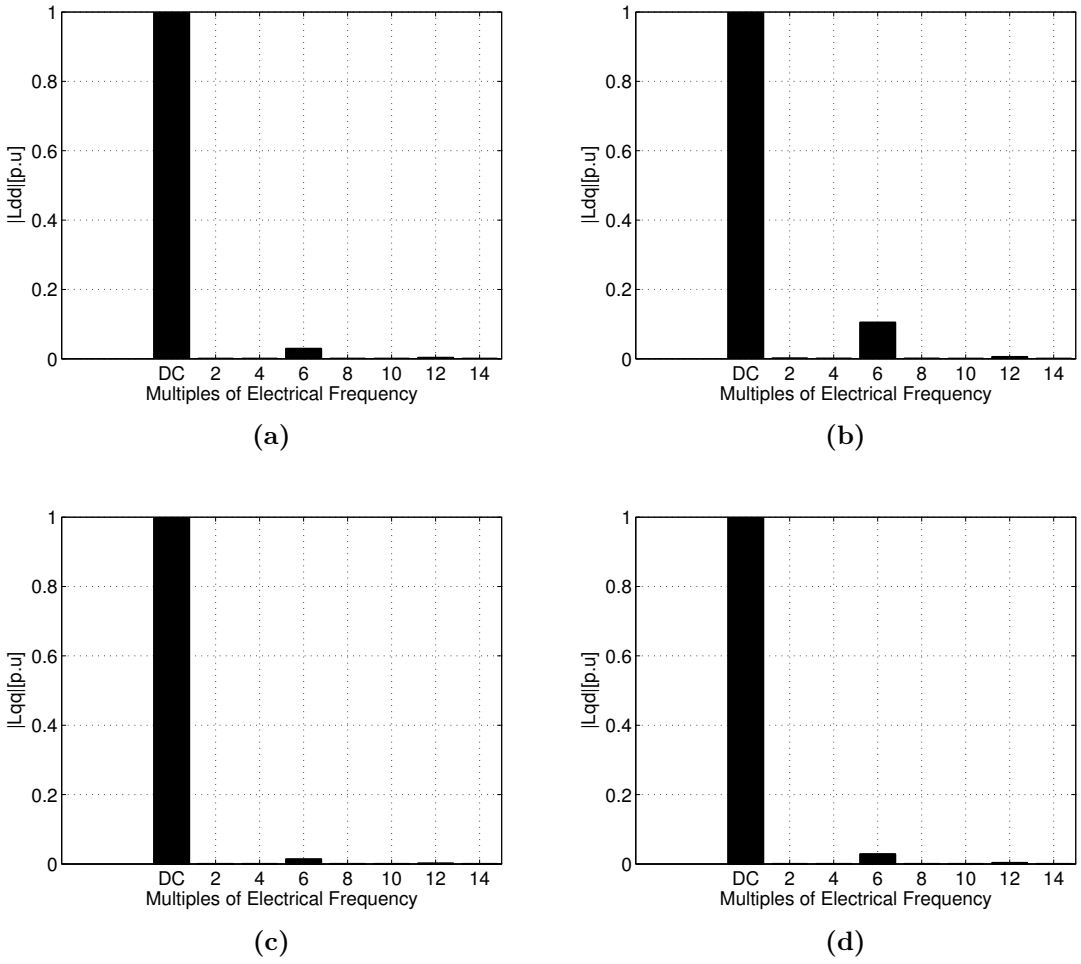

Figure 4.5:
The resulting harmonic contents of the incremental inductances at full load: a)L_{dd} b)L_{dq} c)L_{qq} d)L_{qd}.

mentioned in section 4.1.2.

Figure 4.7 shows the magnitude of the harmonic components of the resulting incremental inductances. These magnitudes are calculated as a per unit representation respect to the offset value (the average inductance) of each related inductance which can be seen in the Matlab code in section A.3 in the Appendix. Also, they are plotted against multiples of the frequency of the electrical period of the motor. Again, It is worth mentioning that the Figure 4.7 agrees with what is mentioned in section 4.1.2 where the unwanted disturbances of the incremental inductances appear in the sixth harmonic component together with its multiples.

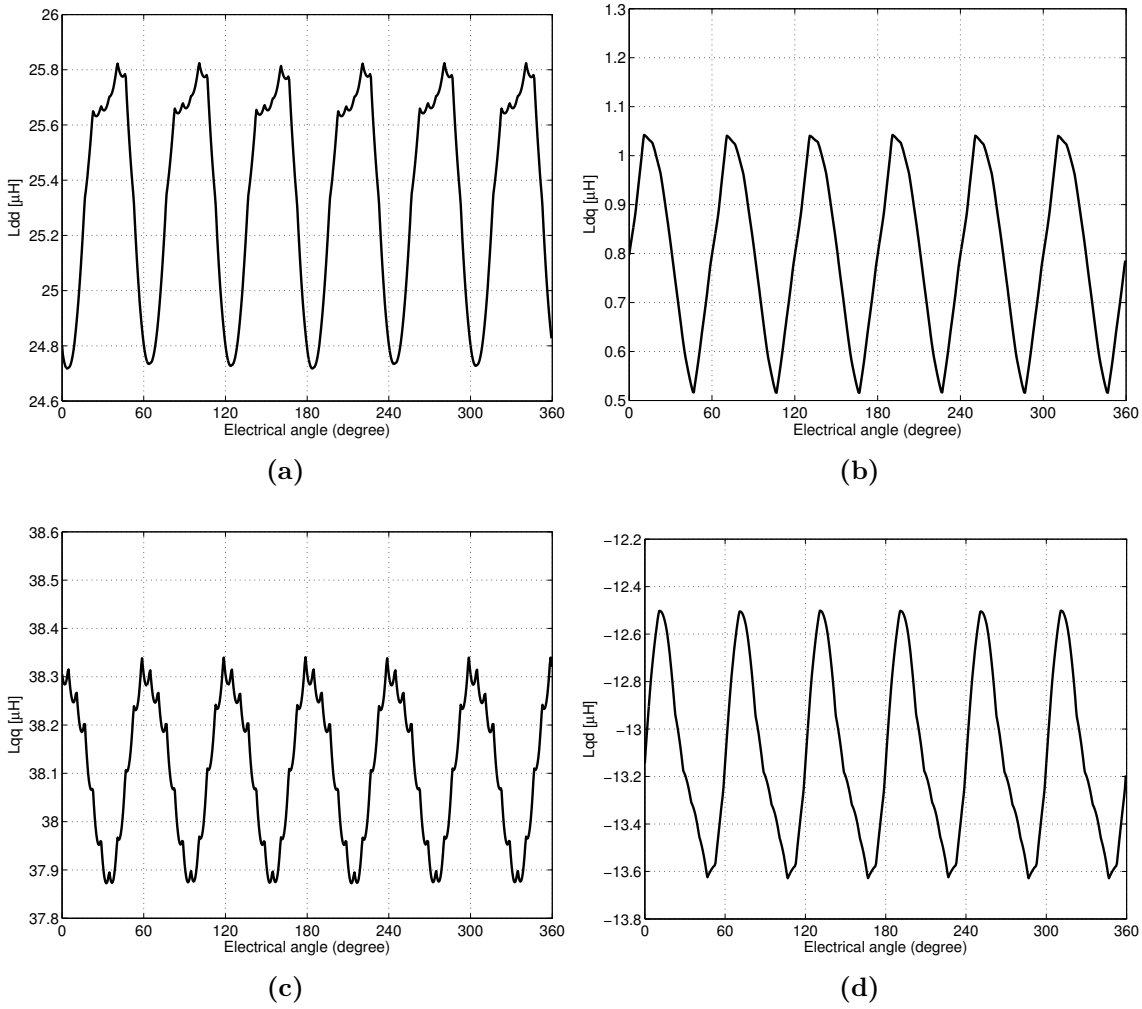

Figure 4.6:
The resulting values of the incremental inductances plotted against the electrical position of the rotor at 30 % of the full load: a)L_{dd} b)L_{dq} c)L_{qq} d)L_{qd}.

4.3.3 No load case

In this case, the motor is loaded with zero current. Thus, the loading conditions for this case should be as follows: $I_d = 0\ A$ and $I_q = 0\ A$. These values are inserted in the Matlab code shown in section A.3 in the Appendix. The resulting incremental inductances (L_{dd}, L_{qq}, L_{dq}, and L_{qd}) as well as their harmonic contents are shown in Figures 4.8 and 4.9 respectively. The resulting values of the incremental inductances (L_{dd}, L_{dq}, L_{qq}, and L_{qd}) plotted against the electrical position of the rotor at no load are shown in Figures 4.8a, 4.8b, 4.8c, and 4.8d respectively. While, the resulting harmonic contents of the incremental inductances (L_{dd}, L_{dq}, L_{qq}, and L_{qd}) at no load are shown in Figures 4.9a, 4.9b, 4.9c, and 4.9d respectively.

Again, the incremental inductances are plotted against one electrical period of

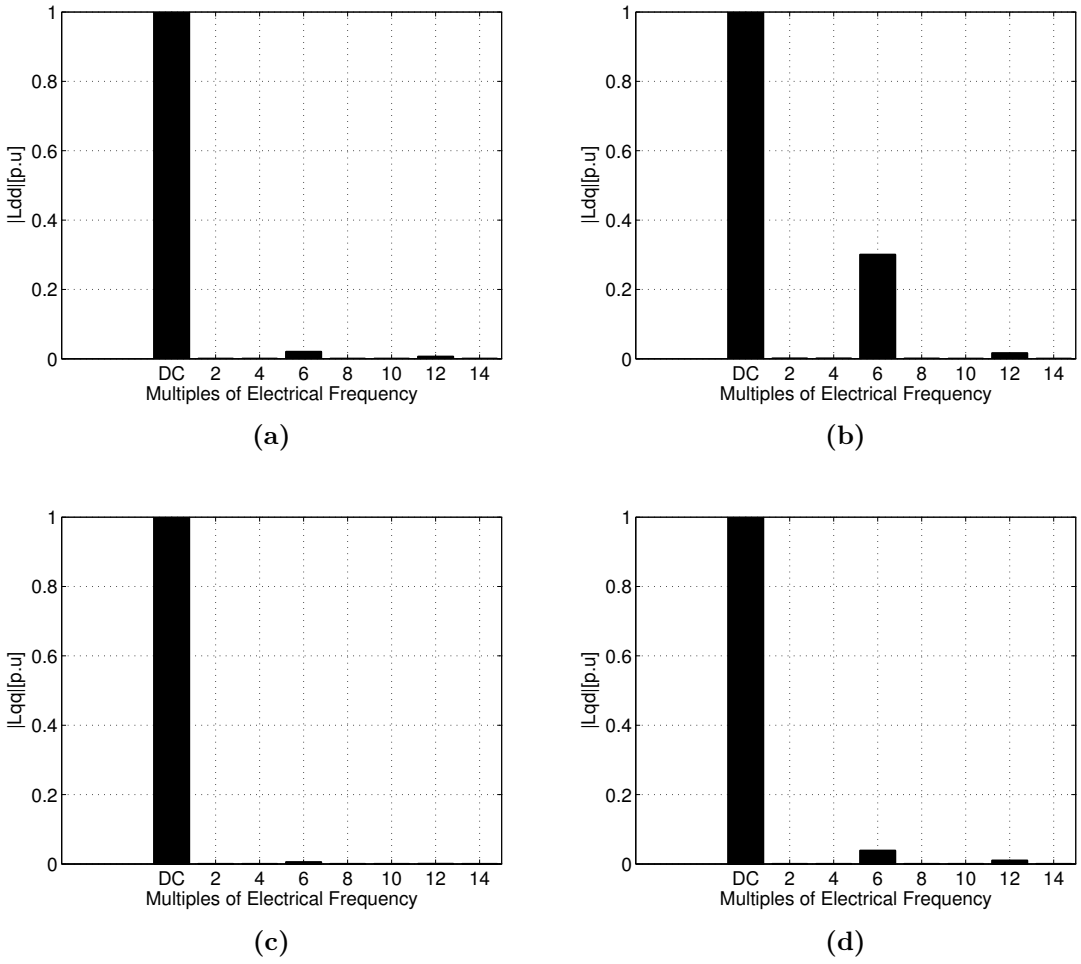

Figure 4.7:
The resulting harmonic contents of the incremental inductances at 30 % of the full load: a)L_{dd} b)L_{dq} c)L_{qq} d)L_{qd}.

the rotor of the studied PM synchronous motor in Figure 4.8. Also, in Figure 4.8, it can be easily seen that the inductance characteristics of L_{dd}, L_{qq}, L_{dq}, and L_{qd} are not DC values and they have some space harmonics which agrees with what is mentioned in section 4.1.2.

Figure 4.9 shows the magnitude of the harmonic components of the resulting incremental inductances. These magnitudes are calculated as a per unit representation respect to the offset value (the average inductance) of each related inductance which can be seen in the Matlab code in section A.3 in the Appendix. Also, they are plotted against multiples of the frequency of the electrical period of the motor. Again, it is worth mentioning that the Figure 4.9 agrees with what is mentioned in section 4.1.2 where the unwanted disturbances of the incremental inductances appear in the sixth harmonic component together with its multiples.

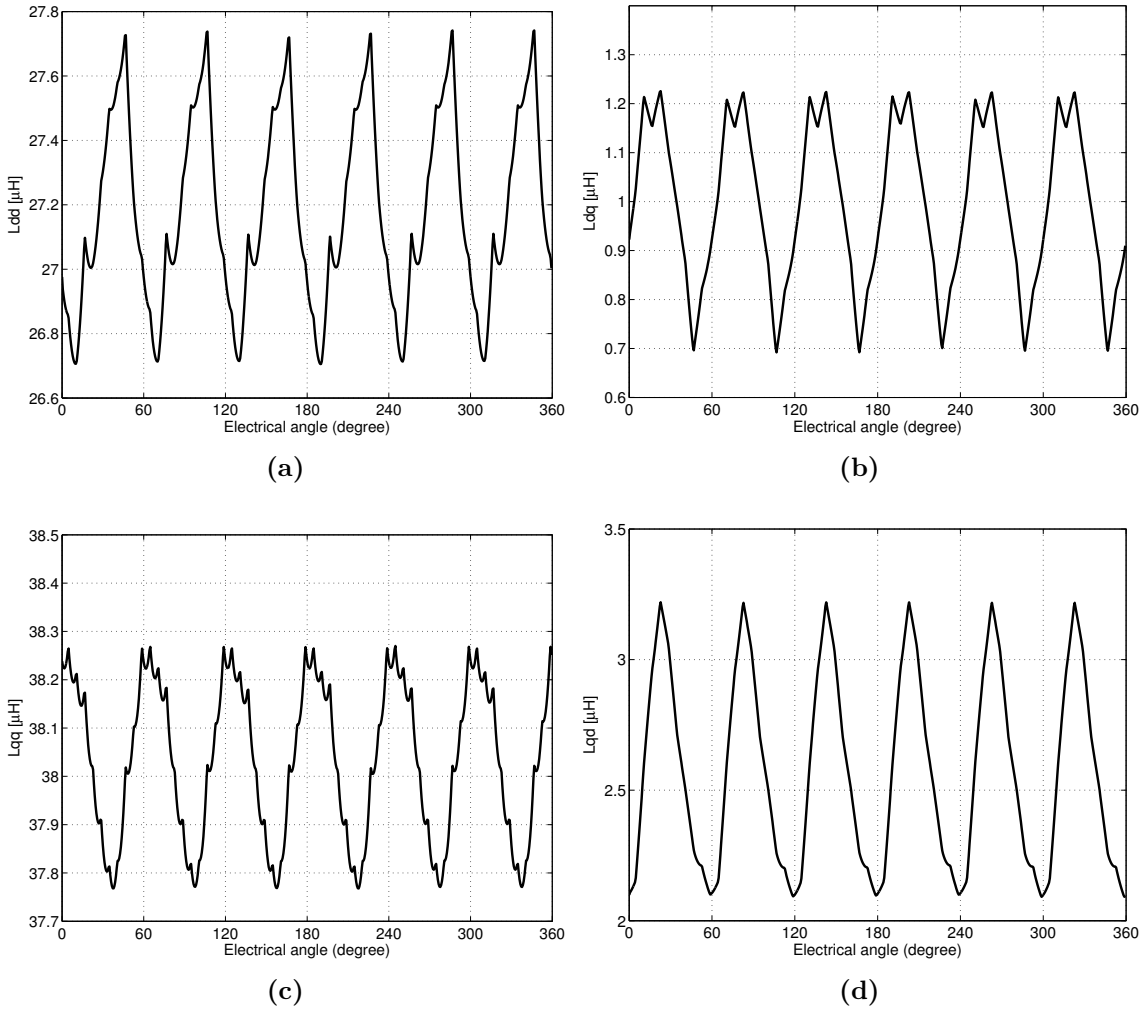

Figure 4.8:
The resulting values of the incremental inductances plotted against the electrical position of the rotor at No Load: a)L_{dd} b)L_{dq} c)L_{qq} d)L_{qd}.

4.4 Summary

In this section, the results that are discussed in section 4.3 are presented again in a more comprehensive and compact way in Figures 4.10 and 4.11. The resulting incremental inductances (L_{dd}, L_{qq}, L_{dq}, and L_{qd}) as well as their harmonic contents are shown in Figures 4.10 and 4.11 respectively. The resulting values of the incremental inductances (L_{dd}, L_{dq}, L_{qq}, and L_{qd}) plotted against the electrical position of the rotor at no load, 30 % of the full load, and full load are shown in Figures 4.10a, 4.10b, and 4.10c respectively. While, the resulting harmonic contents of the incremental inductances (L_{dd}, L_{dq}, L_{qq}, and L_{qd}) at three loads (0 %, 30 %, and 100 %) are shown in Figures 4.11a, 4.11b, 4.11c, and 4.11d respectively. It is worth

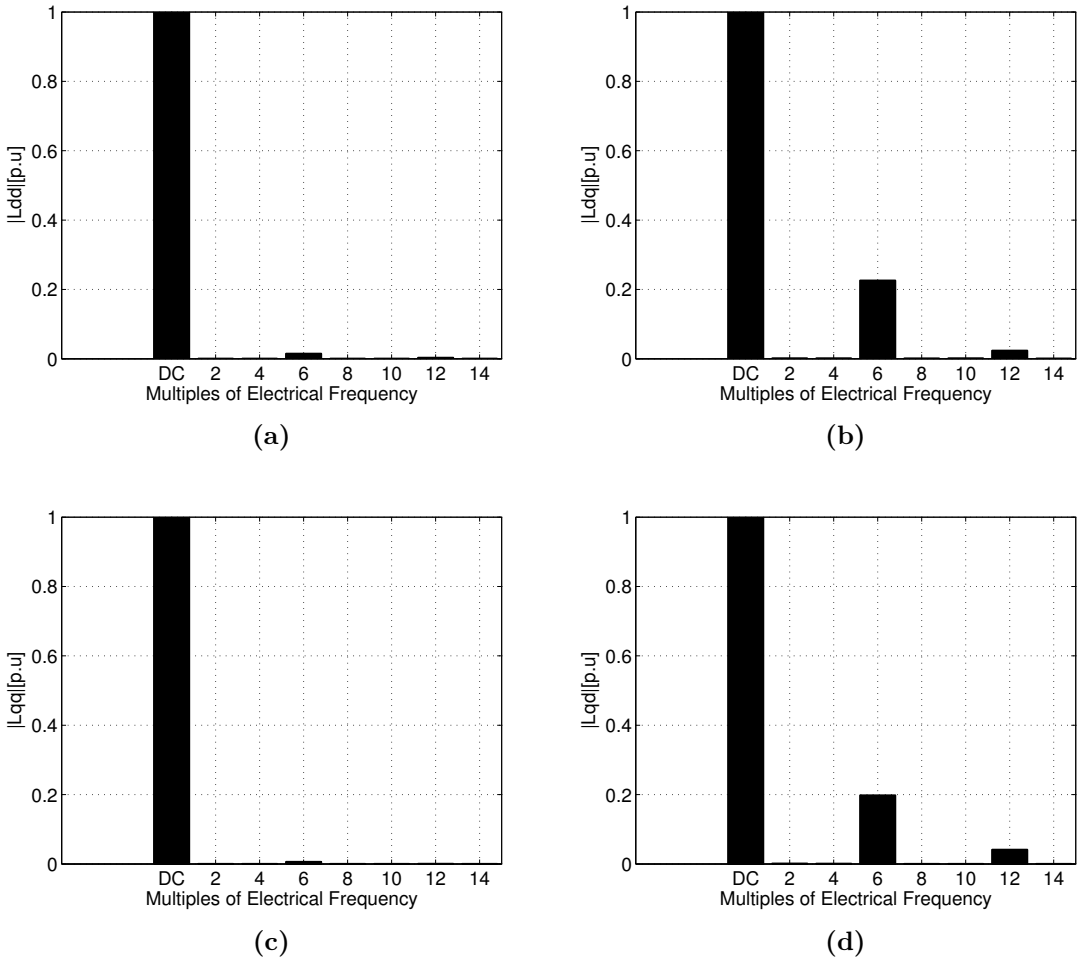

Figure 4.9:
The resulting harmonic contents of the incremental inductances at No Load: a)L_{dd} b)L_{dq} c)L_{qq} d)L_{qd}.

mentioning that Figure 4.11 shows the magnitude of the harmonic components of the resulting incremental inductances. These magnitudes are calculated as a per unit representation respect to the offset value (the average inductance) of each related inductance at full load which is different from what is done in section 4.3 . Also, they are plotted against multiples of the frequency of the electrical period of the motor. Figure 4.11 is modified such that the DC component is not shown. This modification is useful as it will make the harmonic contents appear in a more clear way. This can be seen in Figure 4.12.

Finally, some observations in Figure 4.11 are discussed. It is noticed that the resulting harmonic contents of the incremental inductances (the sixth harmonic component together with its multiples) increase with the loading in most of the cases. This may be due to the fact that the space harmonics (which are due to the

harmonics of the geometric and saturation saliency [18]) becomes more significant as the load increases. Hence, their effect becomes clearer. Additionally, the magnitude of the DC (fundamental) component of the direct axis self-inductance (L_{dd}) shown in Figure 4.11a decreases with the loading. This can be explained by the fact that the DC component is determined by the average value of L_{dd} in each loading case in Figure 4.10 calculated as a per unit representation respect to the average value of L_{dd} at full load and by looking at Figure 4.10, it is clear that the average value of L_{dd} at no load is higher than that at the 30 % of the full load, and the average value of L_{dd} at the 30 % of the full load is higher than that at full load (per unit reference value). The behavior of the magnitude of the DC components with respect to the loading for the remaining incremental inductances (L_{qq}, L_{dq}, and L_{qd}) in Figure 4.11 can be explained using the same approach.

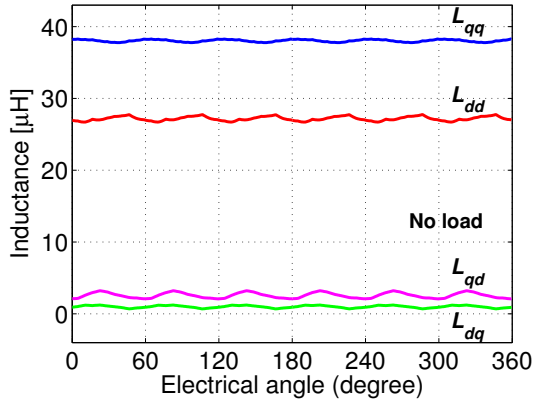

(a)

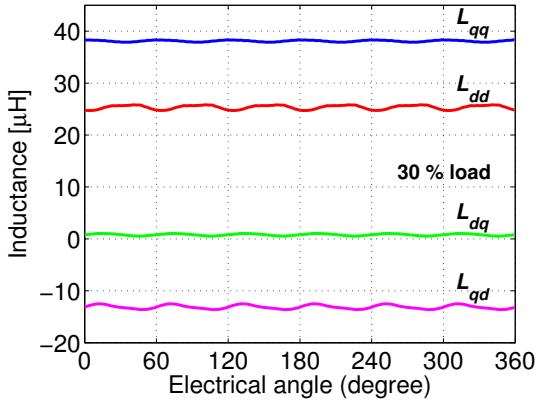

(b)

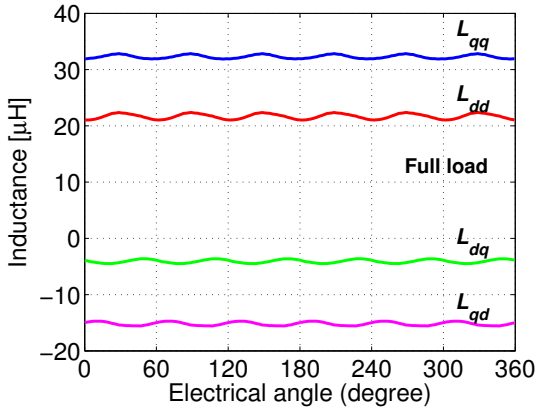

(c)

Figure 4.10:
The resulting values of the incremental inductances plotted against the electrical position of the rotor of the motor studied in chapter 3: a) No Load b) 30 % of the full load c) Full load.

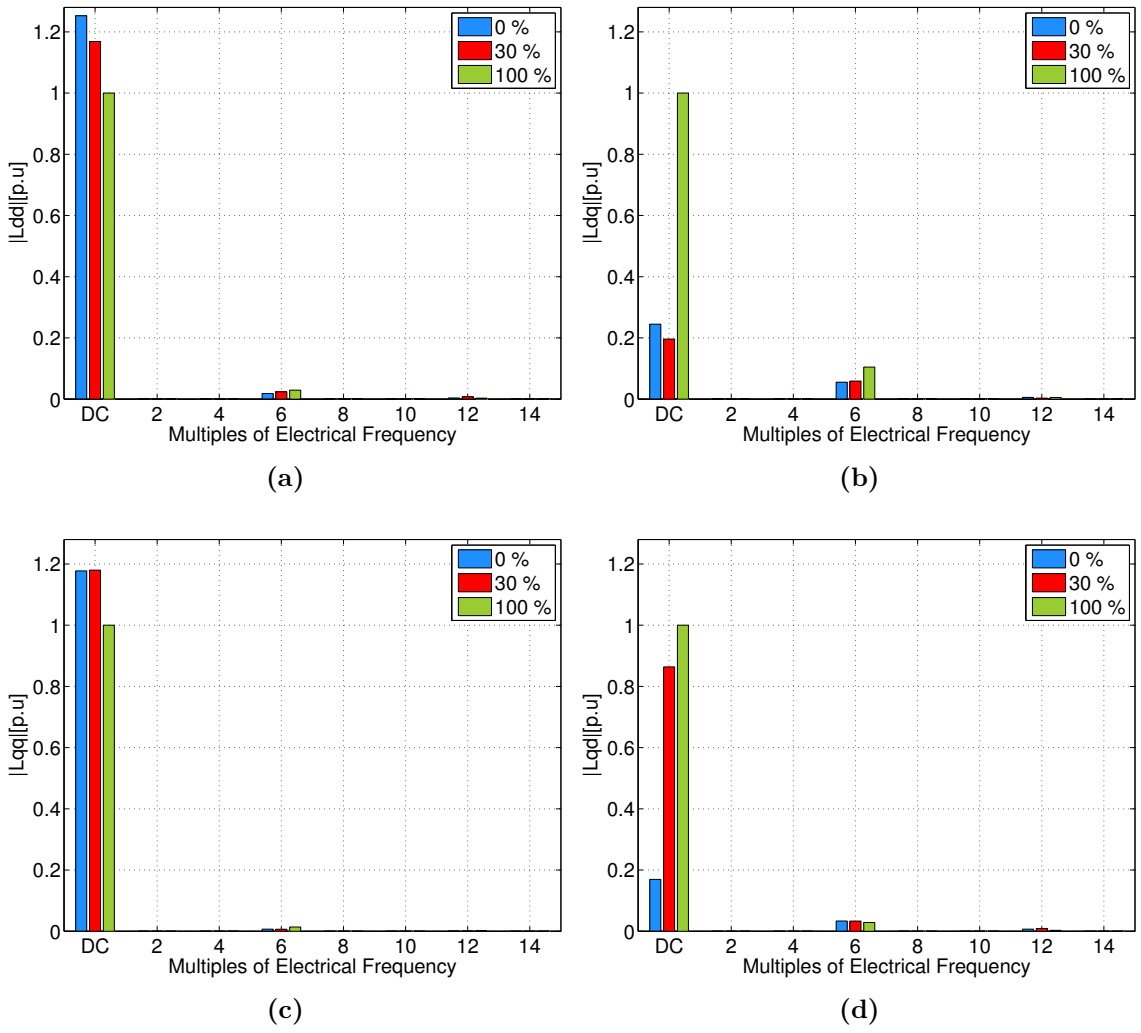

Figure 4.11:
The resulting harmonic contents of the incremental inductances for the motor studied in chapter 3 at three loads (0 %, 30 %, and 100 %): a)L_{dd} b)L_{dq} c)L_{qq} d)L_{qd}.

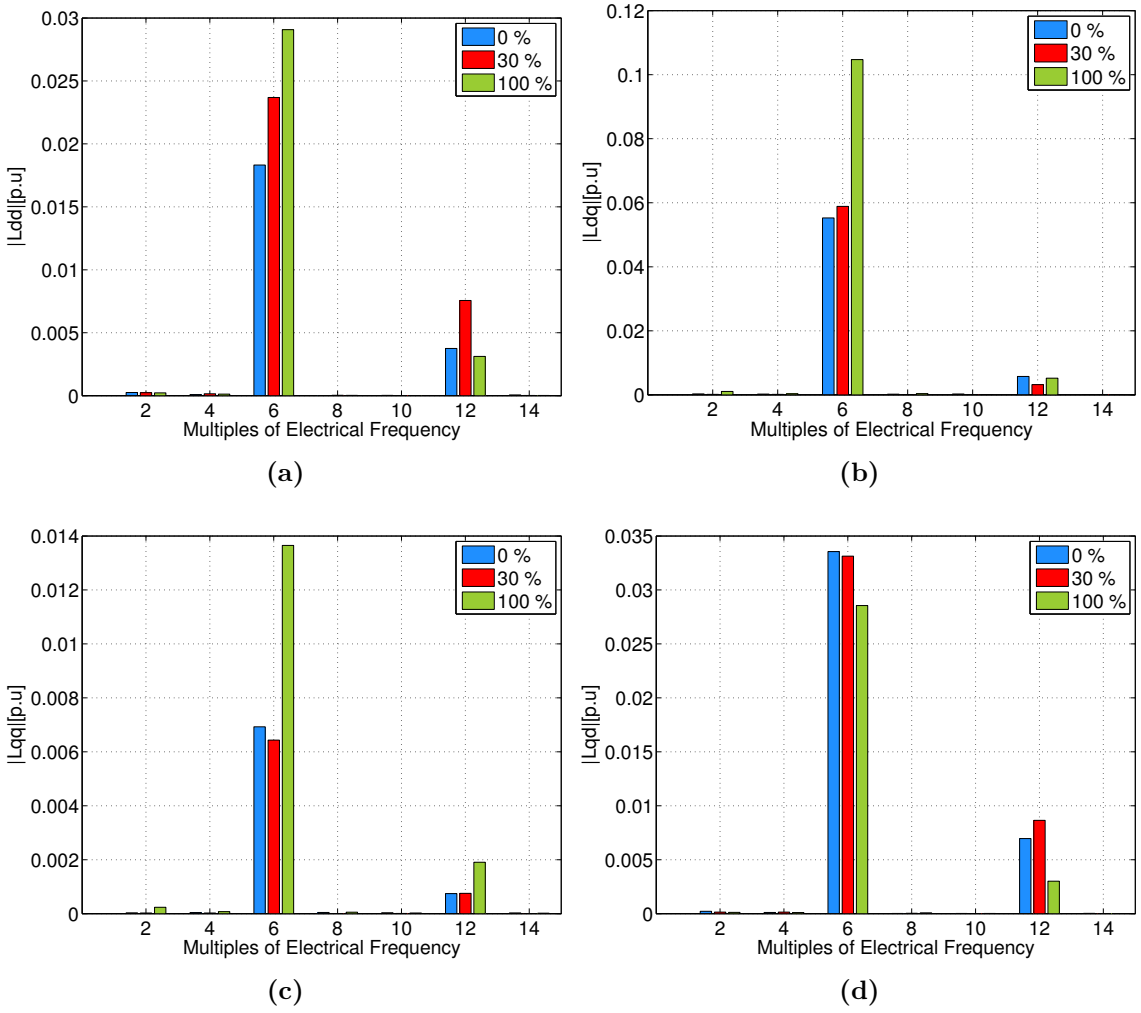

Figure 4.12:
The resulting harmonic contents of the incremental inductances for the motor studied in chapter 3 at three loads (0 %, 30 %, and 100 %): a)L_{dd} b)L_{dq} c)L_{qq} d)L_{qd} where the DC component is not shown.

5

Sensorless Performance

5.1 Introduction

As mentioned and studied in [7] and section 2.4, the field-oriented control system of a permanent magnet synchronous machine needs a position sensor which provides the angular position needed for the accurate coordinates transformation and providing the speed feedback in the controller scheme. This is the typical scheme of the field-oriented control. A certain methodology should be applied to estimate the angular position of the rotor of the studied motor (sensorless vector control) without the need to measure it. The result of this step together with the result of the methodology in chapter 4 will help in the verification of the relation between the selected key performance indicator and the sensorless control performance.

In this chapter, the position estimator is discussed. The methodology to estimate the angular position of the rotor of the studied motor is selected based on the application needs of the PM synchronous motor of Bosch's engine compartment actuator (ECA - E) shown in Figure 1.1. The selected method in this chapter is using a high frequency continuous voltage signal injection. It is mainly based on the magnetic saliency tracking of a PM synchronous machine. A certain continuous voltage signal is injected intentionally into the stator winding of the machine. This voltage signal is selected to be a pulsating signal in the estimated rotor reference frame (estimated d-q frame). The frequency of the injected signal is the same as that of the pulse-width modulation (PWM) switching. Then, the variation in the spatial inductance of the machine is obtained and the estimated angular position is calculated from it. This used methodology will be discussed in details in this chapter.

5.2 Sensorless Control

Sensorless vector control can be defined as the ability of the drive system to detect the rotor position and perform the vector control without any need for a position sensor [7].

5.2.1 Types of Sensorless Control

A lot of research and studies have been focused on improving the sensorless scheme of the controller and making it more practical. The available technologies of the sensorless position estimation can be divided into two main groups according to the estimation principle [26]. These two groups are:

1. Technologies which are based on the back electromotive force (EMF).
2. Technologies which are based on the magnetic saliency of the permanent magnet synchronous machine.

For the first group, voltage models of the controlled machine as well as observers are used. These models and observers can be in the rotating or stationary frames. They are used to estimate the rotor angular position of the motor based on the back electromotive force (EMF). The position estimation is performed in a good way using this group in the middle and high speed range of the motor. However, a bad performance is obtained at standstill as well as low speed range. This can be explained by the fact that the back electromotive force (EMF) voltage value, which is directly proportional to the rotating speed, is very small at low speeds. Therefore, the position estimation can't be performed properly based on this small value. Also, another disadvantage of this method is that it is strongly sensitive to the estimation of machine parameters, such as stator inductance and resistance [27].

For the second group, some characteristics of the studied permanent magnet synchronous machine are used to estimate the position of the rotor. These characteristics are the spatial inductances which vary with the rotor position. This is possible because of the saliency of the machine which is studied in chapter 2. By using the relationship between the current and voltage, any variation in the spatial inductances can be obtained and hence the position estimation is possible. The relationship between the current and voltage can be monitored using the pulse width modulation (PWM) current ripple [26]. Inductances calculation is performed by varying the voltage vector in a pulse width modulation period and then the related current variation is measured. There are two disadvantages of this method. Firstly, a

modification of the pulse width modulation switching pattern is required. Secondly, certain phase current measurement devices are needed in the control hardware [26].

Another method that belongs to this category is to inject a discontinuous voltage signal intentionally into the studied machine and the resulting current variation is measured. The disadvantage of this method is that a discontinuous position estimation is obtained which has a negative impact on the control performance. To avoid the disadvantage of this method, the continuous voltage signal injection methods have been developed. It is worth mentioning that these signal injection methods are better than the technologies which are based on the back electromotive force (EMF) at standstill as well as low speed range of the permanent magnet synchronous motor [27].

Another classification can be made for the methods based on signal injection. According to [26], there are two categories according to where the signal is injected. The first one is "the rotating voltage signal injection in the stationary reference frame". In this category, the continuous signal is injected regardless of the rotor position. The second one is "the pulsating voltage signal injection in the estimated rotor reference frame". As the name suggests, the continuous voltage signal is injected in a pulsating way in the estimated rotor reference frame.

Also, the signal injection methods differ according to the frequency of the injected voltage signal. It must be between the current control bandwidth and the pulse width modulation switching frequency. It is mentioned in [26] that a high frequency of the injected signal results in an enhanced sensorless control performance. Also, if the frequency of the injected signal is the same as the pulse width modulation switching frequency and if the PWM switching frequency is above the audible frequency range, the reduction or the total elimination of the accompanied acoustic noise is possible.

5.3 Proposed Sensorless technology

Based on the discussion in section 5.2.1 and the work performed in Seoul National University Power Electronics Center (SPEC) (presented in [26]), the proposed technology is selected. This new sensorless method uses a pulsating voltage signal injection in the estimated rotor reference frame. The frequency of the injected voltage signal is the same as the pulse width modulation switching frequency (16 kHz). During one PWM switching period, current is sampled twice and also the PWM signal is updated twice. As a result of this method, the decoupling of the injected signal from the fundamental frequency is easy, enhancement of the control perfor-

mance is possible, and the accompanied acoustic noise is reduced which is beneficial to Bosch's different control applications.

Let's start by the voltage equation of the permanent magnet synchronous motor in the d-q axis rotor reference frame. It is worth mentioning that this matrix form is a rearrangement of (2.7) and (2.8) which are discussed in chapter 2 where the derivative of current is expressed in discrete form as current variation ($\Delta i^r_{ds}, \Delta i^r_{qs}$) in a sampling interval (ΔT). The matrix form is given as

$$\begin{bmatrix} v^r_{ds} \\ v^r_{qs} \end{bmatrix} = R_s \begin{bmatrix} i^r_{ds} \\ i^r_{qs} \end{bmatrix} + \begin{bmatrix} L_{ds} & 0 \\ 0 & L_{qs} \end{bmatrix} \frac{1}{\Delta T} \begin{bmatrix} \Delta i^r_{ds} \\ \Delta i^r_{qs} \end{bmatrix} + \omega_r \left(\begin{bmatrix} 0 & -L_{qs} \\ L_{ds} & 0 \end{bmatrix} \begin{bmatrix} i^r_{ds} \\ i^r_{qs} \end{bmatrix} + \begin{bmatrix} 0 \\ \lambda_f \end{bmatrix} \right) \quad (5.1)$$

where $[v^r_{ds}, v^r_{qs}]^T$, and $[i^r_{ds}, i^r_{qs}]^T$ are the vectors of the stator voltage and current in the rotor reference frame, respectively, L_{ds} and L_{qs} are the d-q axis inductances, ω_r is the electrical angular speed, λ_f is the permanent-magnet flux linkage, and R_s is the stator windings resistance. Now, the proposed voltage signal injection method is used for the position estimation. A high frequency voltage signal is injected with the same frequency as the PWM switching one. This signal can be shown in Figure 5.1. From Figure 5.1, it can be seen that the square wave voltage signal is injected only in the d-axis of the estimated rotor reference frame ($v^{\hat{r}}_{dsi}$) while zero voltage is injected in the q-axis ($v^{\hat{r}}_{qsi}$). Also, it can be seen that the currents measurement occurs twice in one pulse width modulation period.

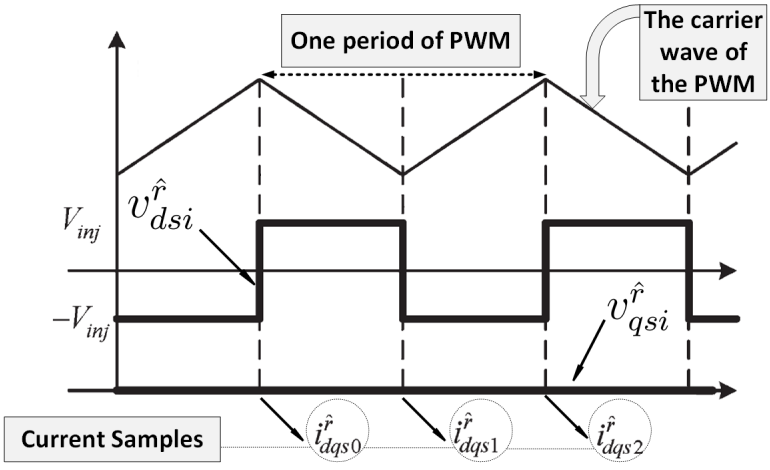

Figure 5.1:
Pulsating injection voltage signal of the proposed method in the estimated rotor reference frame where the rotor position is estimated by measuring three current values successively in one PWM period [26].

As discussed earlier in section 5.2.1, the relationship between the current and

voltage is essential in the position estimation using signal injection method. As a high frequency voltage signal is injected, the current and voltage relation at this high frequency can be obtained from (5.1) where the rotating speed of the motor is almost zero, the voltage drop of the stator resistance and the back electromotive force (EMF) voltages can be neglected. This can be shown in

$$\begin{bmatrix} v^r_{dsh} \\ v^r_{qsh} \end{bmatrix} = \begin{bmatrix} L_{ds} & 0 \\ 0 & L_{qs} \end{bmatrix} \frac{1}{\Delta T} \begin{bmatrix} \Delta i^r_{dsh} \\ \Delta i^r_{qsh} \end{bmatrix} \tag{5.2}$$

where $[v^r_{dsh}, v^r_{qsh}]^T$, and $[i^r_{dsh}, i^r_{qsh}]^T$ are the vectors of the injection frequency voltage component and current component in the rotor reference frame, respectively. The high frequency voltage signal which can be seen in Figure 5.1 is injected in the estimated rotor reference frame as mentioned earlier. The exact position of the real rotor reference frame is not available. There is a position error ($\tilde{\theta}_r$) between the real and the estimated rotor reference frames which can be seen in Figure 5.2. This means that there is also a position error in the injection voltage signal in the real rotor reference frame. The relationship between the injection voltage signal in the real rotor reference frame (V^r_{dqsh}) and the injection voltage signal in the estimated rotor reference frame ($V^{\hat{r}}_{dqsh}$) can be given by

$$V^r_{dqsh} = T(\tilde{\theta}_r) V^{\hat{r}}_{dqsh} = \pm\, V_{inj} \begin{bmatrix} \cos\tilde{\theta}_r \\ -\sin\tilde{\theta}_r \end{bmatrix} \tag{5.3}$$

where $T(\tilde{\theta}_r)$ is the transformation from the estimated rotor reference frame to the real rotor reference frame, and V_{inj} is the amplitude of the injection signal.

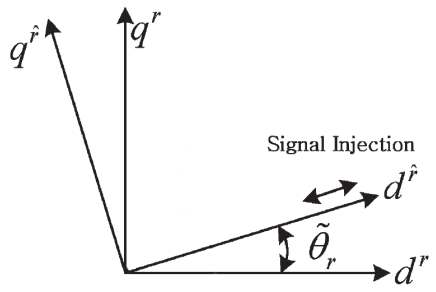

Figure 5.2:
Real axis, and estimated axis in the rotor reference frame with the position error ($\tilde{\theta}_r$) between the real and the estimated rotor reference frames [26].

From (5.2) and (5.3), the current ripple ($[\Delta i^r_{dsh}, \Delta i^r_{qsh}]^T$) can be calculated as

$$\begin{bmatrix}\Delta i^r_{dsh}\\ \Delta i^r_{qsh}\end{bmatrix} = \pm\ \Delta T\ V_{inj}\begin{bmatrix}\frac{1}{L_{ds}}\cos\tilde{\theta}_r\\ \frac{-1}{L_{qs}}\sin\tilde{\theta}_r\end{bmatrix} \tag{5.4}$$

and again, the current measurement can only be obtained in the estimated rotor reference frame. Therefore, the current ripple in the estimated rotor reference frame ($[\Delta i^{\hat{r}}_{dsh}, \Delta i^{\hat{r}}_{qsh}]^T$) can be given as

$$\begin{bmatrix}\Delta i^{\hat{r}}_{dsh}\\ \Delta i^{\hat{r}}_{qsh}\end{bmatrix} = T(\tilde{\theta}_r)^{-1}\begin{bmatrix}\Delta i^r_{dsh}\\ \Delta i^r_{qsh}\end{bmatrix} = \pm\ \Delta T\ V_{inj}\begin{bmatrix}\frac{\cos^2\tilde{\theta}_r}{L_{ds}} + \frac{\sin^2\tilde{\theta}_r}{L_{qs}}\\ \frac{1}{2}\ (\frac{1}{L_{ds}} - \frac{1}{L_{qs}})\sin 2\tilde{\theta}_r\end{bmatrix}. \tag{5.5}$$

As seen from (5.5), the information about the error in the rotor position depends on the q-axis current ripple in the estimated rotor reference frame ($\Delta i^{\hat{r}}_{qsh}$). Thus, it is possible to use the q-axis current ripple in the estimated rotor reference frame as the position error in the sensorless control technique.

Now, the current ripple caused by the injected voltage signal will be calculated. The dq-axis voltage reference from the current control loop consists of two voltages. These voltages are the d-axis voltage reference and the q-axis voltage reference. The d-axis voltage reference is given by

$$v^{\hat{r}}_{ds} = v^{\hat{r}}_{dsf} + v^{\hat{r}}_{dsc} = R_s i^{\hat{r}}_{ds} - \omega_r L_{qs} i^{\hat{r}}_{qs} + L_{ds}\frac{di^{\hat{r}}_{ds}}{dt} \tag{5.6}$$

where the d-axis voltage reference ($v^{\hat{r}}_{ds}$) is composed of two components which are the fundamental d-axis voltage ($v^{\hat{r}}_{dsf}$) and the current control d-axis voltage ($v^{\hat{r}}_{dsc}$). These two components are given by

$$v^{\hat{r}}_{dsf} = R_s i^{\hat{r}}_{ds} - \omega_r L_{qs} i^{\hat{r}}_{qs} \tag{5.7}$$

$$v^{\hat{r}}_{dsc} = L_{ds}\frac{di^{\hat{r}}_{ds}}{dt} \tag{5.8}$$

where the fundamental d-axis voltage ($v^{\hat{r}}_{dsf}$) is composed mainly of the voltage drop of the stator resistance (integral part of the PI controller) and the back electromotive force (EMF) (feed-forward term) voltages, while the current control d-axis voltage ($v^{\hat{r}}_{dsc}$) is the portion which causes the current variation in the voltage reference of the current control loop (proportional part of the PI controller). Similarily, the q-axis voltage reference is given by

$$v^{\hat{r}}_{qs} = v^{\hat{r}}_{qsf} + v^{\hat{r}}_{qsc} = R_s i^{\hat{r}}_{qs} + \omega_r L_{ds} i^{\hat{r}}_{ds} + \omega_r \lambda_f + L_{qs}\frac{di^{\hat{r}}_{qs}}{dt} \tag{5.9}$$

where the q-axis voltage reference ($v^{\hat{r}}_{qs}$) is composed of two components which are

the fundamental q-axis voltage ($v^{\hat{r}}_{qsf}$) and the current control q-axis voltage ($v^{\hat{r}}_{qsc}$). These two components are given by

$$v^{\hat{r}}_{qsf} = R_s i^{\hat{r}}_{qs} + \omega_r L_{ds} i^{\hat{r}}_{ds} + \omega_r \lambda_f \tag{5.10}$$

$$v^{\hat{r}}_{qsc} = L_{qs} \frac{d i^{\hat{r}}_{qs}}{dt} \tag{5.11}$$

where the fundamental q-axis voltage ($v^{\hat{r}}_{dsf}$) is composed mainly of the voltage drop of the stator resistance and the back electromotive force (EMF) voltages, while the current control q-axis voltage ($v^{\hat{r}}_{qsc}$) is the portion which causes the current variation in the voltage reference of the current control loop.

Now, when the discussed voltages are added together with the injected voltage signal, the corresponding current ripple is the resultant of two voltages which are: the current control voltage and the injection voltage. To be able to estimate the rotor position correctly, the current ripple due to the injected voltage signal must be separated from the total current ripple and analyzed. The voltage references as well as the corresponding current ripple can be shown in Figure 5.3.

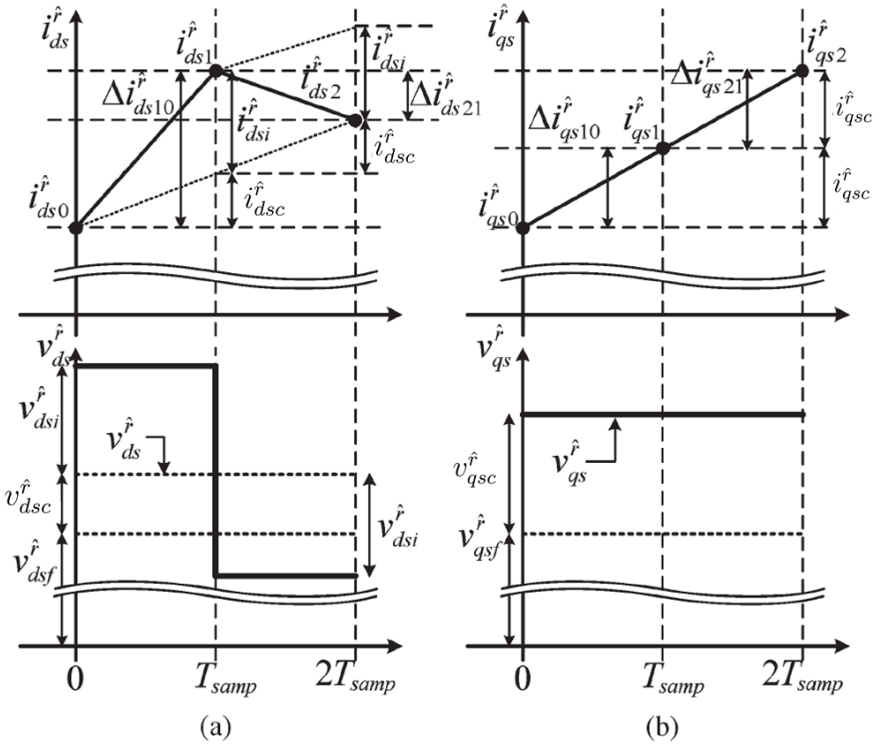

Figure 5.3:
Estimated rotor reference frame voltage signal injection. (a) d-axis voltage reference and injected signal in a PWM period and the corresponding current response. (b) q-axis voltage reference and the corresponding current response [26].

As seen in Figure 5.3, the dq-axis current ripples in the estimated rotor reference frame due to the current control voltage ($v^{\hat{r}}_{dsc}$, $v^{\hat{r}}_{qsc}$) in one pulse width modulation period are $2i^{\hat{r}}_{dsc}$ and $2i^{\hat{r}}_{qsc}$, respectively. While, the ones due to the injected voltage signal are $i^{\hat{r}}_{dsi}$ and $i^{\hat{r}}_{qsi}$. By referring to Figure 5.1, three successive current samples are needed to obtain the current ripple due to only the injected signal. The current ripple in the first half of the PWM period ($\Delta i^{\hat{r}}_{dqs10}$) is composed of two components: the fundamental current ripple ($i^{\hat{r}}_{dqsc}$) and the injection signal current ripple ($i^{\hat{r}}_{dqsi}$). This can be shown in

$$\Delta i^{\hat{r}}_{ds10} = i^{\hat{r}}_{ds1} - i^{\hat{r}}_{ds0} = i^{\hat{r}}_{dsc} + i^{\hat{r}}_{dsi} \tag{5.12}$$

$$\Delta i^{\hat{r}}_{qs10} = i^{\hat{r}}_{qs1} - i^{\hat{r}}_{qs0} = i^{\hat{r}}_{qsc} + i^{\hat{r}}_{qsi} \tag{5.13}$$

where the currents $i^{\hat{r}}_{ds1}$, $i^{\hat{r}}_{ds0}$, $i^{\hat{r}}_{qs1}$, and $i^{\hat{r}}_{qs0}$ can be seen in Figure 5.3.

Similarly, the current ripple in the second half of the PWM period ($\Delta i^{\hat{r}}_{dqs21}$) is composed of the substraction of two components: the fundamental current ripple ($i^{\hat{r}}_{dqsc}$) and the injection signal current ripple ($i^{\hat{r}}_{dqsi}$). This can be shown in

$$\Delta i^{\hat{r}}_{ds21} = i^{\hat{r}}_{ds2} - i^{\hat{r}}_{ds1} = i^{\hat{r}}_{dsc} - i^{\hat{r}}_{dsi} \tag{5.14}$$

$$\Delta i^{\hat{r}}_{qs21} = i^{\hat{r}}_{qs2} - i^{\hat{r}}_{qs1} = i^{\hat{r}}_{qsc} - i^{\hat{r}}_{qsi} \tag{5.15}$$

where the currents $i^{\hat{r}}_{ds2}$, $i^{\hat{r}}_{ds1}$, $i^{\hat{r}}_{qs2}$, and $i^{\hat{r}}_{qs1}$ can be seen in Figure 5.3.

By subtracting (5.14) from (5.12) and (5.15) from (5.13), the current ripple due to only the injected signal can be obtained. This can be shown by

$$\Delta i^{\hat{r}}_{ds10} - \Delta i^{\hat{r}}_{ds21} = 2i^{\hat{r}}_{dsi} \tag{5.16}$$

$$\Delta i^{\hat{r}}_{qs10} - \Delta i^{\hat{r}}_{qs21} = 2i^{\hat{r}}_{qsi} \ . \tag{5.17}$$

From (5.5), (5.16), and (5.17), the calculated current ripple can be obtained as a function of the position error. This is given by

$$\begin{bmatrix} i^{\hat{r}}_{dsi} \\ i^{\hat{r}}_{qsi} \end{bmatrix} = \begin{bmatrix} \Delta i^{\hat{r}}_{ds10} - \Delta i^{\hat{r}}_{ds21} \\ \Delta i^{\hat{r}}_{qs10} - \Delta i^{\hat{r}}_{qs21} \end{bmatrix} = 2\Delta T \ V_{inj} \begin{bmatrix} \frac{\cos^2\tilde{\theta}_r}{L_{ds}} + \frac{\sin^2\tilde{\theta}_r}{L_{qs}} \\ \frac{1}{2}\ (\frac{1}{L_{ds}} - \frac{1}{L_{qs}}) \sin 2\tilde{\theta}_r \end{bmatrix}. \tag{5.18}$$

From (5.18), it can be easily seen that the position error ($\tilde{\theta}_r$) is directly proportional to the difference between two q-axis current ripples in the estimated rotor reference frame with a constant of proportionality (K) where $\sin 2\tilde{\theta}_r \approx 2\tilde{\theta}_r$ where $\tilde{\theta}_r$ is small and in radians. The position error ($\tilde{\theta}_r$) as well as the constant of propor-

tionality (K) can be given by

$$\tilde{\theta}_r = K i^{\hat{r}}_{qsi} = K(\Delta i^{\hat{r}}_{qs10} - \Delta i^{\hat{r}}_{qs21}) \tag{5.19}$$

$$K = \frac{L_{ds} L_{qs}}{2(L_{qs} - L_{ds})\Delta T \; V_{inj}} \tag{5.20}$$

where L_{ds} and L_{qs} are assumed to be constant and finally, the block diagram for the rotor position estimation in the proposed methodology can be shown in Figure 5.4 where the position error ($\tilde{\theta}_r$) can be used as a corrective error input to the

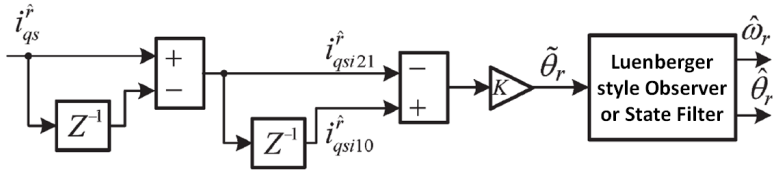

Figure 5.4:
Proposed demodulation process with high-frequency signal injectionin the estimated rotor reference frame [26].

Luenberger style observer [26] or state filter to obtain the estimated rotor position ($\hat{\theta}_r$) and the estimated speed ($\hat{\omega}_r$) [26].

5.4 Implementation

The simulated model of the position estimator that is used in the verification of the key performance indicator (KPI) in chapter 6 is based on one of Bosch's position estimators which are used in real-life applications. It uses the theory discussed in section 5.3. The simulation is performed in SIMULINK using the JMAG-RT motor block that is created from the motor simulation in chapter 3. The model uses some additional libraries like: PLECS Blockset, and Model-based System Engineering (MSE) which is a Bosch-owned library.

The model is customized so that it can be suitable for the permanent magnet synchronous motor (PMSM) of Bosch's engine compartment actuator (ECA - E) which is simulated in chapter 3. The motor parameters like: the number of poles, the stator phase resistance, d-q axis inductances, and the maximum value of the stator winding flux linkage are inserted which can be seen in Table 5.1. During the simulation, the motor is provided with the desired mechanical speed/angle profile. Then, the motor is injected with the high frequency voltage signal and the stator current is measured. The injection current response is extracted to obtain the position estimation information exactly as discussed in section 5.3.

Table 5.1: Values inserted and modified in Bosch's simulated model of the position estimator.

Parameter	Unit	Value
PWM frequency	kHz	18
Injected voltage frequency	kHz	18
Injected voltage amplitude	V	4
Inverter supply voltage	V	12
Number of motor pole pairs		5
Stator phase resistance	$m\Omega$	28.72
Direct-axis inductance (L_d)	μH	27.18
Quadrature-axis inductance (L_q)	μH	38.03
Stator winding peak flux linkage	mVs	2.267

The block diagram of the simulated position estimator is shown in Figure 5.5. As can be seen in the figure, it is composed of seven blocks. Each block represents a certain stage of the position estimation process. The components of the block diagram are as follows:

1. *Current values storage*: In block A, the three successive values of the sampled current in one PWM period are stored.

2. *Position error calculation*: In block B, the stored current values are used to calculate the position error with (5.19) and (5.20).

3. *Luenberger style observer*: In this block C, the estimated position is calculated from the position error obtained in the previous block by using a Luenberger style observer.

4. *Voltage signal injection*: In block D, the high frequency voltage signal which is needed for position estimation is injected.

5. *Duty cycle implementation*: In block E, the duty cycle is implemented to be used in the pulse width modulation technique.

6. *Pulse width modulation creation*: In block F, the pulse width modulation signal is created to supply the inverter.

7. *Inverter and PMSM*: In block G, both the inverter and the controlled permanent magnet synchronous motor are located. Also, the desired mechanical speed/angle profile is supplied to the motor.

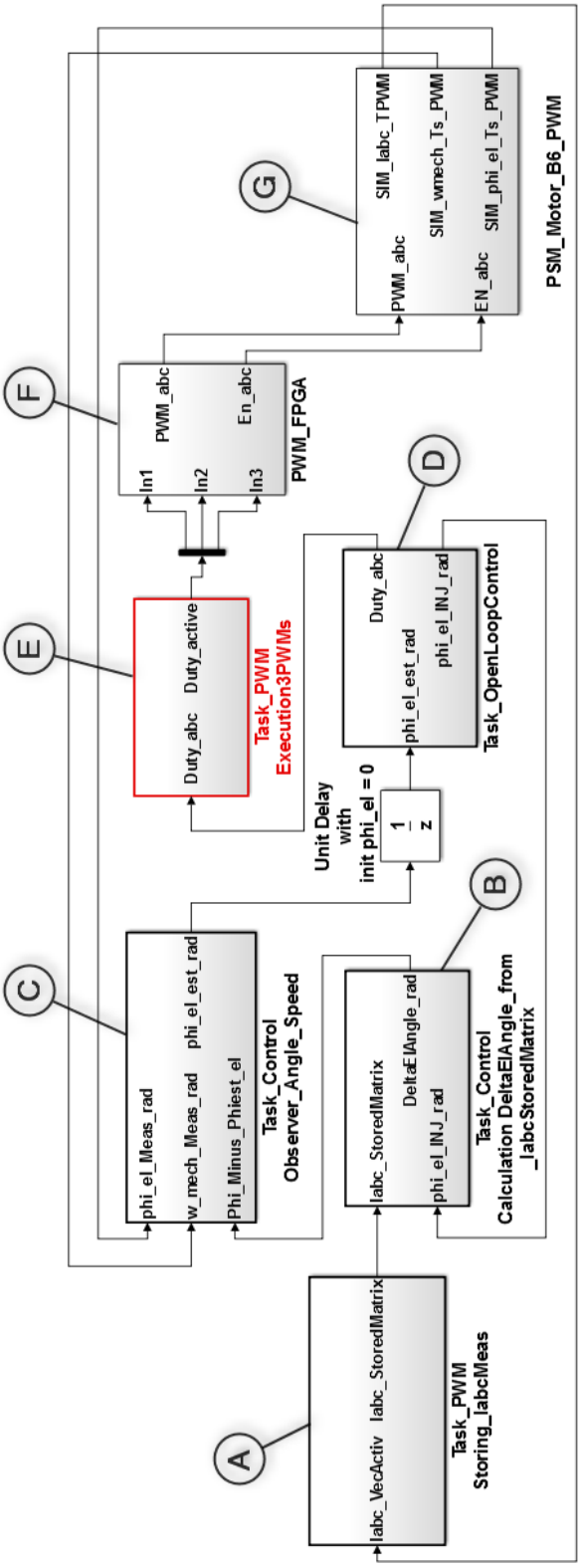

Figure 5.5:
The Block diagram of the simulated model of Bosch's position estimator: A) Current values storage B) Position error calculation C) Luenberger style observer D) Voltage signal injection E) Duty cycle implementation F) Pulse width modulation creation G) Inverter and PMSM.

5.5 Performance of the sensorless observer for the base machine

Two simulations are performed, one with an ideal machine and one with the JMAG machine model. With the ideal machine means a machine which is not based on the FEM simulation and consequently, it doesn't include the effect of saturation, the influence of anisotropy determined by the rotor position and the current phase angles, and the cross-coupling between the quadrature and direct axes. The values used for the position estimator are shown in Table 5.1. The results from the ideal machine are shown in Figure 5.6(a), (c), (e). Figure 5.6a shows the measured and the estimated electrical position. The position error shown in Figure 5.6c is obtained by subtracting the estimated electrical position from the measured one. While, Figure 5.6e shows the measured and the estimated mechanical speed. The results from the JMAG model of the motor studied in chapter 3 are shown in Figure 5.6(b), (d), (f). Figure 5.6b shows the measured and the estimated electrical position. The position error shown in Figure 5.6d is obtained by subtracting the estimated electrical position from the measured one. While, Figure 5.6f shows the measured and the estimated mechanical speed.

As mentioned earlier, the desired speed/angle profile is supplied to the motor in block G in Figure 5.5. This profile can be seen clearly in the measured mechanical speed in Figures 5.6e and f. For the ideal machine (Figures 5.6a, c, and e), it is clear that the position estimator works in an acceptable way. The estimated value follows the measured one in Figures 5.6a and e. The position error in Figure 5.6c is kept between 2.4 and -8 degrees. The estimated electrical angle follows the measured one in Figure 5.6a in a smooth way. However, some oscillations are noticed in the estimated mechanical speed in Figure 5.6e. The mechanical speed shouldn't change in a fast way like that. This may be due to the high bandwidth of the estimator. It is clear that some additional work is needed to tune the estimator. For the JMAG model (Figures 5.6b, d, and f), it is clear that the position estimator still works in an acceptable way where the estimated value follows the measured one in Figures 5.6b and f. The position error in Figure 5.6d became higher when compared with the ideal case and it is kept between 2.5 and -18.75 degrees. The estimated electrical angle follows the measured one in Figure 5.6b with some oscillations. Additionally, higher oscillations are noticed in the estimated mechanical speed in Figure 5.6f when compared with the ideal case. This may be due to the imperfect estimator tuning and the inclusion of the saturation effect, the influence of anisotropy determined by the rotor position, and the cross-coupling between the quadrature and direct axes.

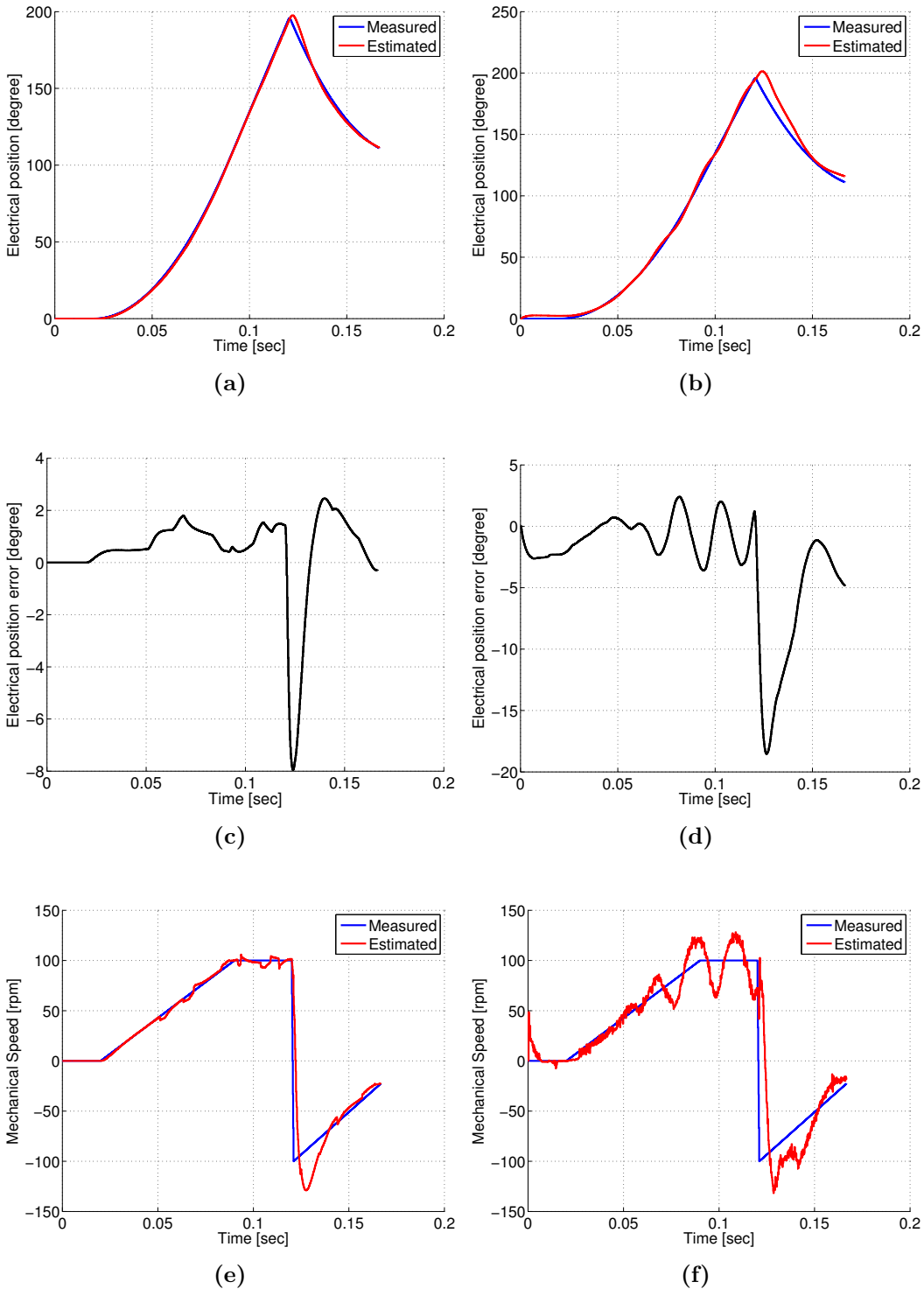

Figure 5.6:
The simulation results obtained by using the model of Bosch's position estimator: a) Measured and estimated electrical angle (ideal) b) Measured and estimated electrical angle (JMAG) c) Position error (ideal) d) Position error (JMAG) e) Measured and estimated mechanical speed (ideal) f) Measured and estimated mechanical speed (JMAG).

6

Verification of the Key Performance Indicator

In this chapter, some modifications are made to the model of the permanent magnet synchronous motor in Bosch's engine compartment actuator (ECA - E), shown in Figure 3.7, to change the level of harmonic content of the incremental inductances where both changes giving higher and lower harmonics are investigated. For each case the performance of the sensorless estimation is evaluated by using the KPI discussed in chapter 4 and simulations using Bosch's position estimator which is discussed in chapter 5. Additionally, the rated torque as well as the materials cost for each modification are also calculated.

6.1 Air holes in the rotor core

In this case, some holes are constructed in the rotor core in the direct axis direction. These holes are ten in total and they are placed under the permanent magnets on the rotor core. They are hollow on the inside which means that they are only full of air. The proposed modification can be shown in Figure 6.1. The same way of modeling in JMAG-Designer in chapter 3 is performed in this case and the air holes are added in the rotor core.

6.1.1 Incremental inductance

After the model creation in JMAG-Designer, the "Current signal input" block is generated using the JMAG-RT tool and it is used in the same way as discussed in section 4.2 in chapter 4 with Simulink to calculate the incremental inductances (L_{dd}, L_{qq}, L_{dq}, and L_{qd}) as well as their harmonic content. Similar to section 4.2, three loading conditions are studied: the full load, 30 % of the full load, and the no load.

The resulting incremental inductances (L_{dd}, L_{qq}, L_{dq}, and L_{qd}) as well as their

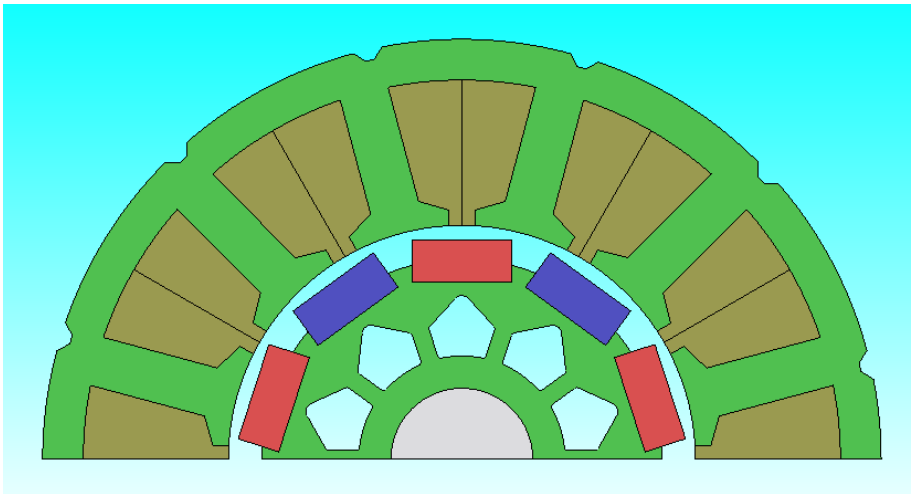

Figure 6.1:
The final 2D half model created by the "geometry editor" in JMAG-Designer including the shaft, rotor core, permanent magnets, stator core, and stator winding for section 6.1.

harmonic content are calculated with the method described in Section 4.2 and are shown in Figures 6.2 and 6.3 respectively. The resulting values of the incremental inductances (L_{dd}, L_{dq}, L_{qq}, and L_{qd}) plotted against the electrical position of the rotor at no load, 30 % of the full load, and full load are shown in Figures 6.2a, 6.2b, and 6.2c respectively. While, the resulting harmonic contents of the incremental inductances (L_{dd}, L_{dq}, L_{qq}, and L_{qd}) at three loads (0 %, 30 %, and 100 %) are shown in Figures 6.3a, 6.3b, 6.3c, and 6.3d respectively. It is worth mentioning that Figure 6.3 shows the magnitude of the harmonic components of the resulting incremental inductances. These magnitudes are calculated as a per unit representation respect to the offset value (the average inductance) of each related inductance at full load. Also, they are plotted against multiples of the frequency of the electrical period of the motor. Finally, Figure 6.3 is modified such that the DC component is not shown, to make the harmonic content appear in a more clear way as can be seen in Figure 6.4. It is clear from comparing Figure 4.12 of the original machine with Figure 6.4 that the harmonic content is more or less the same.

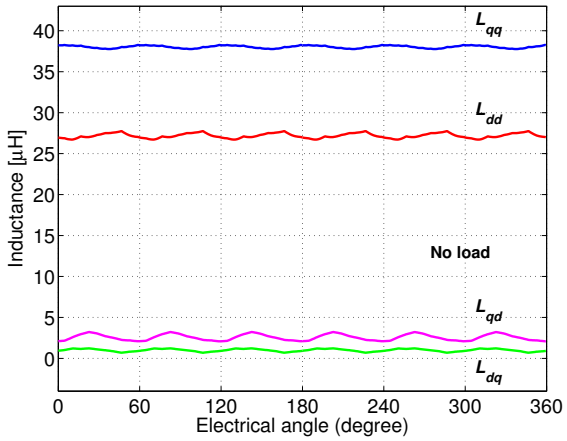

(a)

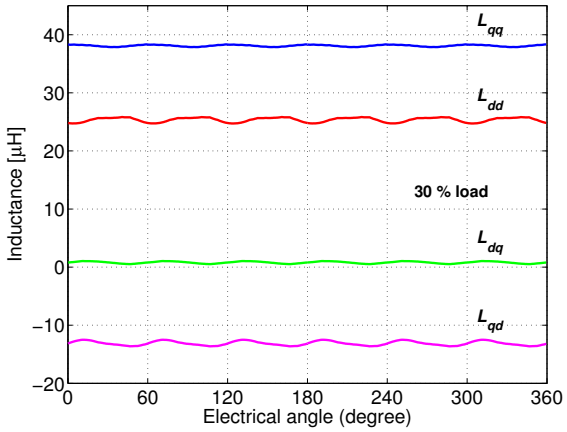

(b)

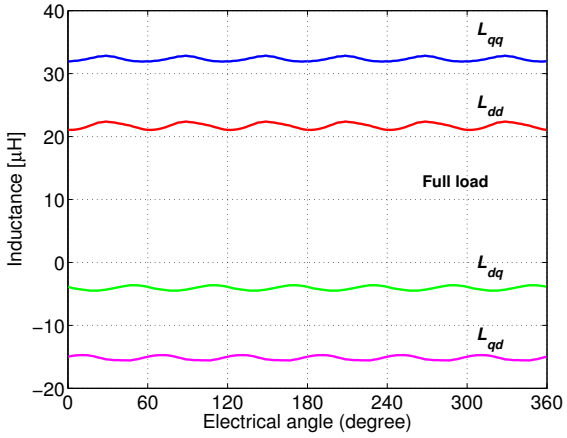

(c)

Figure 6.2:
The resulting values of the incremental inductances plotted against the electrical position of the rotor of the modified motor studied in section 6.1: a) No Load b) 30 % of the full load c) Full load.

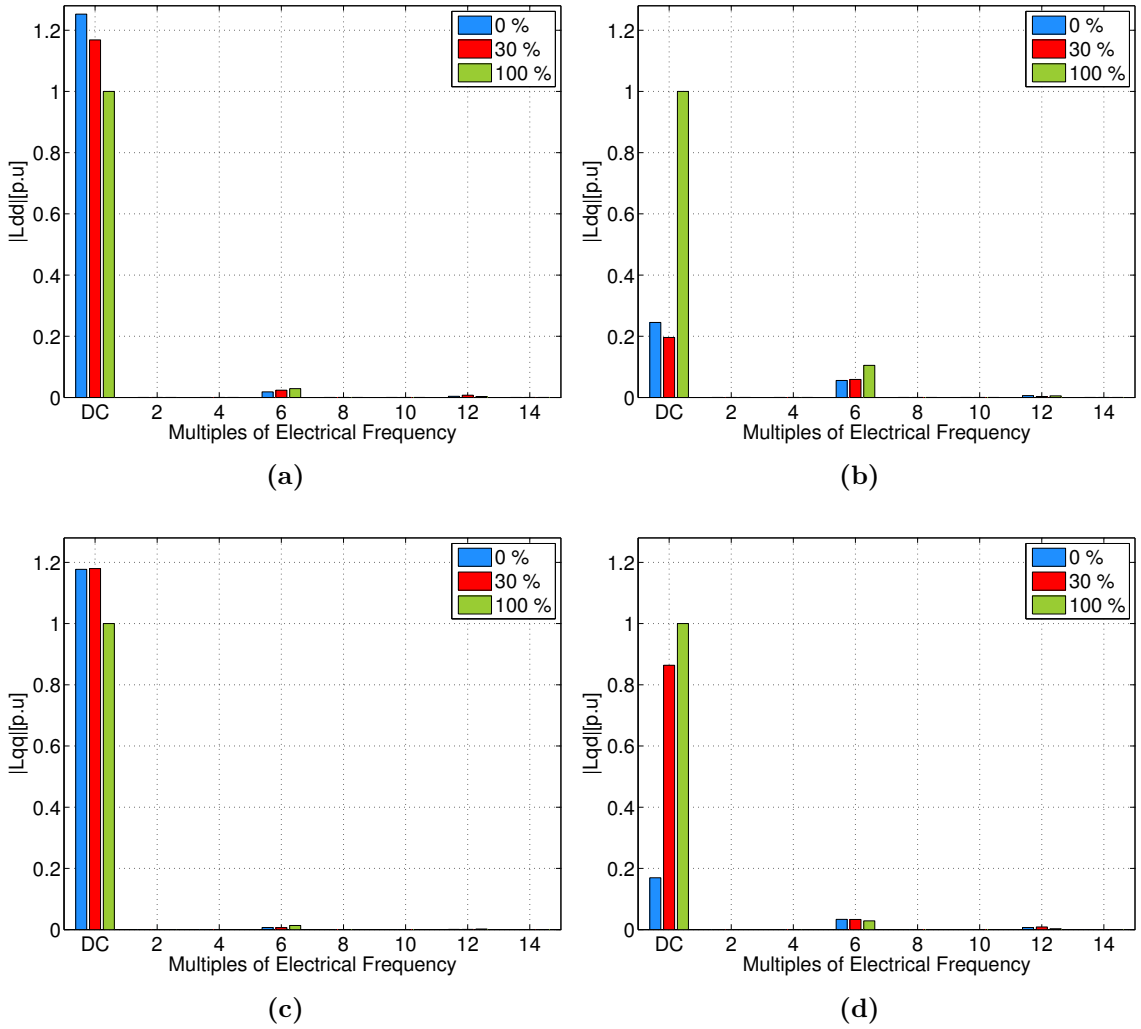

Figure 6.3:
The resulting harmonic content of the incremental inductances for the modified motor studied in section 6.1 at three loads (0 %, 30 %, and 100 %): a)L_{dd} b)L_{dq} c)L_{qq} d)L_{qd}.

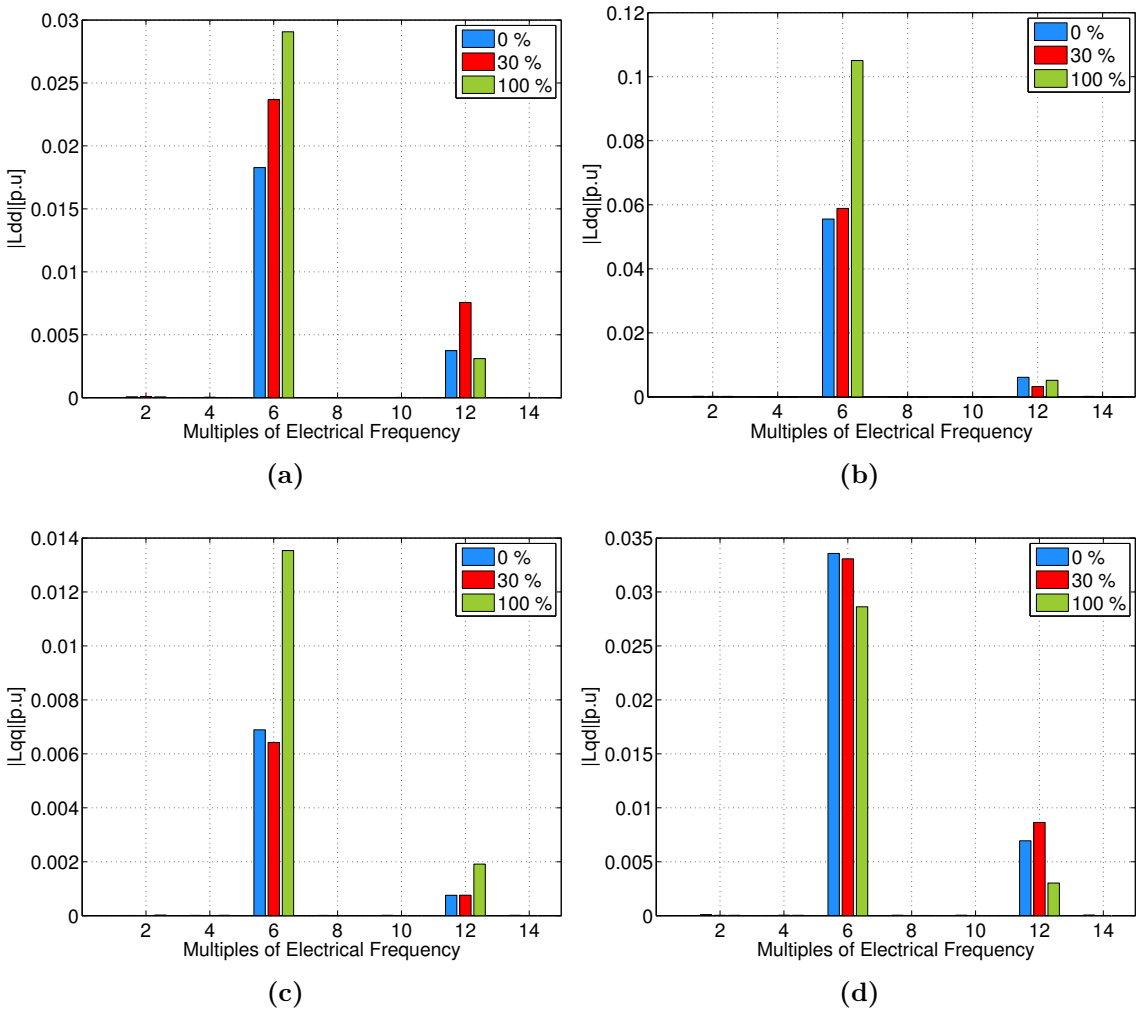

Figure 6.4:
The resulting harmonic content of the incremental inductances for the modified motor studied in section 6.1 at three loads (0 %, 30 %, and 100 %): a)L_{dd} b)L_{dq} c)L_{qq} d)L_{qd} where the DC component is not shown.

6.1.2 Sensorless performance evaluation

Similar to sections 5.4 and 5.5, the sensorless performance of the studied motor studied is evaluated with Bosch's simulated model of the position estimator and the JMAG model of the motor. The values used in Bosch's simulated model of the position estimator can be shown in Table 5.1 except for the direct and quadrature-axis inductances. The direct and quadrature-axis inductances are obtained as the average of the direct and quadrature axis self-inductances (L_{dd}, and L_{qq}) respectively at no load which can be seen in Figure 6.2a. The obtained results from the simulation are shown in Figure 6.5. Figure 6.5a shows the measured and the estimated electrical position. The position error shown in Figure 6.5b is obtained by subtracting the

estimated electrical position from the measured one. While, Figure 6.5c shows the measured and the estimated mechanical speed.

For the sensorless performance using the model of Bosch's position estimator, comparison can be made between Figure 5.6 for the original machine and Figure 6.5. The electrical position estimation errors which can be seen in Figures 5.6d and Figure 6.5b are also similar. These results agree with what is discussed in chapter 4 which implies that the similar harmonic content of the incremental inductances of two studied machines is an indication of a similar sensorless performance using saliency tracking.

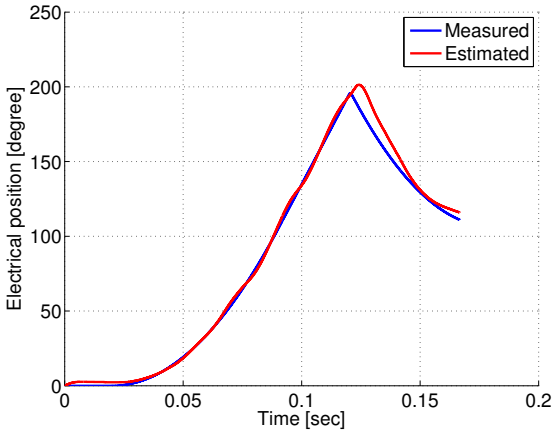

(a)

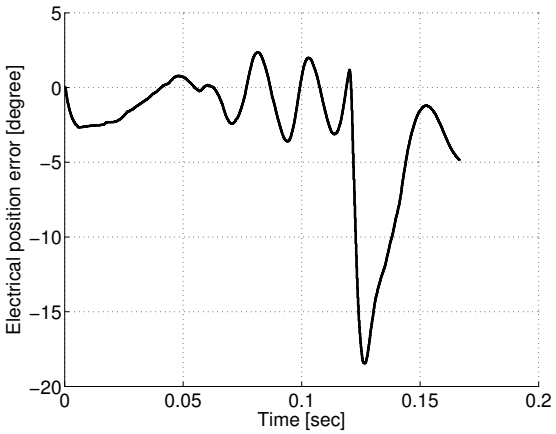

(b)

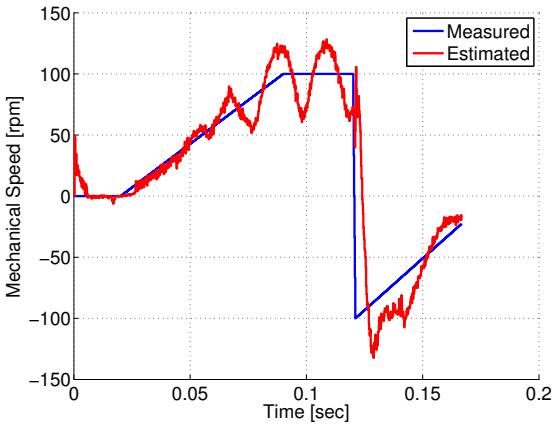

(c)

Figure 6.5:
The simulation results obtained by using the model of Bosch's position estimator and the motor studied in section 6.1: a) Measured and estimated electrical angle b) Position error c) Measured and estimated mechanical speed.

6.1.3 Rated torque and cost

Now, the rated torque of the modified machine should be simulated. Similar to section 3.2.4 in chapter 3, a 3-phase sinusoidal current source which has the phase rated current value and in phase with the 3-phase induced e.m.f is used and the machine is rotated at 2000 *rpm*. As seen from Figure 6.6, the average value of the simulated produced torque is about 1 *pu* where the base is selected as the average value of the simulated rated torque of the original machine that is seen in Figure 3.16.

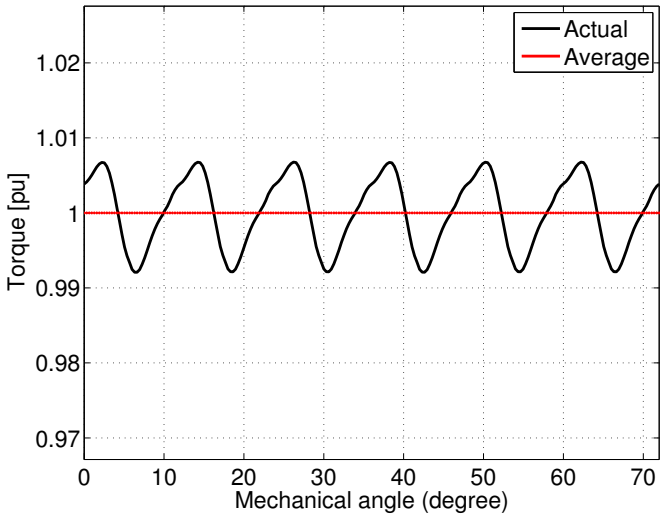

Figure 6.6:
Simulated rated torque which is obtained at the rated speed (2000 *rpm*) of the modified motor in section 6.1 (one complete electrical revolution equivalent to a mechanical angle rotation of about 72 °.

The calculation of the materials costs of the simulated machine is carried out in the same way as in chapter 3. The information about the densities of the materials as well as their prices are obtained from Tables 3.6 and 3.7 respectively. The final costs calculation of the simulated motor studied in section 6.1 can be shown in Table 6.1.

Table 6.1: The final costs calculation of the simulated motor studied in section 6.1.

Part	Volume (mm^3)	Cost (€)
Shaft	1009.84	0.00246
Rotor Core	3844.42	0.08396
Stator Core	12717.10	0.27774
Magnets	2688.00	4.37606
Stator Winding	4588.76	0.32782
Total Cost (€)		5.06805

From Figures 3.16 and 6.6, it can be noticed that the simulated rated torque values are equal. Finally, the total costs of the materials of the machine simulated in chapter 3 have decreased by nearly 0.78 % which can be seen by looking at Tables 3.8 and 6.1. The main reduction is in the rotor core because some parts of the steel material are removed to create the air holes. This means that the rotor core has a reduced weight which offers a reduced inertia and a better mechanical performance.

6.1.4 Summary

In conclusion, the addition of air holes in the rotor core in the direct axis direction didn't have any effect on the harmonic contents of the incremental inductances or the sensorless performance. This can be due to the fact that they are placed far from the magnets so the magnetic flux lines which are created between the poles are not affected. This modification can have an effect on the incremental inductances if the air holes are placed closer to the magnets. However, the practical implementation in manufacturing is not possible as the distance used in this section is the minimum distance allowed between the magnets and the air holes according to Bosch's manufacturing regulations. Finally, this modification can offer the same sensorless performance as well as the rated torque with a 0.78 % decrease in materials costs which is beneficial.

6.2 More steel between magnets

In this case, more steel material in the rotor core in the quadrature axis direction is added. By this modification, the motor becomes a "Surface-Inset PMSM" as studied in chapter 2. The proposed modification can be shown in Figure 6.7. The same way of modeling in JMAG-Designer in chapter 3 is performed in this case and the additional steel is added in the rotor core.

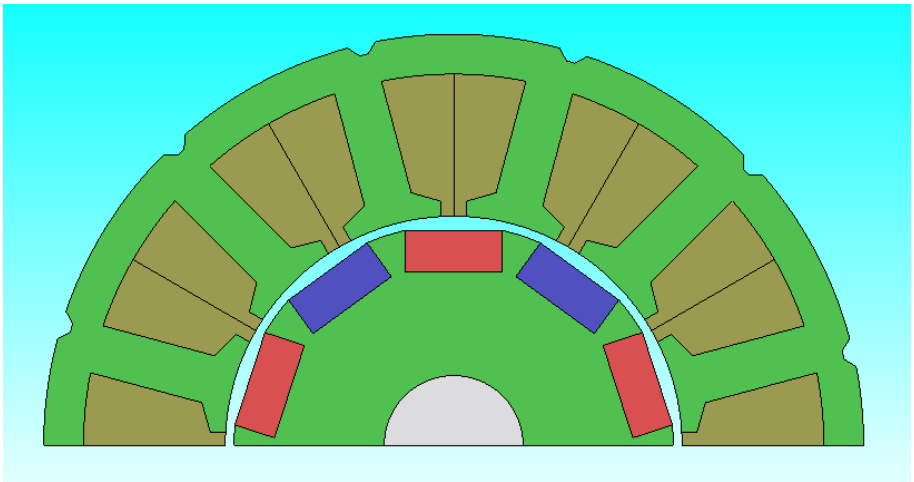

Figure 6.7:
The final 2D half model created by the "geometry editor" in JMAG-Designer including the shaft, rotor core, permanent magnets, stator core, and stator winding for section 6.2.

6.2.1 Incremental inductance

After the model creation in JMAG-Designer, the "Current signal input" block is generated using the JMAG-RT tool and it is used in the same way as discussed in section 4.2 in chapter 4 with Simulink to calculate the incremental inductances (L_{dd}, L_{qq}, L_{dq}, and L_{qd}) as well as their harmonic content. Similar to section 4.2, three loading conditions are studied: the full load, 30 % of the full load, and the no load.

The resulting incremental inductances (L_{dd}, L_{qq}, L_{dq}, and L_{qd}) as well as their harmonic content are calculated with the method described in Section 4.2 and are shown in Figures 6.8 and 6.9 respectively. The resulting values of the incremental inductances (L_{dd}, L_{dq}, L_{qq}, and L_{qd}) plotted against the electrical position of the rotor at no load, 30 % of the full load, and full load are shown in Figures 6.8a, 6.8b, and 6.8c respectively. While, the resulting harmonic content of the incremental inductances (L_{dd}, L_{dq}, L_{qq}, and L_{qd}) at three loads (0 %, 30 %, and 100 %) is shown

in Figures 6.9a, 6.9b, 6.9c, and 6.9d respectively. It is worth mentioning that Figure 6.9 shows the magnitude of the harmonic components of the resulting incremental inductances. These magnitudes are calculated as a per unit representation respect to the offset value (the average inductance) of each related inductance at full load. Also, they are plotted against multiples of the frequency of the electrical period of the motor. Finally, Figure 6.9 is modified such that the DC component is not shown, to make the harmonic content appear in a more clear way as can be seen in Figure 6.10.

From Figure 4.10 and Figure 6.8, it can be seen that the difference between the inductances L_{qq} and L_{dd} has increased by 50 % for the load 0 %. It has increased by 100 % for the load 30 %. While, it has decreased by 50 % for the load 100 %. The increase accompanied with the loads 0 % and 30 % may be due to the fact that adding more steel material in the rotor core in the quadrature axis direction makes the magnetic reluctance lower. Since, the inductance is inversely proportional to the reluctance [13], the quadrature axis inductance (L_{qq}) becomes larger and hence, the difference increases. The reduction accompanied with the load 100 % can be explained by the fact that the magnetic field becomes highly saturated with this load.

It is clear from comparing Figure 4.12 of the original machine with Figure 6.10 that the harmonic content of the machine in section 6.2 is mostly lower. For L_{dd}, the sixth harmonic component has decreased by 57 %, 63 %, and 80 % for the loads 0 %, 30 %, and 100 % respectively. For L_{dq}, the sixth harmonic component has decreased by 50 %, 62 %, and 42 % for the loads 0 %, 30 %, and 100 % respectively. For L_{qq}, the sixth harmonic component is approximately the same for the loads 0 % and 30 %, while, it has increased by 93 % for the load 100 %. For L_{qd}, the sixth harmonic component has decreased by 18 %, 58 %, and 17 % for the loads 0 %, 30 %, and 100 % respectively.

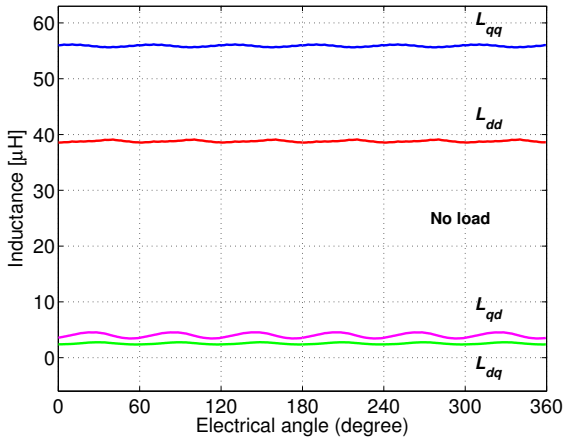

(a)

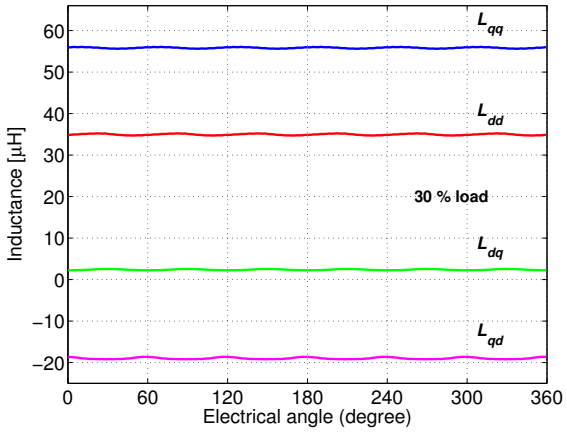

(b)

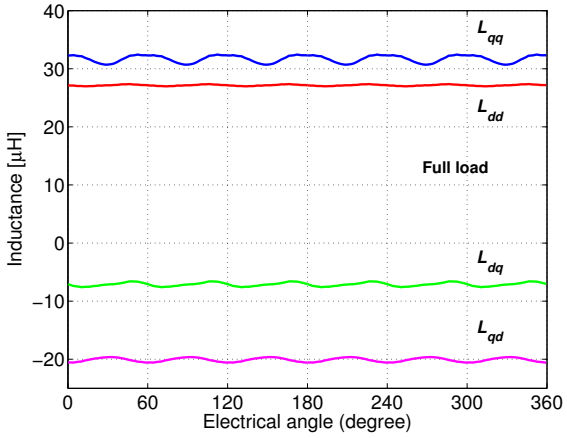

(c)

Figure 6.8:
The resulting values of the incremental inductances plotted against the electrical position of the rotor of the modified motor studied in section 6.2: a) No Load b) 30 % of the full load c) Full load.

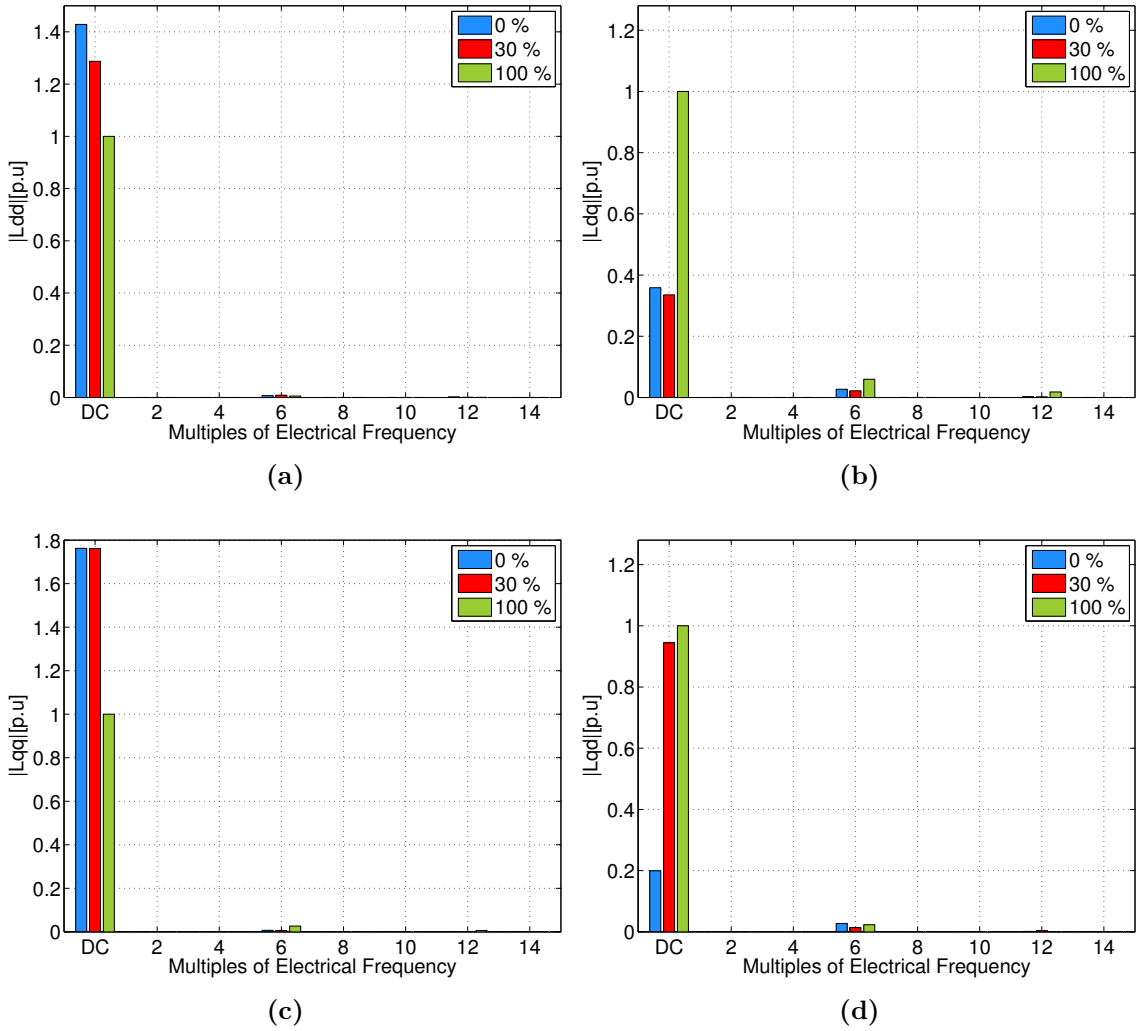

Figure 6.9:
The resulting harmonic content of the incremental inductances for the modified motor studied in section 6.2 at three loads (0 %, 30 %, and 100 %): a)L_{dd} b)L_{dq} c)L_{qq} d)L_{qd}.

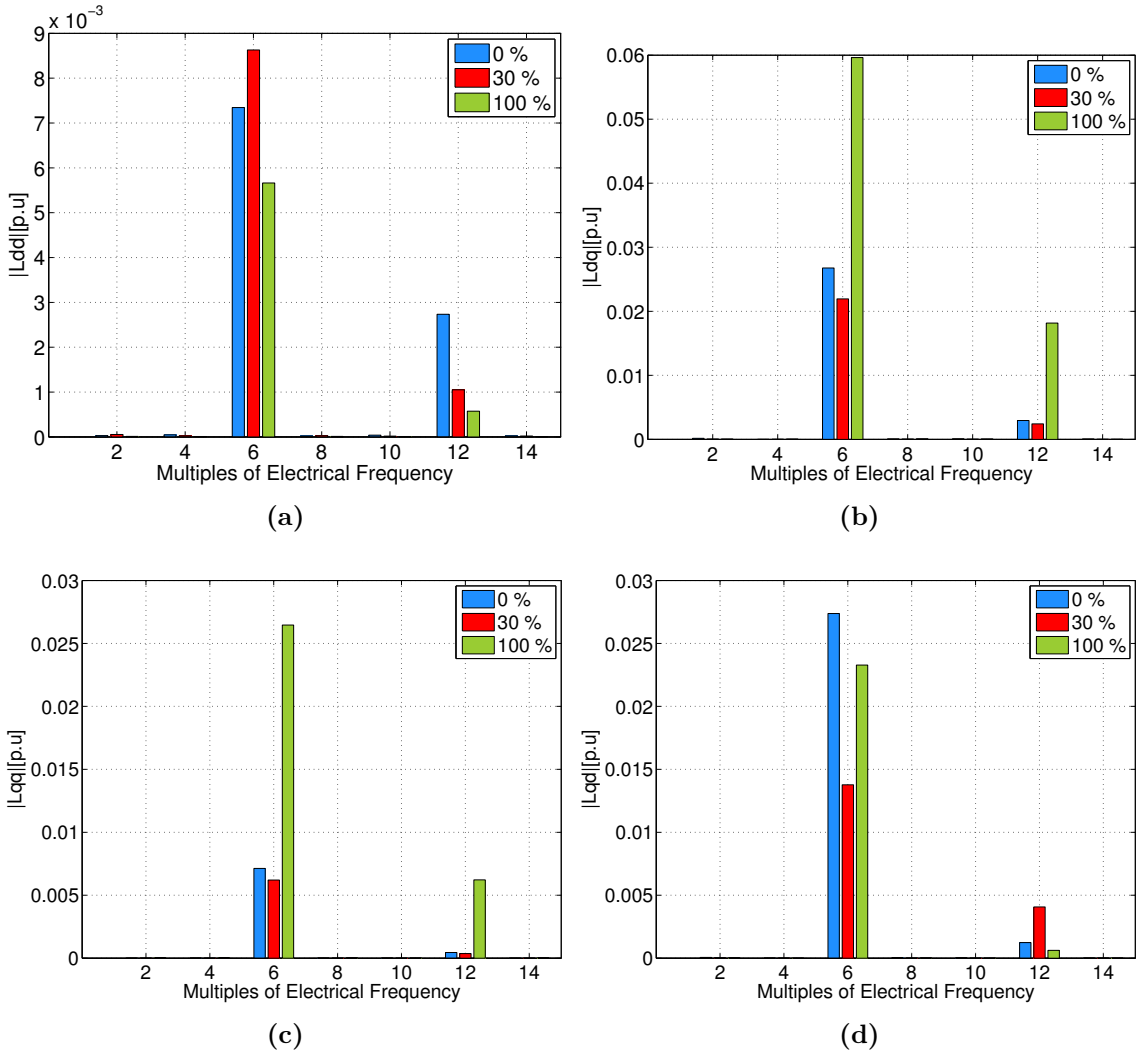

Figure 6.10:
The resulting harmonic content of the incremental inductances for the modified motor studied in section 6.2 at three loads (0 %, 30 %, and 100 %): a)L_{dd} b)L_{dq} c)L_{qq} d)L_{qd} where the DC component is not shown.

6.2.2 Sensorless performance evaluation

Similar to sections 5.4 and 5.5, the sensorless performance of the studied motor is evaluated with Bosch's simulated model of the position estimator and the JMAG model of the motor. The values used in Bosch's simulated model of the position estimator can be shown in Table 5.1 except for the direct and quadrature-axis inductances. The direct and quadrature-axis inductances are obtained as the average of the direct and quadrature axis self-inductances (L_{dd}, and L_{qq}) respectively at no load which can be seen in Figure 6.8a. The obtained results from the simulation are shown in Figure 6.11. Figure 6.11a shows the measured and the estimated electrical

position. The position error shown in Figure 6.11b is obtained by subtracting the estimated electrical position from the measured one. While, Figure 6.11c shows the measured and the estimated mechanical speed.

For the sensorless performance using the model of Bosch's position estimator, comparison can be made between Figure 5.6 for the original machine and Figure 6.11. The electrical position estimation error of the machine studied in section 6.2 (kept between 0.5 and -18.75 degrees) which can be seen in Figure 6.11b is lower than that of the original machine (kept between 2.5 and -18.75 degrees) which can be seen in Figure 5.6d. Also, the oscillations in the mechanical speed in Figure 6.11c are lower than those in Figure 5.6f. These results agree with what is discussed in chapter 4 which implies that the lower harmonic contents of the incremental inductances is an indication of a better sensorless performance using saliency tracking.

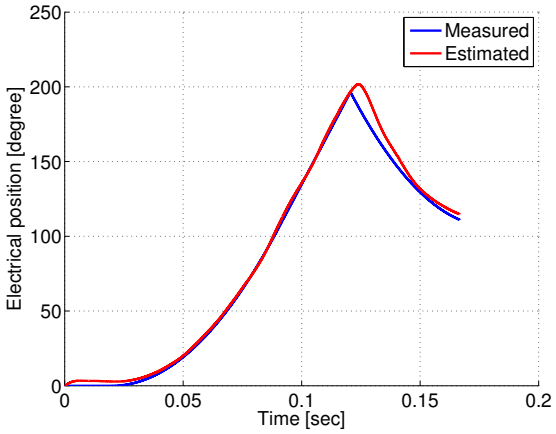

(a)

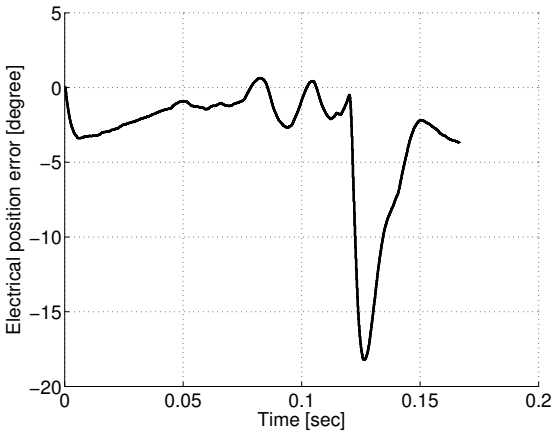

(b)

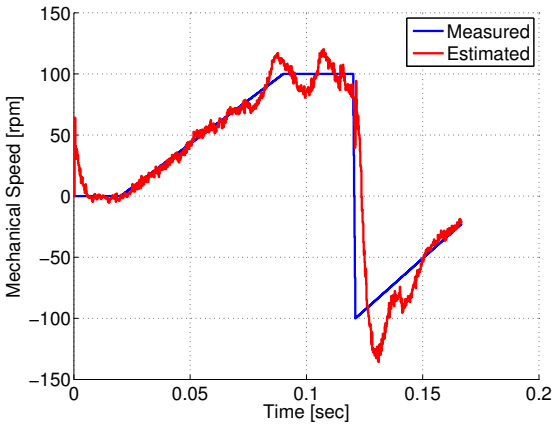

(c)

Figure 6.11:
The simulation results obtained by using the model of Bosch's position estimator and the motor studied in section 6.2: a) Measured and estimated electrical angle b) Position error c) Measured and estimated mechanical speed.

6.2.3 Rated torque and cost

Now, the rated torque of the modified machine should be simulated. Similar to section 3.2.4 in chapter 3, a 3-phase sinusoidal current source which has the phase rated current value and in phase with the 3-phase induced e.m.f is used and the machine is rotated at 2000 *rpm*. As seen from Figure 6.12, the average value of the simulated produced torque is about 0.8433 *pu* where the base is selected as the average value of the simulated rated torque of the original machine that is seen in Figure 3.16.

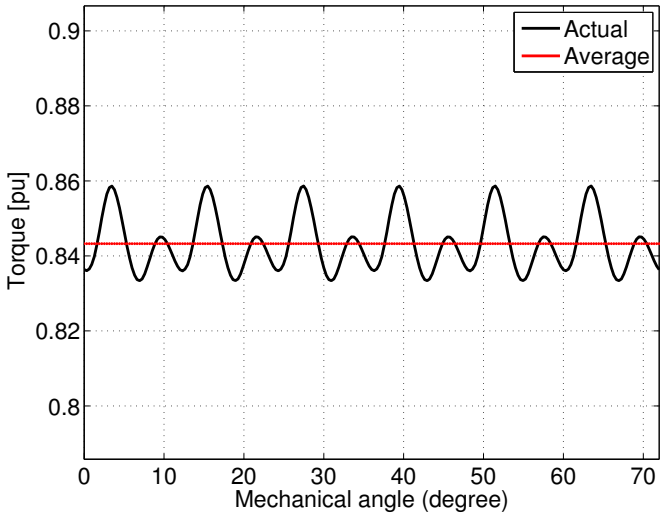

Figure 6.12:
Simulated rated torque which is obtained at the rated speed (2000 *rpm*) of the modified motor in section 6.2 (one complete electrical revolution equivalent to a mechanical angle rotation of about 72 °).

The calculation of the materials costs of the simulated machine is carried out in the same way as in chapter 3. The information about the densities of the materials as well as their prices are obtained from Tables 3.6 and 3.7 respectively. The final costs calculation of the simulated motor studied in section 6.2 can be shown in Table 6.2.

Table 6.2: The final costs calculation of the simulated motor studied in section 6.2.

Part	Volume (mm^3)	Cost (€)
Shaft	1009.84	0.00246
Rotor Core	6190.59	0.13520
Stator Core	12717.10	0.27774
Magnets	2688.00	4.37606
Stator Winding	4588.76	0.32782
Total Cost (€)		5.11929

From Figures 3.16 and 6.12, it can be noticed that the simulated rated torque has decreased by nearly 15.6 %. This reduction may be due to the fact that the maximum torque per ampere (MTPA) condition is not used. Finally, the total costs of the materials of the machine simulated in chapter 3 have increased by nearly 0.22 % which can be seen by looking at Tables 3.8 and 6.2. The main increase is in the rotor core because some parts of the steel material are added in the quadrature axis direction. This means that the rotor core has an increased weight which offers an increased inertia.

6.2.4 Summary

In conclusion, the results verifies that the "the level of harmonic disturbance in the incremental inductances (L_{dd}, L_{qq}, L_{dq}, and L_{qd}) can be used as a key performance indicator to give a preliminary evaluation of the capability of a certain PM synchronous machine to perform sensorless vector control in a better quality using saliency tracking in comparison with a base machine". This is useful when performing iterations in the machine design stage. Additionally, it is found that adding more steel material in the rotor core in the quadrature axis direction makes the harmonic content of the incremental inductances lower and, consequently, a better sensorless performance is obtained. However, this improvement has a price where there is a decrease in the rated toque and an increase in the materials costs.

6.3 Totally-closed slot openings

In this case, the openings of the stator slots are totally closed. They are filled with the same steel material as the stator core. The proposed modification can be shown in Figure 6.13. The same way of modeling in JMAG-Designer in chapter 3 is performed in this case and the slot openings are filled with the steel material.

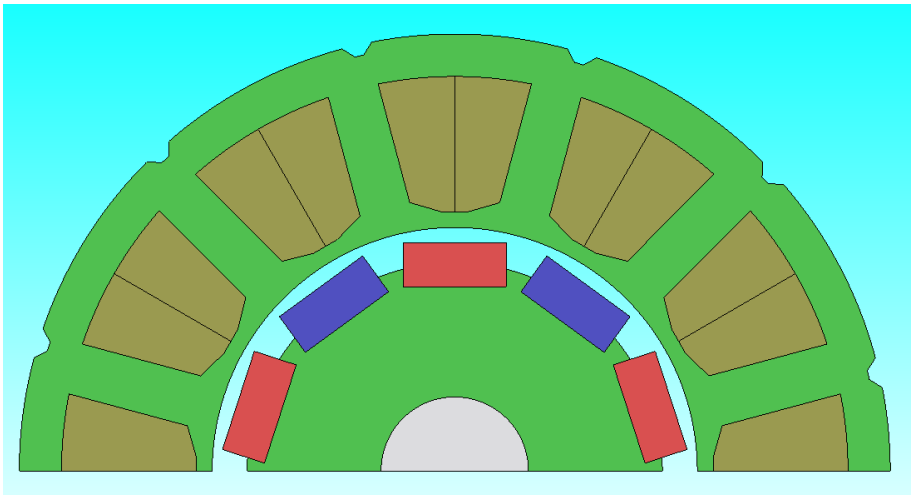

Figure 6.13:
The final 2D half model created by the "geometry editor" in JMAG-Designer including the shaft, rotor core, permanent magnets, stator core, and stator winding for section 6.3.

6.3.1 Incremental inductance

After the model creation in JMAG-Designer, the "Current signal input" block is generated using the JMAG-RT tool and it is used in the same way as discussed in section 4.2 in chapter 4 with Simulink to calculate the incremental inductances (L_{dd}, L_{qq}, L_{dq}, and L_{qd}) as well as their harmonic content. Similar to section 4.2, three loading conditions are studied: the full load, 30 % of the full load, and the no load.

The resulting incremental inductances (L_{dd}, L_{qq}, L_{dq}, and L_{qd}) as well as their harmonic content are calculated with the method described in Section 4.2 and are shown in Figures 6.14 and 6.15 respectively. The resulting values of the incremental inductances (L_{dd}, L_{dq}, L_{qq}, and L_{qd}) plotted against the electrical position of the rotor at no load, 30 % of the full load, and full load are shown in Figures 6.14a, 6.14b, and 6.14c respectively. While, the resulting harmonic content of the incremental inductances (L_{dd}, L_{dq}, L_{qq}, and L_{qd}) at three loads (0 %, 30 %, and 100 %) is shown in Figures 6.15a, 6.15b, 6.15c, and 6.15d respectively. It is worth mentioning that

Figure 6.15 shows the magnitude of the harmonic components of the resulting incremental inductances. These magnitudes are calculated as a per unit representation respect to the offset value (the average inductance) of each related inductance at full load. Also, they are plotted against multiples of the frequency of the electrical period of the motor. Finally, Figure 6.15 is modified such that the DC component is not shown, to make the harmonic content appear in a more clear way as can be seen in Figure 6.16.

From Figure 4.10 and Figure 6.14, it can be seen that the difference between the inductances L_{qq} and L_{dd} has increased by 400 % for the load 0 %. It has increased by 100 % for the load 30 %. Similarly, it has increased by 100 % for the load 100 % but in this case L_{dd} became larger than L_{qq} (loss of saliency). The fact that L_{dd} became larger than L_{qq} may be due to the high level of saturation at this load.

It is clear from comparing Figure 4.12 of the original machine with Figure 6.16 that the harmonic content of the machine in section 6.3 is mostly higher in a big way. For L_{dd}, the sixth harmonic component has increased by 242 %, 657 %, and 331 % for the loads 0 %, 30 %, and 100 % respectively. For L_{dq}, the sixth harmonic component has increased by 1536 %, 858 %, and 138 % for the loads 0 %, 30 %, and 100 % respectively. For L_{qq}, the sixth harmonic component has increased by 3292 %, and 669 % for the loads 0 %, and 30 % respectively, while, it has decreased by 8 % for the load 100 %. For L_{qd}, the sixth harmonic component has increased by 455 %, 733 %, and 456 % for the loads 0 %, 30 %, and 100 % respectively.

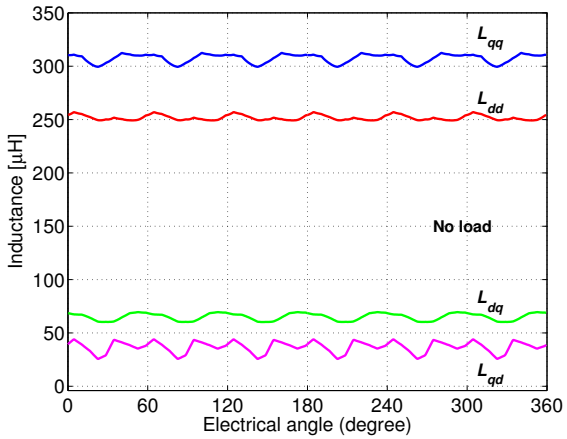

(a)

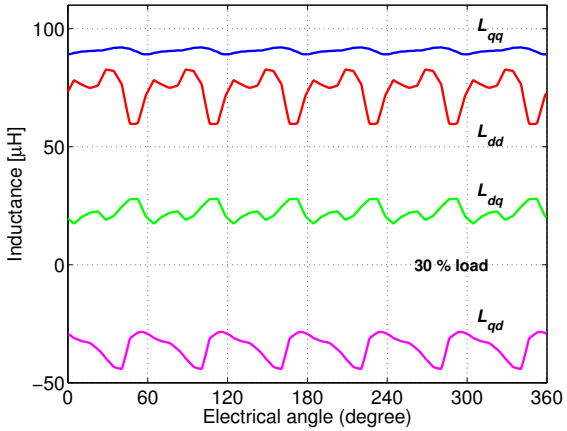

(b)

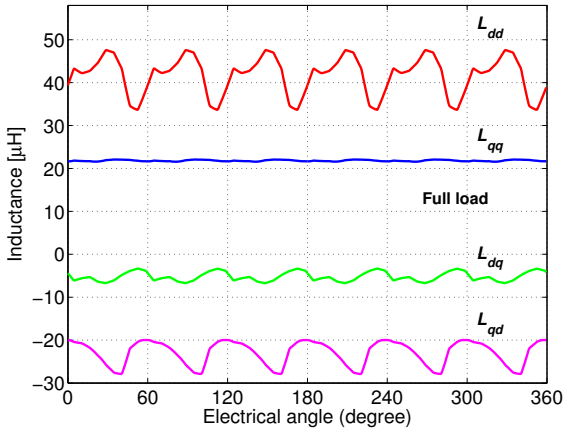

(c)

Figure 6.14:
The resulting values of the incremental inductances plotted against the electrical position of the rotor of the modified motor studied in section 6.3: a) No Load b) 30 % of the full load c) Full load.

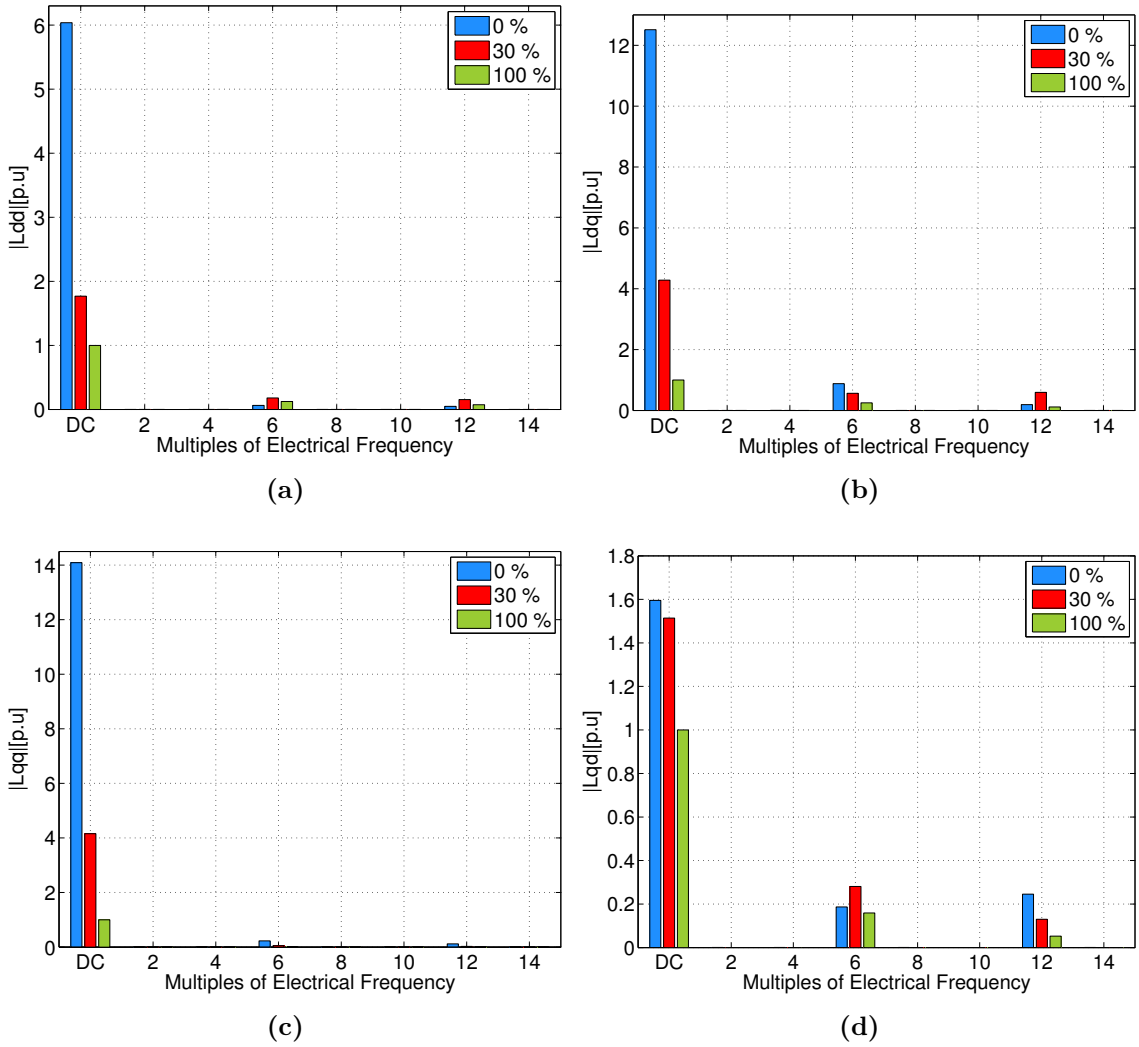

Figure 6.15:
The resulting harmonic content of the incremental inductances for the modified motor studied in section 6.3 at three loads (0 %, 30 %, and 100 %): a)L_{dd} b)L_{dq} c)L_{qq} d)L_{qd}.

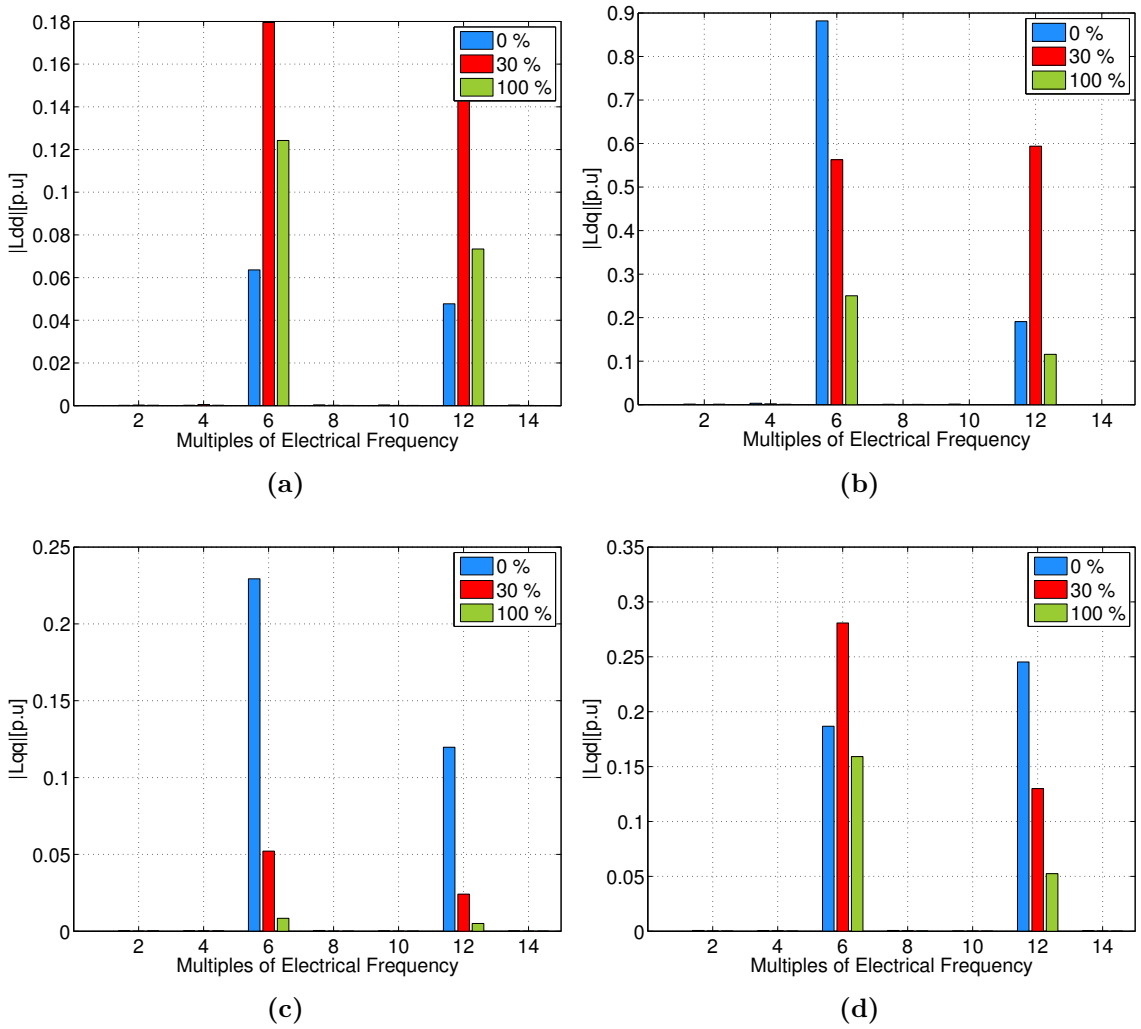

Figure 6.16:
The resulting harmonic content of the incremental inductances for the modified motor studied in section 6.3 at three loads (0 %, 30 %, and 100 %): a)L_{dd} b)L_{dq} c)L_{qq} d)L_{qd} where the DC component is not shown.

6.3.2 Sensorless performance evaluation

Similar to sections 5.4 and 5.5, the sensorless performance of the studied motor is evaluated with Bosch's simulated model of the position estimator and the JMAG model of the motor. The values used in Bosch's simulated model of the position estimator can be shown in Table 5.1 except for the direct and quadrature-axis inductances. The direct and quadrature-axis inductances are obtained as the average of the direct and quadrature axis self-inductances (L_{dd}, and L_{qq}) respectively at no load which can be seen in Figure 6.14a. The obtained results from the simulation are shown in Figure 6.17. Figure 6.17a shows the measured and the estimated electrical

position. The position error shown in Figure 6.17b is obtained by subtracting the estimated electrical position from the measured one. While, Figure 6.17c shows the measured and the estimated mechanical speed.

For the sensorless performance using the model of Bosch's position estimator, comparison can be made between Figure 5.6 for the original motor and Figure 6.17. It is clear from Figure 6.17 that the position estimator fails to work as intended. It is not able to estimate the position or the speed of the motor. These results agree with what is discussed in chapter 4 which implies that the higher harmonic contents of the incremental inductances is an indication of a worse sensorless performance using saliency tracking (In this case, it doesn't work at all because of the very high harmonic content of the incremental inductances and because the machine loses the saliency at full load ($L_{dd} > L_{qq}$)).

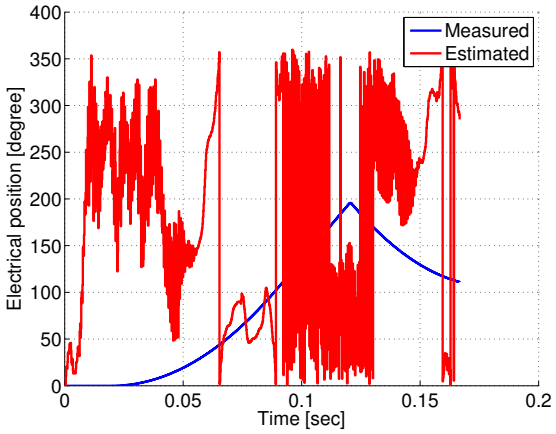

(a)

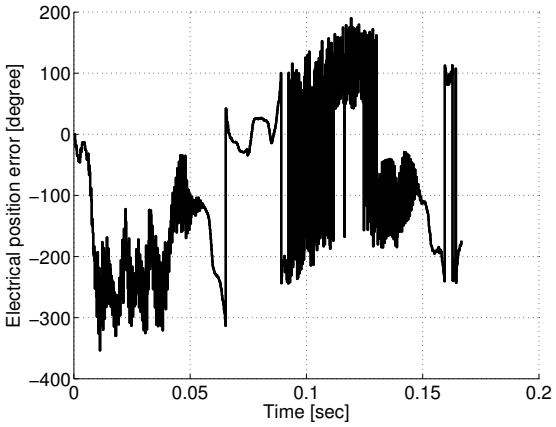

(b)

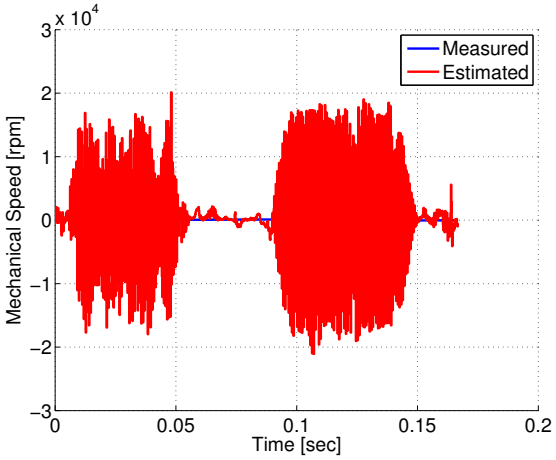

(c)

Figure 6.17:
The simulation results obtained by using the model of Bosch's position estimator and the motor studied in section 6.3: a) Measured and estimated electrical angle b) Position error c) Measured and estimated mechanical speed.

6.3.3 Rated torque and cost

Now, the rated torque of the modified machine should be simulated. Similar to section 3.2.4 in chapter 3, a 3-phase sinusoidal current source which has the phase rated current value and in phase with the 3-phase induced e.m.f is used and the machine is rotated at 2000 *rpm*. As seen from Figure 6.18, the average value of the simulated produced torque is about 0.6229 *pu* where the base is selected as the average value of the simulated rated torque of the original machine that is seen in Figure 3.16.

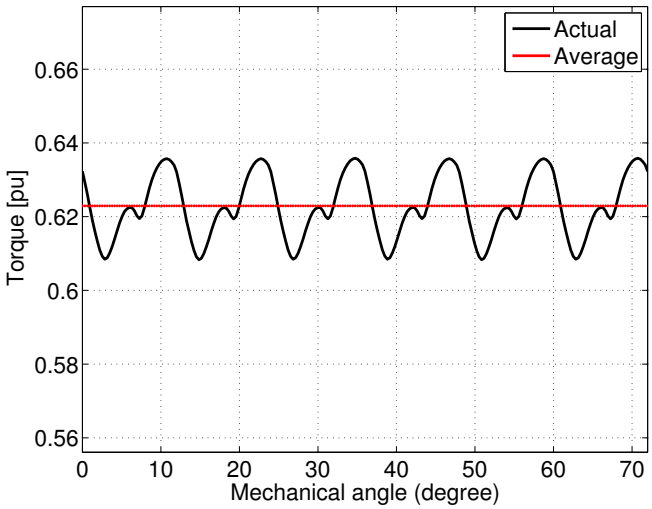

Figure 6.18:
Simulated rated torque which is obtained at the rated speed (2000 *rpm*) of the modified motor in section 6.3 (one complete electrical revolution equivalent to a mechanical angle rotation of about 72 °).

The calculation of the materials costs of the simulated machine is carried out in the same way as in chapter 3. The information about the densities of the materials as well as their prices are obtained from Tables 3.6 and 3.7 respectively. The final costs calculation of the simulated motor studied in section 6.3 can be shown in Table 6.3. Please, note that the volume of the stator winding is kept the same.

Table 6.3: The final costs calculation of the simulated motor studied in section 6.3.

Part	Volume (mm^3)	Cost (€)
Shaft	1009.84	0.00246
Rotor Core	5665.49	0.12373
Stator Core	13031.11	0.28460
Magnets	2688.00	4.37606
Stator Winding	4588.76	0.32782
Total Cost (€)		5.11468

From Figures 3.16 and 6.18, it can be noticed that the simulated rated torque has decreased by nearly 37.7 %. Finally, the total costs of the materials of the machine simulated in chapter 3 have increased by nearly 0.13 % which can be seen by looking at Tables 3.8 and 6.3. The main increase is in the stator core because some parts of the steel material are added to close the openings of the stator slots. This means that the stator core has an increased weight.

6.3.4 Summary

In conclusion, the results verifies that the "the level of harmonic disturbance in the incremental inductances (L_{dd}, L_{qq}, L_{dq}, and L_{qd}) can be used as a key performance indicator to give a preliminary evaluation of the capability of a certain PM synchronous machine to perform sensorless vector control in a better or worse quality using saliency tracking in comparison with a base machine". Additionally, it is found that closing the openings of the stator slots makes the harmonic contents of the incremental inductances higher in a big way and, consequently, a worse sensorless performance is obtained where the position estimator fails to work.

6.4 Bigger stator teeth width

In this case, the width of the stator teeth is increased. The proposed modification can be shown in Figure 6.19. The same way of modeling in JMAG-Designer in chapter 3 is performed in this case and the wider stator teeth are created.

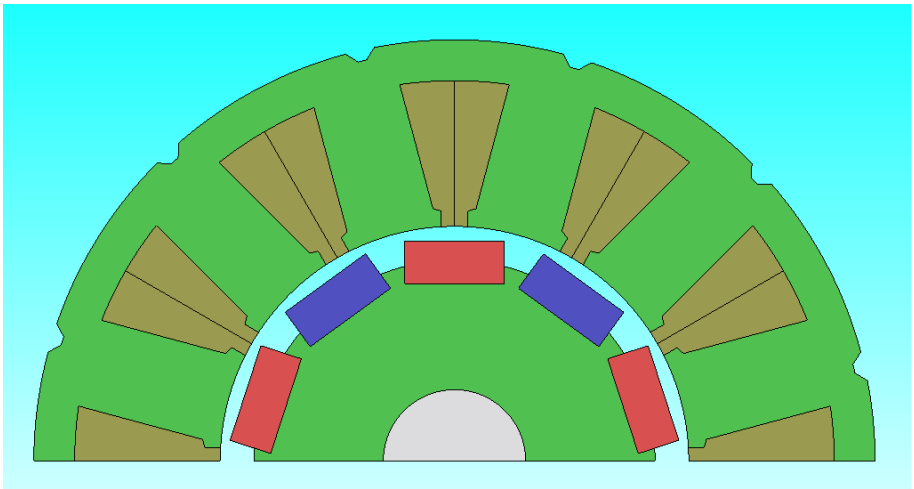

Figure 6.19:
The final 2D half model created by the "geometry editor" in JMAG-Designer including the shaft, rotor core, permanent magnets, stator core, and stator winding for section 6.4.

6.4.1 Incremental inductance

After the model creation in JMAG-Designer, the "Current signal input" block is generated using the JMAG-RT tool and it is used in the same way as discussed in section 4.2 in chapter 4 with Simulink to calculate the incremental inductances (L_{dd}, L_{qq}, L_{dq}, and L_{qd}) as well as their harmonic content. Similar to section 4.2, three loading conditions are studied: the full load, 30 % of the full load, and the no load.

The resulting incremental inductances (L_{dd}, L_{qq}, L_{dq}, and L_{qd}) as well as their harmonic content are calculated with the method described in Section 4.2 and are shown in Figures 6.20 and 6.21 respectively. The resulting values of the incremental inductances (L_{dd}, L_{dq}, L_{qq}, and L_{qd}) plotted against the electrical position of the rotor at no load, 30 % of the full load, and full load are shown in Figures 6.20a, 6.20b, and 6.20c respectively. While, the resulting harmonic content of the incremental inductances (L_{dd}, L_{dq}, L_{qq}, and L_{qd}) at three loads (0 %, 30 %, and 100 %) is shown in Figures 6.21a, 6.21b, 6.21c, and 6.21d respectively. It is worth mentioning that Figure 6.21 shows the magnitude of the harmonic components of the resulting incre-

mental inductances. These magnitudes are calculated as a per unit representation respect to the offset value (the average inductance) of each related inductance at full load. Also, they are plotted against multiples of the frequency of the electrical period of the motor. Finally, Figure 6.21 is modified such that the DC component is not shown, to make the harmonic content appear in a more clear way as can be seen in Figure 6.22.

From Figure 4.10 and Figure 6.20, it can be seen that the difference between the inductances L_{qq} and L_{dd} has decreased by 80 % for the load 0 %. It has decreased by 55 % for the load 30 %. While, it has decreased by 50 % for the load 100 %. Hence, the saliency level has decreased in comparison with the original machine.

It is clear from comparing Figure 4.12 of the original machine with Figure 6.22 that the harmonic content of the machine in section 6.4 is mostly lower. For L_{dd}, the sixth harmonic component has decreased by 75 %, 94 %, and 70 % for the loads 0 %, 30 %, and 100 % respectively. For L_{dq}, the sixth harmonic component has decreased by 27 % and 33 % for the loads 0 % and 30 % respectively, while, it has increased by 376 % for the load 100 %. For L_{qq}, the sixth harmonic component has decreased by 94.6 %, 94.2 %, and 76 % for the loads 0 %, 30 %, and 100 % respectively. For L_{qd}, the sixth harmonic component has decreased by 85 %, 96 %, and 40 % for the loads 0 %, 30 %, and 100 % respectively.

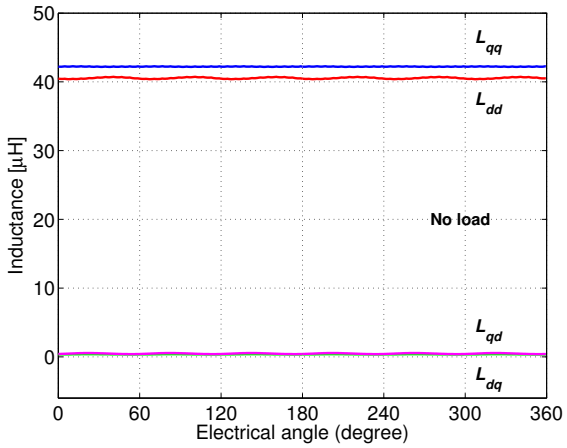

(a)

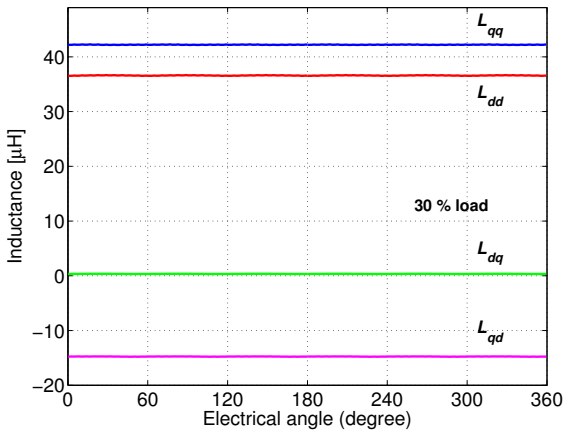

(b)

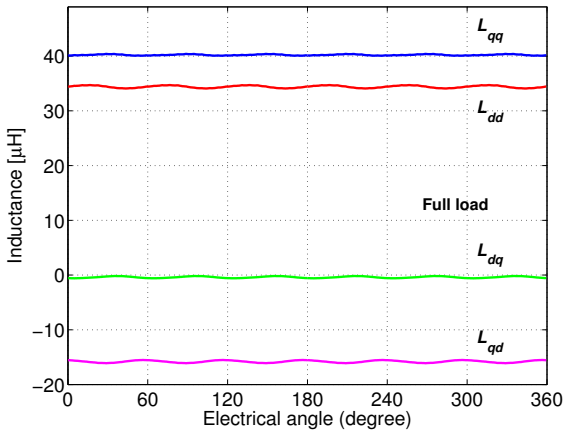

(c)

Figure 6.20:
The resulting values of the incremental inductances plotted against the electrical position of the rotor of the modified motor studied in section 6.4: a) No Load b) 30 % of the full load c) Full load.

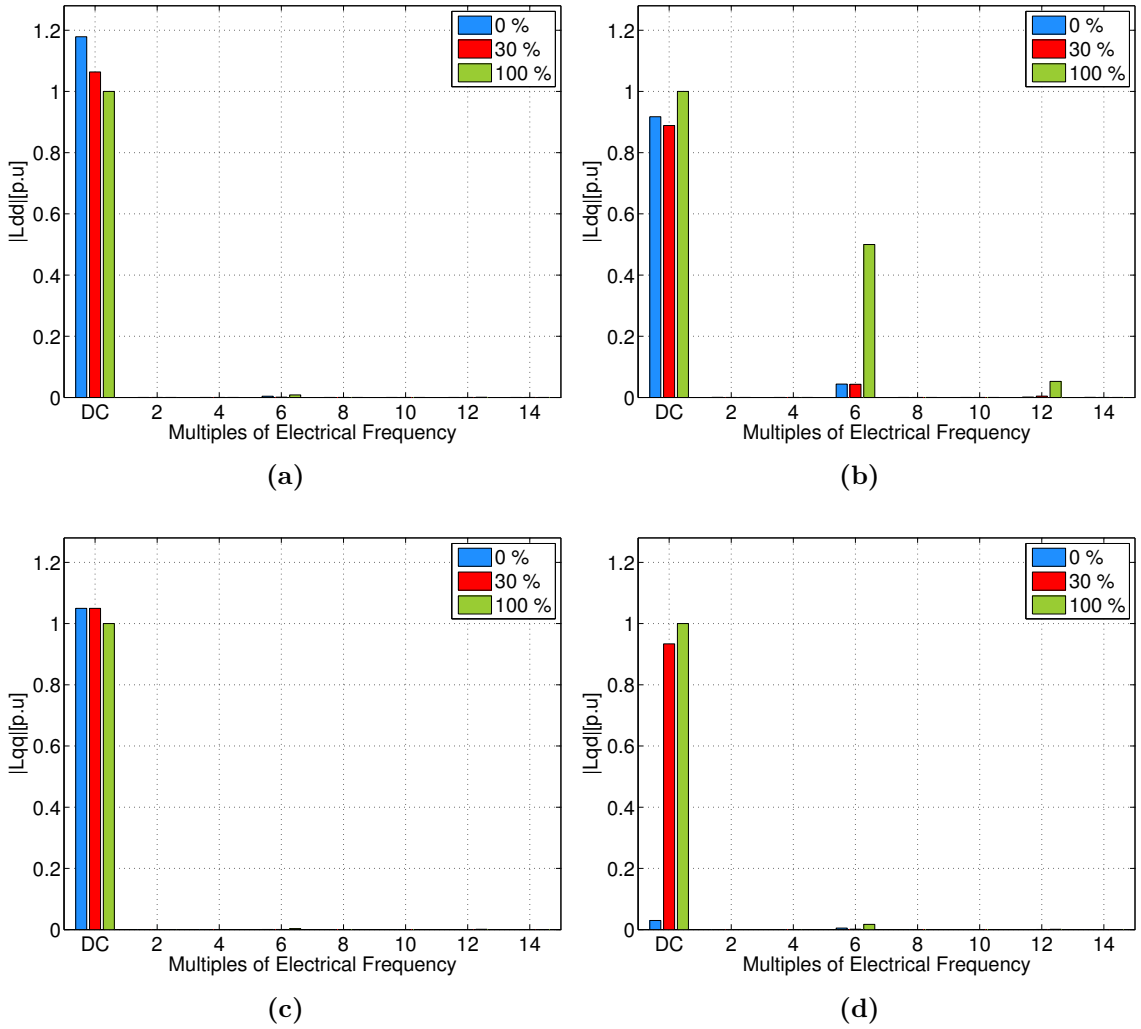

Figure 6.21:
The resulting harmonic content of the incremental inductances for the modified motor studied in section 6.4 at three loads (0 %, 30 %, and 100 %): a)L_{dd} b)L_{dq} c)L_{qq} d)L_{qd}.

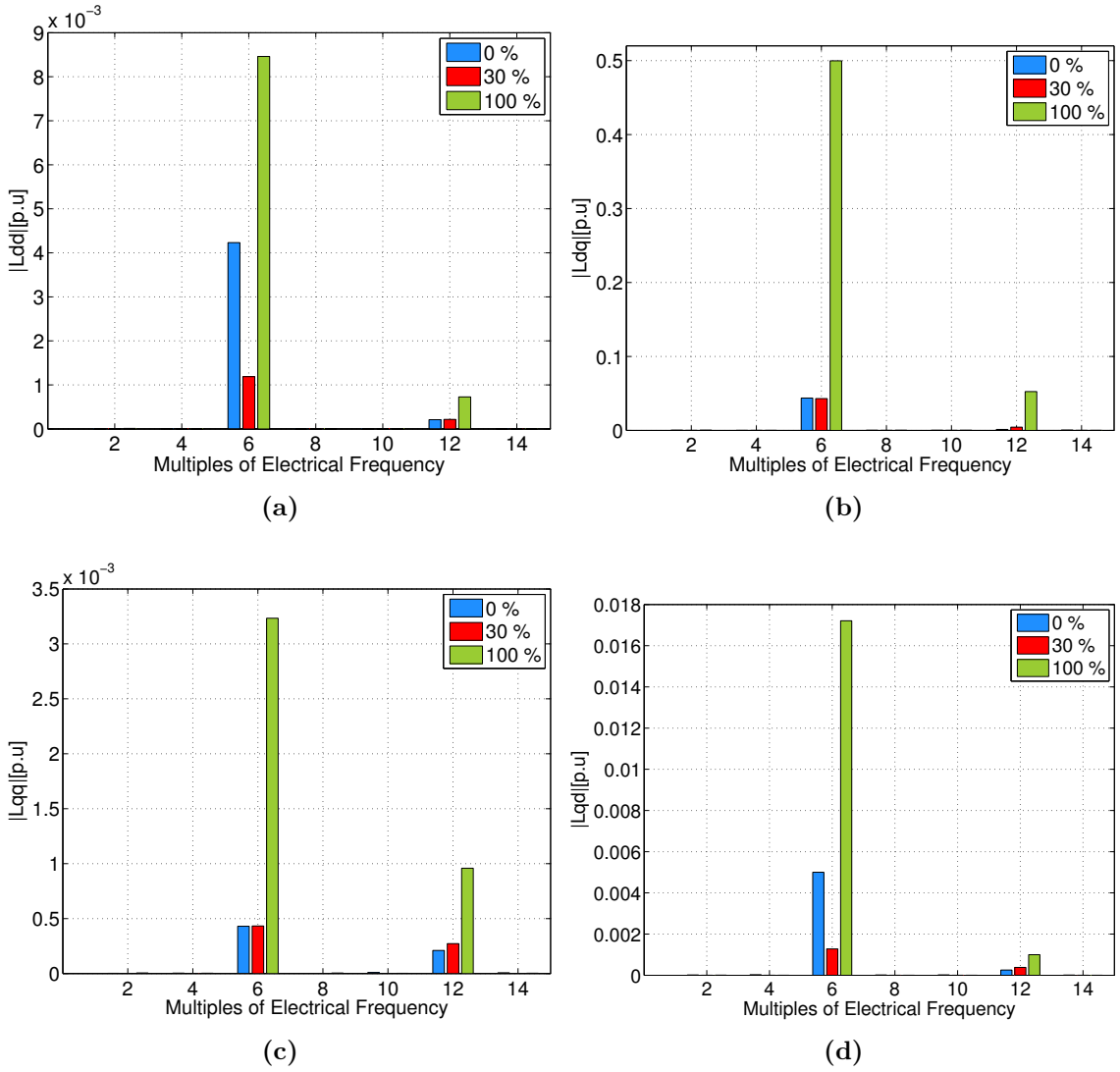

Figure 6.22:
The resulting harmonic content of the incremental inductances for the modified motor studied in section 6.4 at three loads (0 %, 30 %, and 100 %): a)L_{dd} b)L_{dq} c)L_{qq} d)L_{qd} where the DC component is not shown.

6.4.2 Sensorless performance evaluation

Similar to sections 5.4 and 5.5, the sensorless performance of the studied motor is evaluated with Bosch's simulated model of the position estimator and the JMAG model of the motor. The values used in Bosch's simulated model of the position estimator can be shown in Table 5.1 except for the direct and quadrature-axis inductances. The direct and quadrature-axis inductances are obtained as the average of the direct and quadrature axis self-inductances (L_{dd}, and L_{qq}) respectively at no load which can be seen in Figure 6.20a. The obtained results from the simulation are

shown in Figure 6.23. Figure 6.23a shows the measured and the estimated electrical position. The position error shown in Figure 6.23b is obtained by subtracting the estimated electrical position from the measured one. While, Figure 6.23c shows the measured and the estimated mechanical speed.

For the sensorless performance using the model of Bosch's position estimator, comparison can be made between Figure 5.6 for the original machine and Figure 6.23. It is clear from Figure 6.23 that the position estimator fails to work as intended. It is not able to estimate the position or the speed of the motor. This can be explained by the fact that the difference between the direct and quadrature axis self-inductances (L_{dd}, and L_{qq}) is very small which can be seen clearly in Figure 6.20. Thus, the modified machine has a very low saliency feature and, consequently, the position estimator based on saliency tracking fails to work even if the harmonic contents of the incremental inductances are lower.

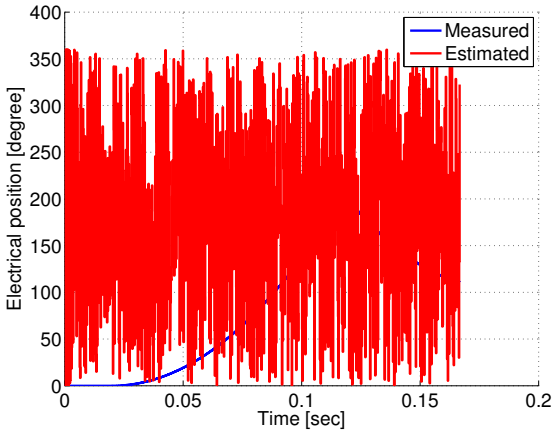

(a)

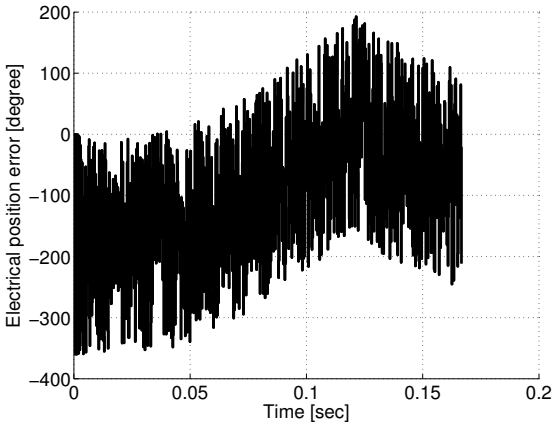

(b)

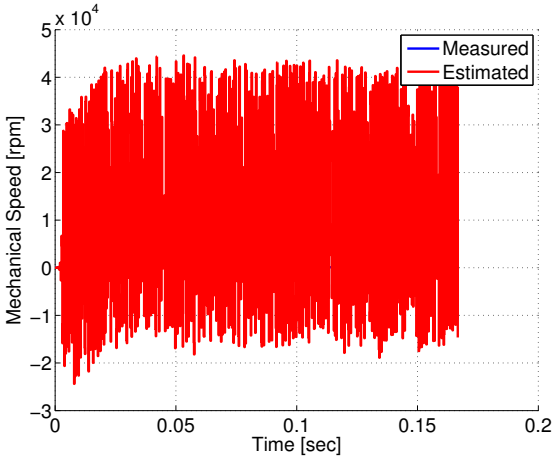

(c)

Figure 6.23:
The simulation results obtained by using the model of Bosch's position estimator and the motor studied in section 6.4: a) Measured and estimated electrical angle b) Position error c) Measured and estimated mechanical speed.

6.4.3 Rated torque and cost

Now, the rated torque of the modified machine should be simulated. Similar to section 3.2.4 in chapter 3, a 3-phase sinusoidal current source which has the phase rated current value and in phase with the 3-phase induced e.m.f is used and the machine is rotated at 2000 *rpm*. As seen from Figure 6.24, the average value of the simulated produced torque is about 1.1004 *pu* where the base is selected as the average value of the simulated rated torque of the original machine that is seen in Figure 3.16.

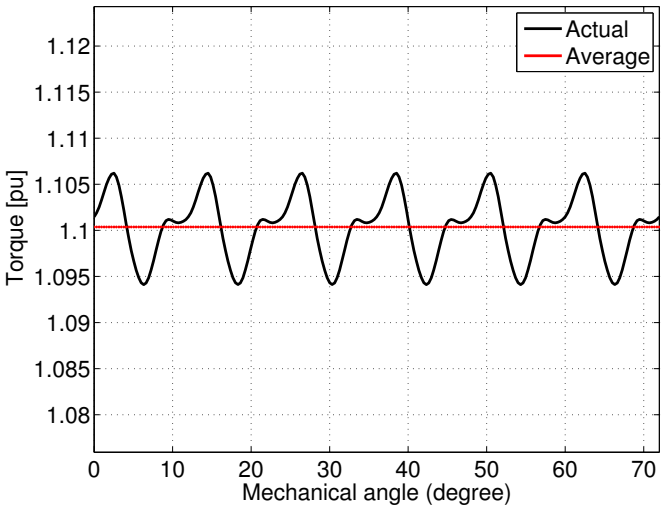

Figure 6.24:
Simulated rated torque which is obtained at the rated speed (2000 *rpm*) of the modified motor in section 6.4 (one complete electrical revolution equivalent to a mechanical angle rotation of about 72 °).

The calculation of the materials costs of the simulated machine is carried out in the same way as in chapter 3. The information about the densities of the materials as well as their prices are obtained from Tables 3.6 and 3.7 respectively. The final costs calculation of the simulated motor studied in section 6.4 can be shown in Table 6.4. Please, note that the volume of the stator winding is kept the same.

Table 6.4: The final costs calculation of the simulated motor studied in section 6.4.

Part	Volume (mm^3)	Cost (€)
Shaft	1009.84	0.00246
Rotor Core	5665.49	0.12373
Stator Core	16386.04	0.35787
Magnets	2688.00	4.37606
Stator Winding	4588.76	0.32782
Total Cost (€)		5.18795

From Figures 3.16 and 6.24, it can be noticed that the simulated rated torque has increased by nearly 10 %. Finally, the total costs of the materials of the machine simulated in chapter 3 have increased by nearly 1.57 % which can be seen by looking at Tables 3.8 and 6.4. The main increase is in the stator core because some parts of the steel material are added to increase the width of the stator teeth. This means that the stator core has an increased weight.

6.4.4 Summary

In conclusion, it is found that increasing the width of the stator teeth makes the machine lose its saleincy and, consequently, a worse sensorless performance is obtained where the position estimator (which is based on saliency tracking) fails to work. This contradicts with the selected KPI concept. The level of harmonic disturbance in the incremental inductances (L_{dd}, L_{qq}, L_{dq}, and L_{qd}) is mostly lower than that of the original machine, and consequently, a better performance of the position estimator is expected which is not the case. This can be explained by the fact that the selected position estimator is based on saliency tracking as discussed in chapter 5 and if the machine loses its saliency, the estimator loses its key strength as there is nothing to track which means that there is no process to measure its quality using the KPI.

6.5 Bigger stator yoke width

In this case, the width of the stator yoke is increased internally while the outer radius of the stator is kept constant. The proposed modification can be shown in Figure 6.25. The same way of modeling in JMAG-Designer in chapter 3 is performed in this case and the bigger stator yoke is constructed.

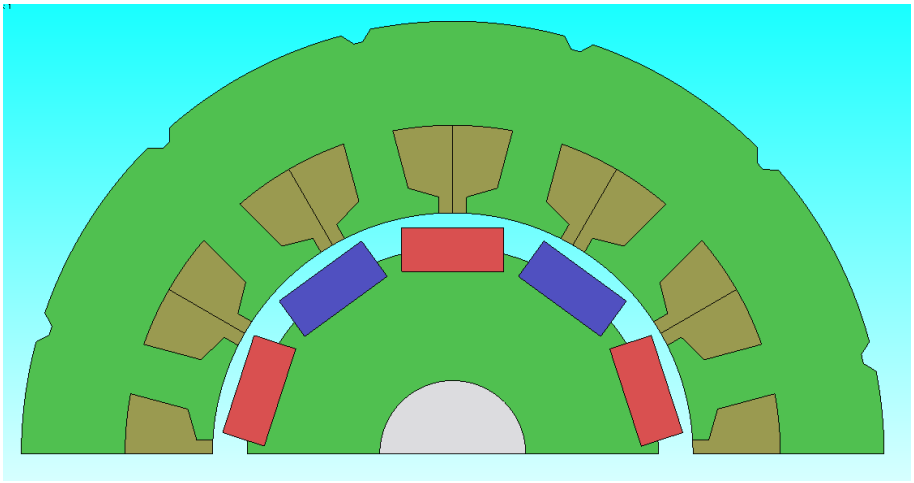

Figure 6.25:
The final 2D half model created by the "geometry editor" in JMAG-Designer including the shaft, rotor core, permanent magnets, stator core, and stator winding for section 6.5.

6.5.1 Incremental inductance

After the model creation in JMAG-Designer, the "Current signal input" block is generated using the JMAG-RT tool and it is used in the same way as discussed in section 4.2 in chapter 4 with Simulink to calculate the incremental inductances (L_{dd}, L_{qq}, L_{dq}, and L_{qd}) as well as their harmonic content. Similar to section 4.2, three loading conditions are studied: the full load, 30 % of the full load, and the no load.

The resulting incremental inductances (L_{dd}, L_{qq}, L_{dq}, and L_{qd}) as well as their harmonic content are calculated with the method described in Section 4.2 and are shown in Figures 6.26 and 6.27 respectively. The resulting values of the incremental inductances (L_{dd}, L_{dq}, L_{qq}, and L_{qd}) plotted against the electrical position of the rotor at no load, 30 % of the full load, and full load are shown in Figures 6.26a, 6.26b, and 6.26c respectively. While, the resulting harmonic content of the incremental inductances (L_{dd}, L_{dq}, L_{qq}, and L_{qd}) at three loads (0 %, 30 %, and 100 %) is shown in Figures 6.27a, 6.27b, 6.27c, and 6.27d respectively. It is worth mentioning that

Figure 6.27 shows the magnitude of the harmonic components of the resulting incremental inductances. These magnitudes are calculated as a per unit representation respect to the offset value (the average inductance) of each related inductance at full load. Also, they are plotted against multiples of the frequency of the electrical period of the motor. Finally, Figure 6.27 is modified such that the DC component is not shown, to make the harmonic content appear in a more clear way as can be seen in Figure 6.28.

From Figure 4.10 and Figure 6.26, it can be seen that the difference between the inductances L_{qq} and L_{dd} is more or less equal to the original machine for the loads 0 %, 30 %, and 100 %.

It is clear from comparing Figure 4.12 of the original machine with Figure 6.28 that the harmonic content of the machine in section 6.5 is mostly lower. For L_{dd}, the sixth harmonic component has decreased by 7 %, 26.3 %, and 26 % for the loads 0 %, 30 %, and 100 % respectively. For L_{dq}, the sixth harmonic component has increased by 41 %, 33 %, and 47 % for the loads 0 %, 30 %, and 100 % respectively. For L_{qq}, the sixth harmonic component has decreased by 21 %, 26 %, and 35 % for the loads 0 %, 30 %, and 100 % respectively. For L_{qd}, the sixth harmonic component has decreased by 8 %, 16.6 %, and 4 % for the loads 0 %, 30 %, and 100 % respectively.

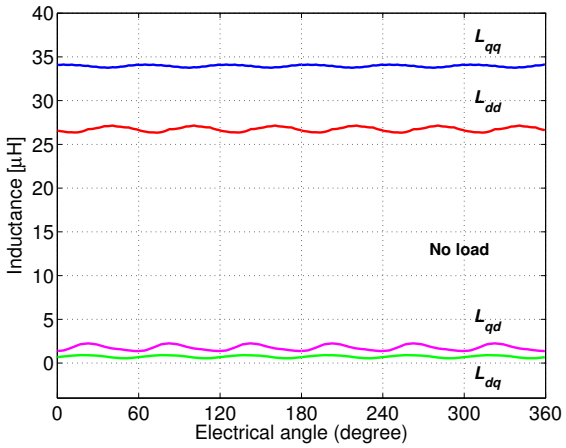

(a)

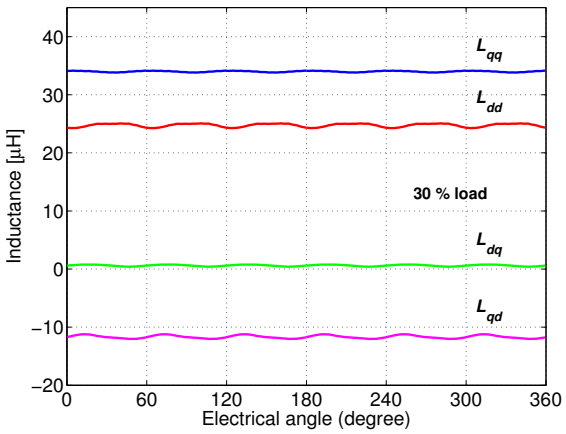

(b)

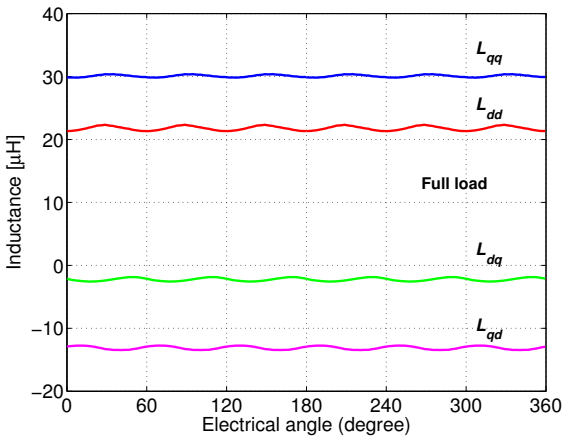

(c)

Figure 6.26:
The resulting values of the incremental inductances plotted against the electrical position of the rotor of the modified motor studied in section 6.5: a) No Load b) 30 % of the full load c) Full load.

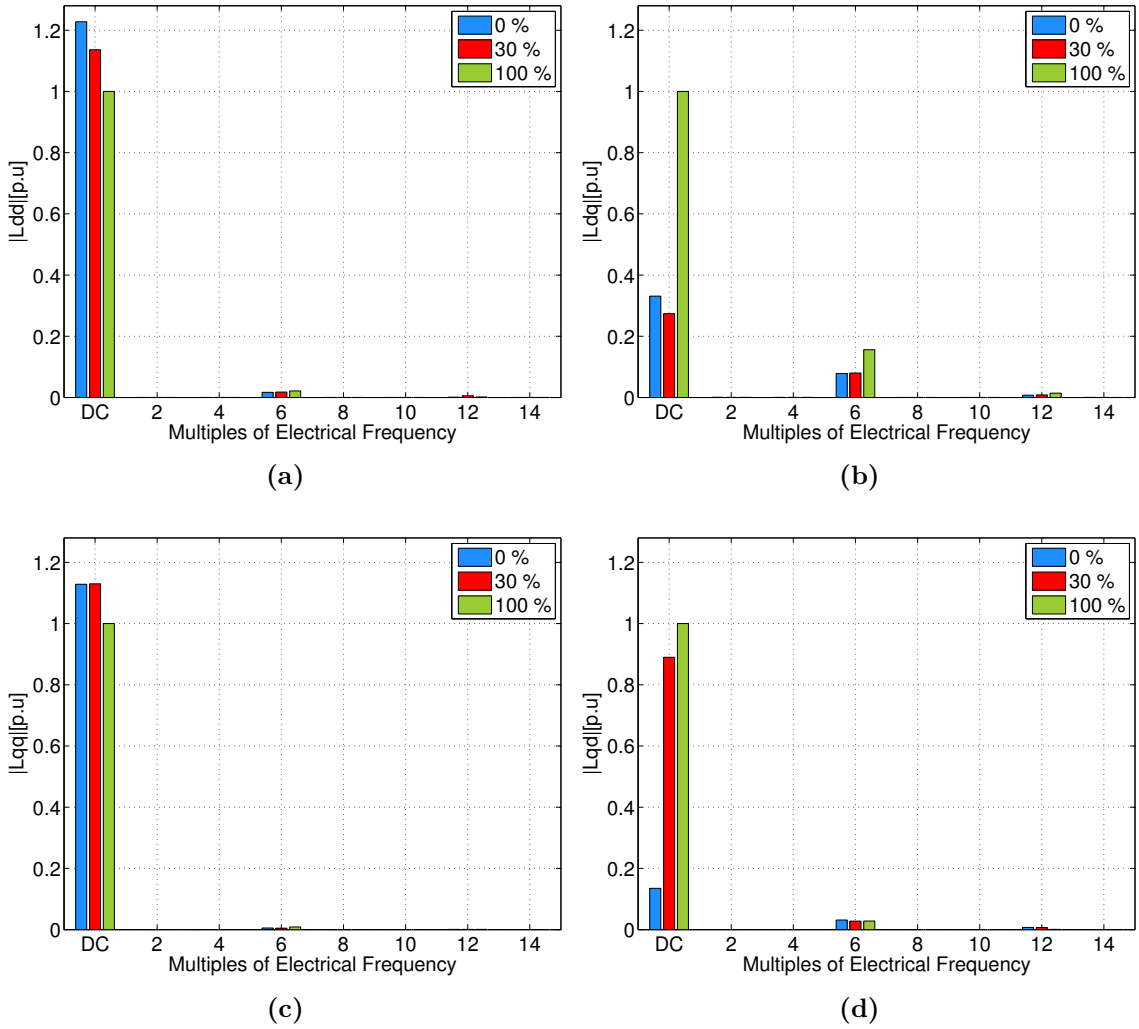

Figure 6.27:
The resulting harmonic content of the incremental inductances for the modified motor studied in section 6.5 at three loads (0 %, 30 %, and 100 %): a)L_{dd} b)L_{dq} c)L_{qq} d)L_{qd}.

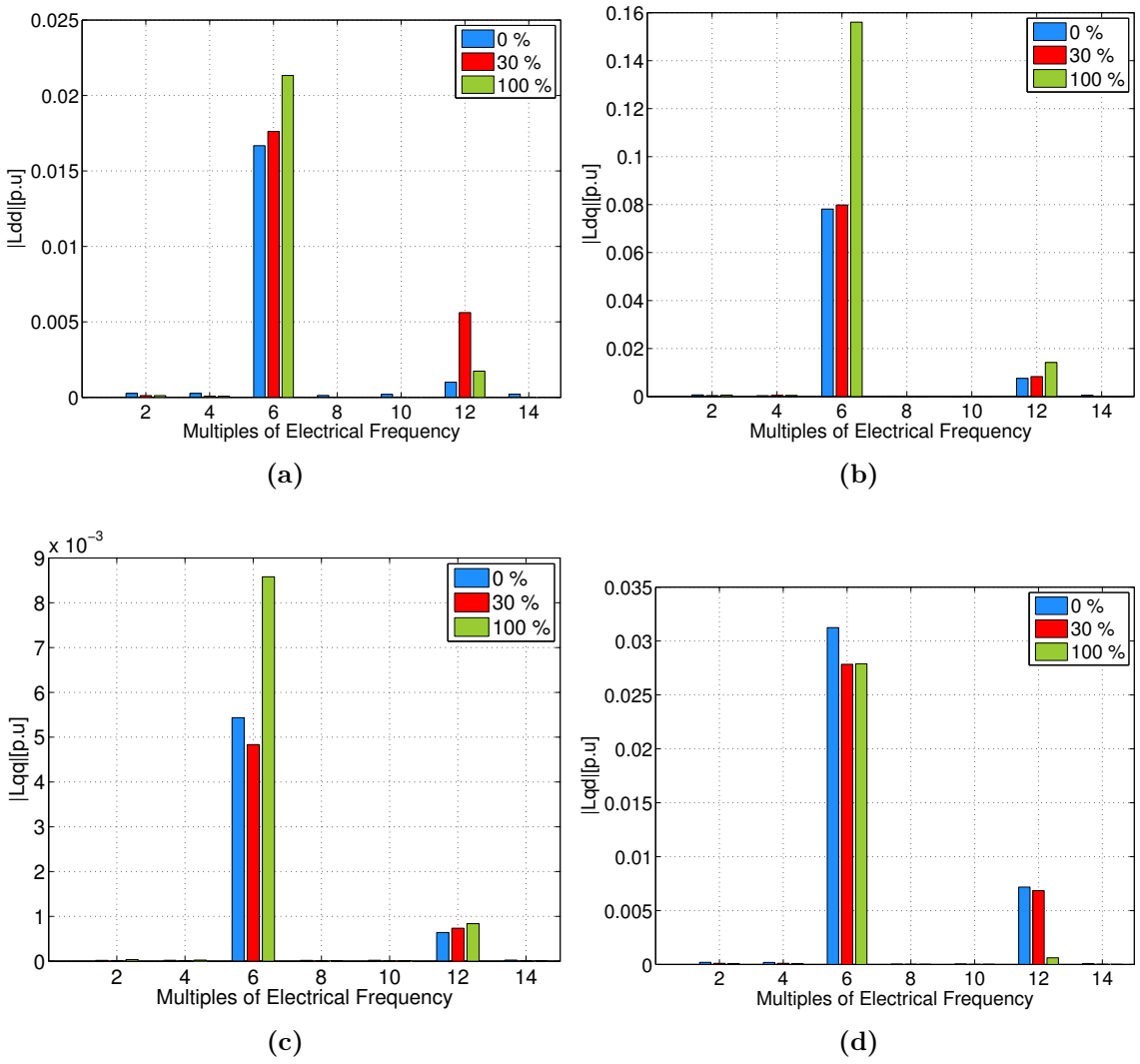

Figure 6.28:
The resulting harmonic content of the incremental inductances for the modified motor studied in section 6.5 at three loads (0 %, 30 %, and 100 %): a)L_{dd} b)L_{dq} c)L_{qq} d)L_{qd} where the DC component is not shown.

6.5.2 Sensorless performance evaluation

Similar to sections 5.4 and 5.5, the sensorless performance of the studied motor is evaluated with Bosch's simulated model of the position estimator and the JMAG model of the motor. The values used in Bosch's simulated model of the position estimator can be shown in Table 5.1 except for the direct and quadrature-axis inductances. The direct and quadrature-axis inductances are obtained as the average of the direct and quadrature axis self-inductances (L_{dd}, and L_{qq}) respectively at no load which can be seen in Figure 6.26a. The obtained results from the simulation are

shown in Figure 6.29. Figure 6.29a shows the measured and the estimated electrical position. The position error shown in Figure 6.29b is obtained by subtracting the estimated electrical position from the measured one. While, Figure 6.29c shows the measured and the estimated mechanical speed.

For the sensorless performance using the model of Bosch's position estimator, comparison can be made between Figures 5.6 for the original machine and Figure 6.29. The electrical position estimation error of the machine studied in section 6.5 (kept between 1 and -18.75 degrees) which can be seen in Figure 6.29b is lower than that of the original machine (kept between 2.5 and -18.75 degrees) which can be seen in Figure 5.6d. These results agree with what is discussed in chapter 4 which implies that the lower harmonic content of the incremental inductances is an indication of a better sensorless performance using saliency tracking. However, it can be noticed in Figure 6.29b that the position estimation error has increased in the negative direction (in the middle) when compared with the position error of the original machine in Figure 5.6d. This may be due to the fact that the harmonic content of the incremental inductances of the machine in section 6.5 is mostly lower than that of the original machine and not all of it. From Figures 6.28b and 4.12b, it can be seen that the harmonic content of the direct axis cross-coupling inductance (L_{dq}) of the machine in section 6.5 is higher than that of the original machine.

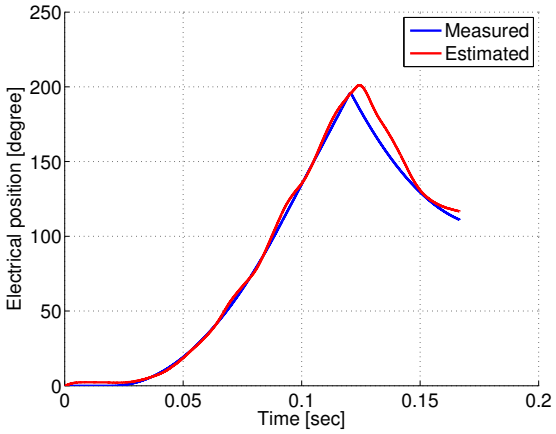

(a)

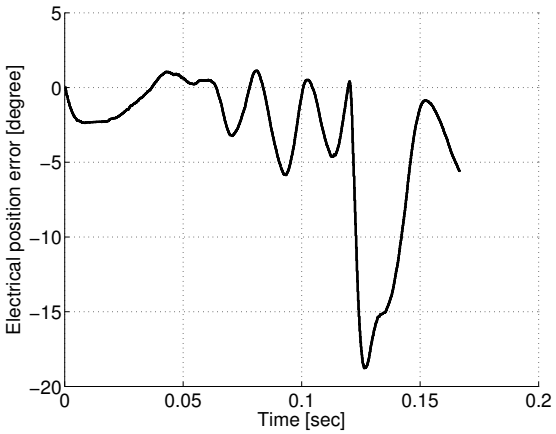

(b)

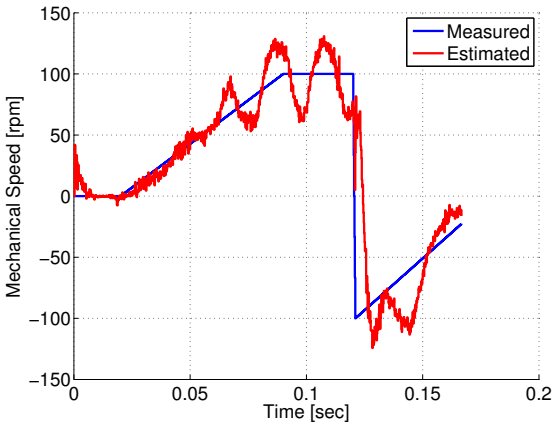

(c)

Figure 6.29:
The simulation results obtained by using the model of Bosch's position estimator and the motor studied in section 6.5: a) Measured and estimated electrical angle b) Position error c) Measured and estimated mechanical speed.

6.5.3 Rated torque and cost

Now, the rated torque of the modified machine should be simulated. Similar to section 3.2.4 in chapter 3, a 3-phase sinusoidal current source which has the phase rated current value and in phase with the 3-phase induced e.m.f is used and the machine is rotated at 2000 *rpm*. As seen from Figure 6.30, the average value of the simulated produced torque is about 1.0464 *pu* where the base is selected as the average value of the simulated rated torque of the original machine that is seen in Figure 3.16.

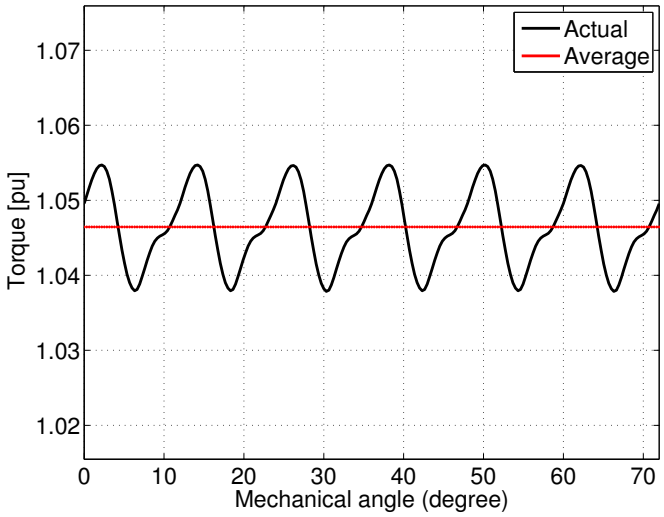

Figure 6.30:
Simulated rated torque which is obtained at the rated speed (2000 *rpm*) of the modified motor in section 6.5 (one complete electrical revolution equivalent to a mechanical angle rotation of about 72 °).

The calculation of the materials costs of the simulated machine is carried out in the same way as in chapter 3. The information about the densities of the materials as well as their prices are obtained from Tables 3.6 and 3.7 respectively. The final costs calculation of the simulated motor studied in section 6.5 can be shown in Table 6.5. Please, note that the volume of the stator winding is kept the same.

Table 6.5: The final costs calculation of the simulated motor studied in section 6.5.

Part	Volume (mm^3)	Cost (€)
Shaft	1009.84	0.00246
Rotor Core	5665.49	0.12373
Stator Core	18847.31	0.41163
Magnets	2688.00	4.37606
Stator Winding	4588.76	0.32782
Total Cost (€)		5.24171

From Figures 3.16 and 6.30, it can be noticed that the simulated rated torque has increased by nearly 4.64 %. Finally, the total costs of the materials of the machine simulated in chapter 3 have increased by nearly 2.62 % which can be seen by looking at Tables 3.8 and 6.5. The main increase is in the stator core because some parts of the steel material are added to increase the width of the stator yoke. This means that the stator core has an increased weight.

6.5.4 Summary

In conclusion, the results verifies that the "the level of harmonic disturbance in the incremental inductances (L_{dd}, L_{qq}, L_{dq}, and L_{qd}) can be used as a key performance indicator to give a preliminary evaluation of the capability of a certain PM synchronous machine to perform sensorless vector control in a good quality using saliency tracking". Additionally, it is found increasing the width of the stator yoke makes the harmonic contents of the incremental inductances mostly lower and, consequently, a better sensorless performance is obtained. However in some time instants, the position error becomes larger than that of the original machine. Finally, this modification results in an increase in the rated toque as well as the materials costs.

6.6 Verification summary

The comparison between each motor modification in chapter 6 and the original motor can be summarized in the Table 6.6. The motors are compared according to: the harmonic contents of the incremental inductances, sensorless performance, rated torque, and cost.

Adding air holes in the rotor core has no effect on the harmonic content of the incremental inductances or the sensorless performance. The electrical position estimation error is still kept between 2.5 and −18.75 degrees. However, this modification can offer the same rated torque with a decrease (0.78 %) in materials costs which is beneficial.

Adding more steel between magnets has a good effect. It makes the harmonic content (KPI) of the inductances mostly lower. For L_{dd}, the sixth harmonic component has decreased by 57 %, 63 %, and 80 % for the loads 0 %, 30 %, and 100 % respectively. For L_{dq}, the sixth harmonic component has decreased by 50 %, 62 %, and 42 % for the loads 0 %, 30 %, and 100 % respectively. For L_{qq}, the sixth harmonic component is approximately the same for the loads 0 % and 30 %, while, it has increased by 93 % for the load 100 %. For L_{qd}, the sixth harmonic component has decreased by 18 %, 58 %, and 17 % for the loads 0 %, 30 %, and 100 % respectively. Also, a better sensorless performance is obtained where the electrical position estimation error is kept between 0.5 and −18.75 degrees. However, there is a decrease (15.6 %) in the rated toque and an increase (0.22 %) in the materials costs.

Closing the openings of the stator slots has a bad effect. It makes the harmonic content (KPI) of the inductances mostly higher in a big way. For L_{dd}, the sixth harmonic component has increased by 242 %, 657 %, and 331 % for the loads 0 %, 30 %, and 100 % respectively. For L_{dq}, the sixth harmonic component has increased by 1536 %, 858 %, and 138 % for the loads 0 %, 30 %, and 100 % respectively. For L_{qq}, the sixth harmonic component has increased by 3292 %, and 669 % for the loads 0 %, and 30 % respectively, while, it has decreased by 8 % for the load 100 %. For L_{qd}, the sixth harmonic component has increased by 455 %, 733 %, and 456 % for the loads 0 %, 30 %, and 100 % respectively. Also, a worse sensorless performance is obtained where the position estimator fails to work. Additionally, there is a decrease (37.7 %) in the rated toque and an increase (0.13 %) in the materials costs.

Increasing the width of the stator teeth has a bad effect regardless of the KPI. It makes the harmonic content (KPI) of the inductances mostly lower. For L_{dd}, the sixth harmonic component has decreased by 75 %, 94 %, and 70 % for the loads 0 %,

30 %, and 100 % respectively. For L_{dq}, the sixth harmonic component has decreased by 27 % and 33 % for the loads 0 % and 30 % respectively, while, it has increased by 376 % for the load 100 %. For L_{qq}, the sixth harmonic component has decreased by 94.6 %, 94.2 %, and 76 % for the loads 0 %, 30 %, and 100 % respectively. For L_{qd}, the sixth harmonic component has decreased by 85 %, 96 %, and 40 % for the loads 0 %, 30 %, and 100 % respectively. In spite of making the harmonic content (KPI) mostly lower, a worse sensorless performance is obtained where the position estimator fails to work. This is due to the decrease in the difference between the direct and quadrature axis self-inductances (L_{dd}, and L_{qq}) (loss of saliency). The difference between the inductances L_{qq} and L_{dd} has decreased by 80 %, 55 %, and 50 % for the loads 0 %, 30 %, and 100 % respectively. Additionally, there is an increase (10 %) in the rated toque and an increase (1.57 %) in the materials costs.

Increasing the width of the stator yoke has a good effect. It makes the harmonic content (KPI) of the inductances mostly lower. For L_{dd}, the sixth harmonic component has decreased by 7 %, 26.3 %, and 26 % for the loads 0 %, 30 %, and 100 % respectively. For L_{dq}, the sixth harmonic component has increased by 41 %, 33 %, and 47 % for the loads 0 %, 30 %, and 100 % respectively. For L_{qq}, the sixth harmonic component has decreased by 21 %, 26 %, and 35 % for the loads 0 %, 30 %, and 100 % respectively. For L_{qd}, the sixth harmonic component has decreased by 8 %, 16.6 %, and 4 % for the loads 0 %, 30 %, and 100 % respectively. Also, a better sensorless performance is mostly obtained where the electrical position estimation error is kept between 1 and -18.75 degrees. Additionally, there is an increase (4.64 %) in the rated toque and an increase (2.62 %) in the materials costs.

Table 6.6: Final comparison of the motor modifications in chapter 6 with the original motor.

Modification	Harmonic content	Sensorless performance	Rated torque	Cost
Air holes in the rotor core	Similar	Similar	Equal	Lower
More steel between magnets	Mostly lower	Better	Lower	Higher
Totally-closed slot openings	Mostly higher (big way)	Fails	Lower	Higher
Bigger stator teeth width	Mostly lower	Fails (loss of saliency)	Higher	Higher
Bigger stator yoke width	Mostly lower	Mostly better	Higher	Higher

7

Conclusion and future work

7.1 Conclusion

In this study, the relation between the machine design, the harmonic content of the incremental inductances (L_{dd}, L_{qq}, L_{dq}, and L_{qd}), and the sensorless performance using saliency tracking has been studied, and verified. Bosch's motor of the engine compartment actuator (ECA - E) has been simulated and compared with the real-life machine performance to make sure that the model is a good representation of the real-life machine (the simulated induced e.m.f. matches the one measured from the real-life machine performance as they are both sinusoidal, they have the same maximum value (1 pu), their periods are equal (360 °) and the simulated cogging torque has the same number of cogging cycles per one mechanical revolution (N_{co}= 60) as well as the period (6 °)). Also, the methodology for the measurement of the incremental inductances has been implemented and simulated using SIMULINK.

Additionally, the coupling between the FEA machine model and the Bosch position estimator has proven to be possible and successful. This allows the inclusion of the load and saturation effects, of the anisotropy determined by the rotor position and current phase angles, and of the cross-coupling between the quadrature and direct axes in the controller, as well as in the position and speed observer dimensioning process as the used model of the machine is based on FEM calculations. Finally, it has been verified that the selected key performance indicator (the harmonic content of the incremental inductances) is reliable and it can evaluate the quality of the potential sensorless vector control capabilities of a certain permanent magnet synchronous machine in the early design stages in comparison with a base model.

It has been proven that the harmonic content of the incremental inductances of the permanent magnet synchronous machine are connected to the motor design. This includes the dimensions of the different parts of the studied motor. Most of the changes in the machine dimensions will have an impact on the harmonic content

and, consequently, the sensorless performance using saliency tracking will differ.

When the air holes were added in the rotor core of the machine in the direct axis direction, there was no effect on the harmonic content of the incremental inductances or the sensorless performance (the electrical position estimation error is still kept between 2.5 and −18.75 degrees which is similar to the original machine). The effect may be noticed if the air holes are placed closer to the magnets but this was not simulated due to Bosch's manufacturing regulations. It has been found that this modification can offer the same sensorless performance as well as the rated torque with a decrease (0.78 %) in materials costs which is beneficial.

It has been proven that adding more steel material in the rotor core in the quadrature axis direction has a good effect. This modification results in lower harmonic content of the incremental inductances and a better sensorless performance using saliency tracking. For L_{dd}, the sixth harmonic component has decreased by 57 %, 63 %, and 80 % for the loads 0 %, 30 %, and 100 % respectively. For L_{dq}, the sixth harmonic component has decreased by 50 %, 62 %, and 42 % for the loads 0 %, 30 %, and 100 % respectively. For L_{qq}, the sixth harmonic component is approximately the same for the loads 0 % and 30 %, while, it has increased by 93 % for the load 100 %. For L_{qd}, the sixth harmonic component has decreased by 18 %, 58 %, and 17 % for the loads 0 %, 30 %, and 100 % respectively. Additionally, the electrical position estimation error is kept between 0.5 and −18.75 degrees which is better. The disadvantage of this modification is that there is a decrease (15.6 %) in the rated toque and an increase (0.22 %) in the materials costs.

Closing the openings of the stator slots has a very bad impact on the machine performance. There is a big increase in the harmonic content of the incremental inductances and the position estimator fails to work as intended. For L_{dd}, the sixth harmonic component has increased by 242 %, 657 %, and 331 % for the loads 0 %, 30 %, and 100 % respectively. For L_{dq}, the sixth harmonic component has increased by 1536 %, 858 %, and 138 % for the loads 0 %, 30 %, and 100 % respectively. For L_{qq}, the sixth harmonic component has increased by 3292 %, and 669 % for the loads 0 %, and 30 % respectively, while, it has decreased by 8 % for the load 100 %. For L_{qd}, the sixth harmonic component has increased by 455 %, 733 %, and 456 % for the loads 0 %, 30 %, and 100 % respectively. This modification results in a reduction (37.7 %) in the machine's rated torque. In addition to that, there is an increase (0.13 %) in the total costs of the materials of the machine.

The position estimator also fails to work when the width of the stator teeth of the machine is increased. This modification results in lower harmonic content of the incremental inductances. However, the machine lose its saliency as the difference

between the direct and quadrature axis self-inductances (L_{dd}, and L_{qq}) becomes very small (the difference between the inductances L_{qq} and L_{dd} has decreased by 80 %, 55 %, and 50 % for the loads 0 %, 30 %, and 100 % respectively). This explains why the position estimator fails. For L_{dd}, the sixth harmonic component has decreased by 75 %, 94 %, and 70 % for the loads 0 %, 30 %, and 100 % respectively. For L_{dq}, the sixth harmonic component has decreased by 27 % and 33 % for the loads 0 % and 30 % respectively, while, it has increased by 376 % for the load 100 %. For L_{qq}, the sixth harmonic component has decreased by 94.6 %, 94.2 %, and 76 % for the loads 0 %, 30 %, and 100 % respectively. For L_{qd}, the sixth harmonic component has decreased by 85 %, 96 %, and 40 % for the loads 0 %, 30 %, and 100 % respectively. The advantage of this modification is that the rated torque is increased (10 %). But, there is an increase (1.57 %) in the materials costs.

Increasing the width of the stator yoke makes the harmonic content of the incremental inductances mostly lower. For L_{dd}, the sixth harmonic component has decreased by 7 %, 26.3 %, and 26 % for the loads 0 %, 30 %, and 100 % respectively. For L_{dq}, the sixth harmonic component has increased by 41 %, 33 %, and 47 % for the loads 0 %, 30 %, and 100 % respectively. For L_{qq}, the sixth harmonic component has decreased by 21 %, 26 %, and 35 % for the loads 0 %, 30 %, and 100 % respectively. For L_{qd}, the sixth harmonic component has decreased by 8 %, 16.6 %, and 4 % for the loads 0 %, 30 %, and 100 % respectively. A better sensorless performance is obtained by this modification where the electrical position estimation error is kept between 1 and -18.75 degrees. However in some time instants (negative part in the middle), the position error becomes larger than that of the original machine. This may be due to the fact that not all of the harmonic contents of the incremental inductances are reduced as the harmonic contents of the direct axis cross-coupling inductance (L_{dq}) of the machine becomes larger. Additionally, the rated torque of the machine increases (4.64 %) by this modification. But, there is an increase (2.62 %) in the total costs of the materials of the machine.

7.2 Future work

As seen in chapter 6, the reduction of all of the harmonic content of the incremental inductances of the machine can't be done by just one simple geometric modification. Most of the harmonic contents can be reduced but not all of them. Consequently, an optimization study should be performed by varying the machine dimensions to obtain the lowest possible harmonic contents and the best sensorless performance.

Additionally, the implemented methodology for the measurement of the incre-

mental inductances is to be integrated into Bosch's in-house Finite Element Analysis software (EDYSON) in an automated and user-friendly interface instead of using SIMULINK and JMAG-RT. Also, instead of using the JMAG-RT generated block in the system simulation the flux-based machine modeling can be developed and integrated, eliminating the JMAG license bottle-neck when performing an optimization.

Bibliography

[1] ED/MBL - NA Department, *Electrical drives - actuation systems*, Internal presentation, Section: Engine Compartment Actuators, Robert Bosch GmbH, 2015.

[2] O. Choi and A. Fisher, "The Impacts of Socioeconomic Development and Climate Change on Severe Weather Catastrophe Losses: Mid-Atlantic Region (MAR) and the U.S.", English, *Climatic Change*, vol. 58, no. 1-2, pp. 149–170, 2003.

[3] Global Fuel Economy Initiative, *Top Reasons for Supporting Cleaner, More Efficient Vehicles*, Internet, Accessed: 2015-04-15. [Online]. Available: `http://www.unep.org/transport/gfei/autotool/Pdf%27s/Top_Reasons_leaflet_with_bleed.pdf`.

[4] M. Ehsani, F. Wang, and G. Brosch, *Transportation Technologies for Sustainability*, 1st ed. New York: SPRINGER VERLAG GMBH, 2013, p. 1190.

[5] J. Åström, *Permanent magnets and PM Motors*, Lecture notes, Course: Electric Drives I, Chalmers University of Technology, 2013.

[6] Schonhardt, "Musterprüfbericht - ECA-E Smart Actuator B1.1 Muster", Robert Bosch GmbH, Tech. Rep. 2012/050, Jun. 18, 2012.

[7] C. A. Silva, "Sensorless vector control of surface mounted permanent magnet machines without restriction of zero frequency", PhD thesis, The University of Nottingham, May 2003. [Online]. Available: `http://eprints.nottingham.ac.uk/id/eprint/12435`.

[8] S. Sul, *Control of Electric Machine Drive Systems*, ser. IEEE Press Series on Power Engineering. Hoboken, New Jersey: Wiley, 2011, p. 399.

[9] J. Arellano-Padilla, M. Sumner, C. Gerada, and G. Asher, "Prediction of Inductance Characteristics in PMSMs and their impact on Saliency-based Sensorless Control", presented at the Power Electronics and Motion Control Conference, Novi Sad, 2012.

[10] Robert Bosch GmbH, *Automotive industry portal*, Internet, Accessed: 2015-04-16. [Online]. Available: `http://www.bosch.de/en/de/startpage_1/automotive-industr-portal.html`.

[11] JSOL Corporation, *FEA Software for Electromechanical Design*, Internet, Accessed: 2015-04-17. [Online]. Available: `https://www.jmag-international.com/products/jmag-designer/`.

[12] W. Tong, *Mechanical Design of Electric Motors*, 1st ed. Taylor & Francis, 2014, p. 736.

[13] R. Krishnan, *Permanent Magnet Synchronous and Brushless DC Motor Drives*, 1st ed. Blacksburg, Virginia: CRC Press, 2009, p. 611.

[14] A. Hughes and B. Drury, *Electric Motors and Drives: Fundamentals, Types and Applications*, Fourth Edition. Boston: Newnes, 2013, p. 440.

[15] A. N. Ştirban, "Low cogging torque tooth wound PMSM drives with rectangular current control", PhD thesis, University "Politehnica" of Timisoara, Faculty of Electrical and Power Engineering, Oct. 2010.

[16] J. Arellano-Padilla, M. Sumner, C. Gerada, and G. Asher, "Prediction of Inductance Characteristics of PMSMs in Saliency-based Sensorless Control", presented at the Power Electronics and Motion Control Conference, Novi Sad, 2012, LS3a–1.1–1 –LS3a–1.1–5.

[17] S. Lundberg, *PMSM-Drive*, Lecture notes, Course: Electric Drives II, Chalmers University of Technology, 2013.

[18] J. Arellano-Padilla, C. Gerada, G. Asher, and M. Sumner, "Inductance Characteristics of PMSMs and their Impact on Saliency-based Sensorless Control", presented at the Power Electronics and Motion Control Conference, Ohrid, 2010, S1–1 –S1–9.

[19] T. Miller, *Speed's electric machines (software manual)*, Computational Dynamics Ltd. "CD-adapco", 2014.

[20] D. Stellas, "Sensorless scalar and vector control of a subsea PMSM", M.Sc. thesis, Chalmers University of Technology, Gothenburg, Sweden, 2013.

[21] A. Bondeson, T. Rylander, and P. Ingelström, *Computational Electromagnetics*, Second Edition, ser. Texts in Applied Mathematics. Springer, 2013.

[22] Y. Serdyuk, *Finite Element Method*, Lecture notes, Course: Applied Computational Electromagnetics, Chalmers University of Technology, 2014.

[23] T. Miller, *Speed's electric machines (steels database)*, Computational Dynamics Ltd. "CD-adapco", 2014.

[24] ZHENGZHOU JINGYING IRON AND STEEL CO.,LTD., *Steel sheets SS400 A36 A283GrC ST37 S235JR*, Internet, Accessed: 2015-05-27. [Online]. Available: `http://steelplates.en.china.cn/selling-leads/detail,1160798794,steel-sheets-SS400-A36-A283GrC-ST37-S235JR.html`.

[25] A. A. Ganji, P. Gillaume, R. Pintelon, and P. Lataire, "Induction motor dynamic and static inductance identification using a broadband excitation technique", *IEEE Transactions on Energy Conversion*, vol. 13, no. 1, pp. 15–20, 1998.

[26] S. Kim, J.-I. Ha, and S.-K. Sul, "PWM Switching Frequency Signal Injection Sensorless Method in IPMSM", *IEEE Transactions on Industry Applications*, vol. 48, no. 5, pp. 1576 –1587, 2012.

[27] I. Serban, "Sensorless rotor position estimation of high-dynamic EC-Drives", Robert Bosch GmbH, Tech. Rep. 1588, Mar. 28, 2012.

A

Appendix

A.1 Transformations

Transformations between three-phase and two-phase system and amplitude invariant transformation

$$\begin{bmatrix} S_\alpha \\ S_\beta \end{bmatrix} = \frac{2}{3} \begin{bmatrix} 1 & -\frac{1}{2} & -\frac{1}{2} \\ 0 & \frac{\sqrt{3}}{2} & -\frac{\sqrt{3}}{2} \end{bmatrix} \begin{bmatrix} S_a \\ S_b \\ S_c \end{bmatrix}, \quad \begin{bmatrix} S_a \\ S_b \\ S_c \end{bmatrix} = \begin{bmatrix} 1 & 0 \\ -\frac{1}{2} & \frac{\sqrt{3}}{2} \\ -\frac{1}{2} & -\frac{\sqrt{3}}{2} \end{bmatrix} \begin{bmatrix} S_\alpha \\ S_\beta \end{bmatrix} \tag{A.1}$$

Transformation between rotating and stationary coordinate system

$$\underline{u}^s = \underline{u} e^{j\theta}, \ \underline{u} = \underline{u}^s e^{-j\theta}, \ e^{j\theta} = \cos\theta + j \sin\theta \tag{A.2}$$

$$\begin{bmatrix} u_\alpha \\ u_\beta \end{bmatrix} = \begin{bmatrix} \cos\theta & -\sin\theta \\ \sin\theta & \cos\theta \end{bmatrix} \begin{bmatrix} u_d \\ u_q \end{bmatrix}, \quad \begin{bmatrix} u_d \\ u_q \end{bmatrix} = \begin{bmatrix} \cos\theta & \sin\theta \\ -\sin\theta & \cos\theta \end{bmatrix} \begin{bmatrix} u_\alpha \\ u_\beta \end{bmatrix} \tag{A.3}$$

A.2 Fourier Series

Let f be a piecewise continuous function on $[-\pi, \pi]$. Then the **Fourier series** of f is the series

$$a_0 + \sum_{n=1}^{\infty} (a_n \cos nx + b_n \sin nx) \tag{A.4}$$

where the coefficients a_0, a_n, and b_n in this series are defined by

$$a_0 = \frac{1}{2\pi} \int_{-\pi}^{\pi} f(x)\,\mathrm{d}x, \ a_n = \frac{1}{\pi} \int_{-\pi}^{\pi} f(x) \cos nx\,\mathrm{d}x, \ b_n = \frac{1}{\pi} \int_{-\pi}^{\pi} f(x) \sin nx\,\mathrm{d}x \tag{A.5}$$

and are called the **Fourier coefficients** of f.

A.3 Matlab Code for the Proposed Key Performance Indicator

```
clc         % clear command window
clear all   % clear workspace memory
close all   % closing all plot windows

%*********************************************************************
% Parameter definition ( ECA-E machine)                              *
%*********************************************************************
P  =10;              % Total number of poles
Omega  =2000;             % Rated mechanical speed in RPM
delta=0.5;                 % injected current disturbance

%*********************************************************************
% Current in dq ( To get the three phase current be used as a source in
% JMAG) *
%*********************************************************************

%No Disturbance - Case 1
D0=0;               % d-current in A
Q0=50;               % q-current in A

%Disturbance in d - Case 2
Dd=0+delta;               % d-current in A
Qd=50;               % q-current in A

%Disturbance in q - Case 3
Dq=0;               % d-current in A
Qq=50+delta;               % q-current in A


% Call Simulink
%*********************************************************************
Tstart=0;
step=0.00001;
Fs=1/step;
Tstop=0.006*1;            % one electrical cycle
sim('Parameters_calculation_calc',[Tstart:step:Tstop])

%*********************************************************************
% Removal of the first point which causes wrong calculations
% based on the periodicity
%*********************************************************************

PSI_D0(1) = PSI_D0(end);
PSI_D0 = PSI_D0(1:end-1);
PSI_Dd(1) = PSI_Dd(end);
PSI_Dd = PSI_Dd(1:end-1);
PSI_Dq(1) = PSI_Dq(end);
PSI_Dq = PSI_Dq(1:end-1);
```

```
PSI_Q0(1) = PSI_Q0(end);
PSI_Q0 = PSI_Q0(1:end-1);
PSI_Qd(1) = PSI_Qd(end);
PSI_Qd = PSI_Qd(1:end-1);
PSI_Qq(1) = PSI_Qq(end);
PSI_Qq = PSI_Qq(1:end-1);

I_A0(1)= I_A0(end);
I_A0 = I_A0(1:end-1);
I_B0(1)= I_B0(end);
I_B0 = I_B0(1:end-1);
I_C0(1)= I_C0(end);
I_C0 = I_C0(1:end-1);
I_D0(1)= I_D0(end);
I_D0 = I_D0(1:end-1);
I_Q0(1)= I_Q0(end);
I_Q0 = I_Q0(1:end-1);

I_Ad(1)= I_Ad(end);
I_Ad = I_Ad(1:end-1);
I_Bd(1)= I_Bd(end);
I_Bd = I_Bd(1:end-1);
I_Cd(1)= I_Cd(end);
I_Cd = I_Cd(1:end-1);
I_Dd(1)= I_Dd(end);
I_Dd = I_Dd(1:end-1);
I_Qd(1)= I_Qd(end);
I_Qd = I_Qd(1:end-1);

I_Aq(1)= I_Aq(end);
I_Aq = I_Aq(1:end-1);
I_Bq(1)= I_Bq(end);
I_Bq = I_Bq(1:end-1);
I_Cq(1)= I_Cq(end);
I_Cq = I_Cq(1:end-1);
I_Dq(1)= I_Dq(end);
I_Dq = I_Dq(1:end-1);
I_Qq(1)= I_Qq(end);
I_Qq = I_Qq(1:end-1);

t = t(1:end-1);
theta_el = 2*pi*Omega/60*P/2*t;    % Rated electrical angle in rad

%**********************************************************************
% Calculation of incremental inductance according to Asher            *
%**********************************************************************

Ldd=(PSI_Dd-PSI_D0)./delta;
Ldq=(PSI_Dq-PSI_D0)./delta;
Lqq=(PSI_Qq-PSI_Q0)./delta;
Lqd=(PSI_Qd-PSI_Q0)./delta;

%**********************************************************************
% Plotting                                    *
%**********************************************************************
set(0,'DefaultAxesFontSize',14)
```

```
%No Disturbance - Case 1
figure('Name','No Disturbance - Case 1','NumberTitle','off')
subplot(2,2,1)
plot(t,I_A0,'b',t,I_B0,'r',t,I_C0,'g')
grid on
xlabel('Time (s)')
ylabel('Stator Current [A]')
title('blue A-phase, red B-phase, green C-phase')

subplot(2,2,2)
plot(t,I_D0,'b',t,I_Q0,'r')
%axis([0 inf -3 11])
grid on
xlabel('Time (s)')
ylabel('Stator Current Component [A]')
title('blue d-component, red q-component')

subplot(2,2,3)
plot(t,PSI_D0,'b',t,PSI_Q0,'r')
%axis([0 inf -3 11])
grid on
xlabel('Time (s)')
ylabel('Flux Component [Wb]')
title('blue d-component, red q-component')

%Disturbance in d - Case 2
figure('Name','Disturbance in d - Case 2','NumberTitle','off')
subplot(2,2,1)
plot(t,I_Ad,'b',t,I_Bd,'r',t,I_Cd,'g')
grid on
xlabel('Time (s)')
ylabel('Stator Current [A]')
title('blue A-phase, red B-phase, green C-phase')

subplot(2,2,2)
plot(t,I_Dd,'b',t,I_Qd,'r')
%axis([0 inf -3 11])
grid on
xlabel('Time (s)')
ylabel('Stator Current Component [A]')
title('blue d-component, red q-component')

subplot(2,2,3)
plot(t,PSI_Dd,'b',t,PSI_Qd,'r')
grid on
xlabel('Time (s)')
ylabel('Flux Component [Wb]')
title('blue d-component, red q-component')

%Disturbance in q - Case 3
figure('Name','Disturbance in q - Case 3','NumberTitle','off')
subplot(2,2,1)
plot(t,I_Aq,'b',t,I_Bq,'r',t,I_Cq,'g')
grid on
xlabel('Time (s)')
ylabel('Stator Current [A]')
```

```
title('blue A-phase, red B-phase, green C-phase')

subplot(2,2,2)
plot(t,I_Dq,'b',t,I_Qq,'r')
%axis([0 inf -3 11])
grid on
xlabel('Time (s)')
ylabel('Stator Current Component [A]')
title('blue d-component, red q-component')

subplot(2,2,3)
plot(t,PSI_Dq,'b',t,PSI_Qq,'r')
grid on
xlabel('Time (s)')
ylabel('Flux Component [Wb]')
title('blue d-component, red q-component')

%Incremental inductances


figure('Name','1a- Direct-axis self-inductance(Ldd)','NumberTitle','off')
plot(Omega*(360/60)*P/2*t,Ldd/(1e-06),'b')
%axis([0 inf 1e-05 4e-05])
grid on
xlabel('Electrical angle (degree)')
ylabel('Ldd [\muH]')

nue_dd = 0:100; % electrical order
n_dd = length(Ldd);
for i = 1:length(nue_dd)
    if i == 1
        k = 1;
    else
        k = 2;
    end
    an_dd(i) = sum(k/n_dd*Ldd.*cos(nue_dd(i)*theta_el));
    bn_dd(i) = sum(k/n_dd*Ldd.*sin(nue_dd(i)*theta_el));
end

A_dd = sqrt(an_dd.^2 + bn_dd.^2);

figure('Name','1b- Harmonic content of Ldd ','NumberTitle','off')
bar(nue_dd(1:2:15),A_dd(1:2:15)/A_dd(1)) ;
grid on
set(gca,'Xtick',nue_dd(1:2:15),'XTickLabel',{'DC', '2', '4', '6','8',...
    '10','12','14'})
xlabel('Multiples of Electrical Frequency')
ylabel('|Ldd|[p.u]')

figure('Name','2a- Direct-axis cross-coupling inductance(Ldq)',...
    'NumberTitle','off')
plot(Omega*(360/60)*P/2*t,Ldq/(1e-06),'b')
%axis([0 inf 1e-05 4e-05])
grid on
xlabel('Electrical angle (degree)')
ylabel('Ldq [\muH]')
```

```
nue_dq = 0:100; % electrical order
n_dq = length(Ldq);
for i = 1:length(nue_dq)
    if i == 1
        k = 1;
    else
        k = 2;
    end
    an_dq(i) = sum(k/n_dq*Ldq.*cos(nue_dq(i)*theta_el));
    bn_dq(i) = sum(k/n_dq*Ldq.*sin(nue_dq(i)*theta_el));
end

A_dq = sqrt(an_dq.^2 + bn_dq.^2);

figure('Name','2b- Harmonic content of Ldq ','NumberTitle','off')
bar(nue_dq(1:2:15),A_dq(1:2:15)/A_dq(1)) ;
grid on
set(gca,'Xtick',nue_dq(1:2:15),'XTickLabel',{'DC', '2', '4', '6','8',...
    '10', '12','14'})
xlabel('Multiples of Electrical Frequency')
ylabel('|Ldq|[p.u]')

figure('Name','3a- Quadrature-axis self-inductance(Lqq)',...
    'NumberTitle','off')
plot(Omega*(360/60)*P/2*t,Lqq/(1e-06),'b')
%axis([0 inf 1e-05 4e-05])
grid on
xlabel('Electrical angle (degree)')
ylabel('Lqq [\muH]')

nue_qq = 0:100; % electrical order
n_qq = length(Lqq);
for i = 1:length(nue_qq)
    if i == 1
        k = 1;
    else
        k = 2;
    end
    an_qq(i) = sum(k/n_qq*Lqq.*cos(nue_qq(i)*theta_el));
    bn_qq(i) = sum(k/n_qq*Lqq.*sin(nue_qq(i)*theta_el));
end

A_qq = sqrt(an_qq.^2 + bn_qq.^2);

figure('Name','3b- Harmonic content of Lqq ','NumberTitle','off')
bar(nue_qq(1:2:15),A_qq(1:2:15)/A_qq(1)) ;
grid on
set(gca,'Xtick',nue_qq(1:2:15),'XTickLabel',{'DC', '2', '4', '6',...
    '8', '10', '12','14'})
xlabel('Multiples of Electrical Frequency')
ylabel('|Lqq|[p.u]')

figure('Name','4a- Quadrature-axis cross-coupling inductance(Lqd)'...
    ,'NumberTitle','off')
plot(Omega*(360/60)*P/2*t,Lqd/(1e-06),'b')
```

```
%axis([0 inf 1e-05 4e-05])
grid on
xlabel('Electrical angle (degree)')
ylabel('Lqd [\muH]')

nue_qd = 0:100; % electrical order
n_qd = length(Lqd);
for i = 1:length(nue_qd)
    if i == 1
        k = 1;
    else
        k = 2;
    end
    an_qd(i) = sum(k/n_qd*Lqd.*cos(nue_qd(i)*theta_el));
    bn_qd(i) = sum(k/n_qd*Lqd.*sin(nue_qd(i)*theta_el));
end

A_qd = sqrt(an_qd.^2 + bn_qd.^2);

figure('Name','4b- Harmonic content of Lqd ','NumberTitle','off')
bar(nue_qd(1:2:15),A_qd(1:2:15)/A_qd(1)) ;
grid on
set(gca,'Xtick',nue_qd(1:2:15),'XTickLabel',{'DC', '2', '4', '6',...
    '8', '10', '12','14'})
xlabel('Multiples of Electrical Frequency')
ylabel('|Lqd|[p.u]')


%**************************************************************************
% Testing                                  *
%**************************************************************************

A0=max(I_A0)
Ad=max(I_Ad)
Aq=max(I_Aq)


PSI_A0(1) = PSI_A0(end);
PSI_A0 = PSI_A0(1:end-1);
PSI_Ad(1) = PSI_Ad(end);
PSI_Ad = PSI_Ad(1:end-1);
PSI_Aq(1) = PSI_Aq(end);
PSI_Aq = PSI_Aq(1:end-1);

PSI_B0(1) = PSI_B0(end);
PSI_B0 = PSI_B0(1:end-1);
PSI_Bd(1) = PSI_Bd(end);
PSI_Bd = PSI_Bd(1:end-1);
PSI_Bq(1) = PSI_Bq(end);
PSI_Bq = PSI_Bq(1:end-1);

PSI_C0(1) = PSI_C0(end);
PSI_C0 = PSI_C0(1:end-1);
PSI_Cd(1) = PSI_Cd(end);
PSI_Cd = PSI_Cd(1:end-1);
PSI_Cq(1) = PSI_Cq(end);
```

```
PSI_Cq = PSI_Cq(1:end-1);



figure
plot(t,PSI_A0,'b',t,PSI_Ad,'r',t,PSI_Aq,'g')
grid on
figure
plot(t,PSI_B0,'b',t,PSI_Bd,'r',t,PSI_Bq,'g')
grid on
figure
plot(t,PSI_C0,'b',t,PSI_Cd,'r',t,PSI_Cq,'g')
grid on
```